DETECTION OF DEFECT IN CONCRETE USING ELASTIC WAVE TOMOGRAPHY RECONSTRUCTION TECHNIQUE

LIU KIT FOOK

FACULTY OF ENGINEERING
UNIVERSITY OF MALAYA
KUALA LUMPUR

2017

DETECTION OF DEFECT IN CONCRETE USING ELASTIC WAVE TOMOGRAPHY RECONSTRUCTION TECHNIQUE

LIU KIT FOOK

DISSERTATION SUBMITTED IN FULFILMENT
OF THE REQUIREMENT FOR THE DEGREE OF
MASTER OF ENGINEERING SCIENCE

DEPARTMENT OF CIVIL ENGINEERING
FACULTY OF ENGINEERING
UNIVERSITY OF MALAYA
KUALA LUMPUR

2017

UNIVERSITI MALAYA

ORIGINAL LITERARY WORK DECLARATION

Name of Candidate: LIU KIT FOOK

Registration/Matric No: KGA120016

Name of Degree: MASTER OF ENGINEERING SCIENCE

Title of Project Paper/Research Report/Dissertation/Thesis (“this Work”):

DETECTION OF DEFECT IN CONCRETE USING ELASTIC WAVE TOMOGRAPHY RECONSTRUCTION TECHNIQUE

Field of Study: CIVIL ENGINEERING

I do solemnly and sincerely declare that:

(1) I am the sole author/writer of this Work;
(2) This Work is original;
(3) Any use of any work in which copyright exists was done by way of fair dealing and for permitted purposes and any excerpt or extract from, or reference to or reproduction of any copyright work has been disclosed expressly and sufficiently and the title of the Work and its authorship have been acknowledged in this Work;
(4) I do not have any actual knowledge nor do I ought reasonably to know that the making of this work constitutes an infringement of any copyright work;
(5) I hereby assign all and every rights in the copyright to this Work to the University of Malaya (“UM”), who henceforth shall be owner of the copyright in this Work and that any reproduction or use in any form or by any means whatsoever is prohibited without the written consent of UM having been first had and obtained;
(6) I am fully aware that if in the course of making this Work I have infringed any copyright whether intentionally or otherwise, I may be subject to legal action or any other action as may be determined by UM.

Candidate’s Signature Date

Subscribed and solemnly declared before,

Witness’s Signature Date

Name:
Designation:

Abstract

Non-destructive evaluation (NDE) and structural health monitoring (SHM) methods have become a vital technology in civil engineering industry. Defects found in new or aging structures may cause casualty. Hence, detection and assessment of defects in structures have to be carried out effectively. The tomography technique is one of the NDE methods that evaluate soundness of concrete structures by providing visualization to its interior. In this study, three different types of elastic wave properties have been considered in developing tomography reconstruction methodologies namely travel time (velocity), amplitude and frequency. The developments of algorithms for these methodologies are undertaken, which are fundamentally based on ray-tracing approach and SIRT. To verify effectiveness of the methodologies, numerical simulations of wave motion and experimental works were conducted for concrete with honeycomb defect, surface deterioration and partially grouted tendon duct. In this study, it was found that the travel time tomography was less sensitive than the amplitude tomography and frequency tomography in visualizing defect. However, with the use of Q-value as observed data in tomography reconstruction, visualization accuracy has improved substantially. The interpretation of results becomes more accurate by assessing and comparing tomography reconstructions of the three wave parameters. Following that, a new implementation procedure for tomography technique utilizing the proposed wave parameters is recommended to optimize instrumentation and signal processing potentially for reliable in-situ assessment purposes.

Abstrak

Kaedah penilaian tanpa musnah (NDE) dan pemantauan kesihatan struktur (SHM) telah menjadi teknologi yang amat penting dalam industri kejuruteraan awam. Kecacatan yang didapati dalam struktur baru ataupun lama akan menyebabkan kecederaan dan kehilangan nyawa. Oleh itu, pengesanan dan penilaian kecacatan dalam struktur harus dilaksanakan secara berkesan. Teknik tomografi adalah satu kaedah NDE untuk menilai kekukuhan struktur konkrit dengan memberikan visualisasi pedalaman struktur. Dalam kajian ini, tiga jenis sifat gelombang elastik telah dipertimbangkan dalam pembentukan kaedah pembinaan semula tomografi, iaitu perjalanan masa (hadlaju), amplitud dan frekuensi. Pembangunan algoritma untuk kaedah ini telah dilaksanakan, dimana pada asasnya adalah berdasarkan pencarian cara dan surih gelombang dan teknik pembinaan semula lelaran serentak (SIRT). Simulasi berangka gerakan gelombang dan eksperimen telahpun dilaksanakan dengan konkrit yang mempunyai kecacatan sarang lebah dan prategasan tendon sarung yang diturap dengan sebahagiannya untuk mengesahkan keberkesanan kaedah yang dibentuk. Kajian ini juga mendapati bahawa tomografi masa perjalanan adalah kurang peka jika dibanding dengan tomografi amplitud dan tomografi frekuensi dalam penggambaran kecacatan. Manakala, dengan pengunaan nilai-Q sebagai maklumat yang diperhatikan dalam pembinaan semula tomografi, ketepatan visualisasi telah bertambah baik. Taksiran untuk keputusan menjadi lebih tepat dengan penilaian dan pembandingan kaedah pembinaan semula tomografi bagi tiga jenis parameter gelombang. Berikutan itu, satu prosedur baru bagi pelaksanaan teknik tomografi menggunakan parameter gelombang telah dicadangkan untuk mengoptimumkan peralatan dan pemprosesan isyarat yang berpotensi untuk tujuan penilaian di-situ.

ACKNOWLEDGEMENTS

First and foremost, I would like to offer my sincere apprecation to my respected supervisor, Dr. Chai Hwa Kian for his excellent guidance, supports and suggestions throughout my thesis with his passion and knowledge. I also express my deepest gratitute for his precious time that he had spent in supervising my study, especially in corrected my writing and financially supported me without asking for any returns. He had also attribute my Master's degree with his knowlege in nondestructive evaluation field and his patient and encouragement finally made this project completed and successful. It is really lucky for me to have him as my supervisor.

Besides my supervisor, I would like to thank Dr Kobayashi Yoshikazu for his invaluable advice, help, supports and guidance on my project. Besides that, I would like to thank the help and technical support provided from all the staffs and lab assistants especially Mr. Mansor and Mr. Sreedharan at the Civil Engineering Department, University of Malaya. In addition, I would like to express my appreciation to the faculty members and friends in Faculty of Engineering, University of Malaya for their assistance and help throughout my Master study.

The last but not least, I would like to gratitute to Khor Pee Fen and my family for giving me support and encouragement to me for conducting this research.

TABLE OF CONTENTS

LIST OF FIGURES

LIST OF TABLES

LIST OF SYMBOLS AND ABBREVIATIONS

Symbols	Descriptions
$\emptyset_f$	Phase angle of component with frequency f.
C_b	Bar wave velocity
C_p	P-wave velocity
C_r	R-wave velocity
C_s	S-wave velocity
$c_{R(f)}$	Surface wave speed
σ^2	Variance
Δ	Change
E	Slowness
S	Slowness
V_L	Longitudinal wave speed
A	Attenuation coefficient
B	Absorption coefficient
N	Poisson's ratio
P	Density
A	Amplitude
D	Distance,

G	Shear modulus of elasticity
R	Fraction of the incident wave that are reflected and transmitted
Z	Acoustic impedance
f	Frequency
p	Density
t	Travel time
v	Velocity
θ	Angle of wave
λ	Wavelength
μ	Second lame constants
ϑ	First lame constants

Abbrevations	Descriptions
AE	Acoustic Emission
AT	Amplitude tomography
EM	Electromagnetic
FT	Frequency tomography
GPR	Ground-penetrating radar
IRT	Infrared thermography
Low Ec	Surface deteriorate layer
MIRA	The state-of-the art elastic wave tomography
NDE	Non-destructive evaluation (NDE)
PC	Prestressed concrete
P-wave	Primary wave
Q-Value	Medium quality factor
R-wave	Rayleigh wave
SASW	Spectral analysis of surface waves
SHM	Structural health monitoring
SIBIE	Spectral amplitudes based on impact-echo
SIRT	Simultaneous iterative reconstruction technique
S-wave	Secondary wave
TDR	Transient dynamic response
TTT	Travel time tomography
EWPV	Elastic wave pulse velocity
EWT	Elastic wave testing
EWTM	Elastic wave transmission method
X-ray	X-radiation

LIST OF APPENDICES

CHAPTER 1

GENERAL INTRODUCTION

1.1 Background of Study

There is a growing concern about the deterioration of concrete infrastructures in places all over the world. Detection of damage and understanding the behaviour of deteriorated structures has thus become vital practices in the civil engineering industry. Construction faults and design errors such as inadequate structural design and poor design detailing could lead to unexpected deterioration of concrete infrastructures. Besides that, excessive physical and environmental effects often result in the loss of structure’s integrity and increased effort in repair and have to be put up in time. To avoid aging infrastructures from further deteriorating, regular inspection is critical to detect and repair. Traditionally, destructive methods such as coring and drilling are commonly used for assessment of the concrete interior condition. These methods are time consuming, expensive and may turn out to be the focal point for deterioration in the future. In search for more effective means, technologies for NDE have been developed to offer alternatives in structural damage assessment. The NDE is a wide group of techniques that evaluate the properties of material, component or system without impairing its future usefulness. The ultimate aim of NDE is to detect defects of the interior structure accurately in order to proceed for specific repair action. Implementation of NDE is considered relatively simple, flexible and cost effective compared to the conventional coring and drilling methods. The results of evaluation are useful in providing warning or indication towards imminent failure. Some of the common NDE techniques for early stage damage detection of concrete structures include chain dragging method, GPR, EWPV, EM methods, and IRT (Malhotra and Carino, 2003 ; Ansari and Sture, 1992).

The tomography technique is an emerging NDE technique to visualise the condition of the inner structure without causing any damage. The application of tomography enables a better detection of anomalous regions and determination of the physical properties of the structures (Bond et al.,2000). One of the common tomography applications is X-ray, which is used for detecting defects in human bones. Due to high operating costs and harmful radiation, X-ray is not used in the civil engineering field. The tomography technique adopted for civil engineering industry is based on elastic or stress in structure, which are usually generated by mechanical impacts, such as tapping on the structure's surface. Elastic waves have energy from mechanical impacts and the speed of elastic waves is affected by properties of propagated medium. The energy of elastic waves is related to the frequency of wave and impact contact time with surface. The speed of waves, on the other hand, depends on the elastic properties of propagated medium, such as density, young's modulus and Poisson's ratio.

In general, the existing literature has investigated the elastic time tomography for wave velocity distribution, while the potential of other parameters of elastic waves have been overlooked. Therefore, this study is to investigate the applicability of the other elastic wave parameters such as amplitude, frequency and Q-value to provide visualized tomograms other than wave velocity. The algorithm of each technique is based on two basic principle which are ray-tracing and simultaneous iterative reconstruction technique. The ray-tracing approach is used in tomography reconstruction of elastic waves to determine the wave propagation and its displacement, mathematical model such as SIRT is used to update the mesh information of testing structure. In order to verify the developed algorithms, seismic tomography and experimental work cases have been carried out by using concrete with honeycomb defect and partially grouted pre-stressed tendon sheath.

1.2 Problem Statement

In the construction industry, design errors and construction defects are some of the common factors that may affect the safety and service life span of civil structures. For example, a honeycomb defect in concrete structure due to poor compaction caused reduces the stiffness of the structure. Besides that, deterioration of concrete is a time-dependent process which severely affects durability, service life, maintenance costs and structural integrity of concrete structures. Corrosion-induced delamination of concrete causes the structure to further deteriorate as a result of the penetration of water and chemicals into concrete, increases the corrosion rate of reinforcing steel. It is thus important to assess deteriorated concrete for detecting and evaluating defect that could hamper structural integrity.

Various types of non-destructive testing (NDT) methods have been used for assessment of concrete NDT methods were being used for concrete infrastructure evaluation. However, “imaging” or “visualization” defects in concrete facilities better understanding of the structure interior. The elastic wave tomography has been recognised as one of the appropriate methods for such purpose. To develop simplest and robust tomography technique, this study is engaged by developing and comparing four types of wave parameters used for tomographic reconstruction process, namely travel time, amplitude, frequency and the Q-value. The results of tomography assessment provide useful information for effective maintenance of structures. In addition, the structure tomograms can be stored to facilitate effective remedy after years if any repair is needed (Aggelis & Shiotani ,2007 ; Shiotani et al, 2009). This is because there is no standard difference wave range or speed and attenuation coefficient between the sound concrete and concrete with defects. This study aims to explore the optimum wave properties (source frequency and energy of excitation) and instrumentation conditions (sensor arrangement, geometry and mesh size) of these four techniques in the evaluation of the defects.

1.3 Research Objectives

The objectives of this study are as follows:

- To develop tomographic reconstruction algorithm based on ray tracing principles with Simultaneous iteration reconstruction technique (SIRT) as numerical solution to update the quality of the concrete inner structure.
- To establish tomography assessment procedures using different wave parameters, namely velocity, amplitude, frequency and the Q-value by wave simulation and laboratory measurements.
- To establish the configurations of evaluation ranges for the different wave parameters for optimising results of tomography assessment.
- To compare and evaluate effectiveness of the different wave parameters for use in tomography assessment of concrete with various types of defects, including honeycomb, void and surface deterioration.

1.4 Scope of Research

The fundamental principles of elastic wave tomography were studied, discovered in particular ray tracing approach and SIRT for solving inverse wave propagation problems. In addition, computer programming was carried out to update mesh's elastic wave speed and attenuation coefficient. The developed elastic wave tomography techniques algorithms were verified with numerical simulations and laboratory measurements such as detection of concrete surface deterioration, concrete honeycomb and concrete with partially grouted pre-stressed tendon sheath. Extraction of the wave information was done for simulation and experiment. Parameters such as offset time, first peak amplitude were obtained from time domain while central frequency from the frequency domain. The results of tomography were critically analysed in qualification and quantification. The study has resulted in a new implementation procedure for elastic wave tomography to optimise instrumentation and signal processing for in-situ applications.

1.5 Outline of Thesis

This thesis includes five chapters. Chapter One contains general introduction to this study on the background of NDE and elastic wave tomography, the problem statement, research objectives and scope of research. Chapter Two provides literature review in which describes and reviews on related articles was done. The factors that contribute to concrete deterioration and types of defects in concrete structures were being reviewed. In addition, the stress wave properties, NDE techniques and recent related technology of elastic wave tomography were reviewed in this chapter. Chapter Three is the research methodology. It included software that was used and principle of numerical simulations to obtain raw data. In addition, the instruments used to obtain the waveform from the experimental work were included. Sensors arrangement, material properties etc. were also explained in this chapter.

Chapter Four included tomography results in qualification and quantification. The new implementation procedure for elastic wave tomography technique was proposed to optimise instrumentation and signal processing potentially for in-situ assessment applications. The chapter five of this dissertation presented the conclusion based on analysis and discussion of the numerical simulations and experimental. Chapter Five suggest on the possible future works. The developed tomography algorithms and the supporting data and analysis were included in the Appendix.

CHAPTER 2

LITERATURE REVIEW

2.1 Introduction

Concrete is a strong and durable material that can be used to build houses, bridges, road, dams and many more. However, there are risks of concrete which possibly to causes causality due to concrete deterioration. In order to avoid collapse of a deteriorated structure or other disaster, proper preventive maintenance has to be carried out. NDE has to be carried out to detect which part of concrete structure is defected so that repair work can be carried out rapidly and cost efficiently. Besides, it is encouraged to conduct inspection on a regular basis so that necessary considerations and effective repair action can be implemented. There are various NDE techniques that have been practiced by engineers in detecting defects and evaluating the integrity of structures depending on the physical conditions of concrete structures.

There are various NDE techniques such as impact echo (IE), Ground Penetrating Radar , pulse eddy-current (PEC), Parallel-seismic method, Sonic-echo method and acoustic emission (AE), that can be used either locally or globally (Cheng, Y. et.al, 2015; Farhidzadeh, A. et. Al, 2014; Tian, G.Y et. al,2005; Schabowicz, K., 2014;). The unique advantages of employing NDE include time and cost saving, flexibility in operation, and simple implementation. Each techniques can be used for specific conditions. For example, IE can be used to find out the thickness of different layers of medium, or PEC can be utilized for surface crack detection, whereas the EWT technique uniquely facilitates visualization inspection so that anomalous regions or distribution of physical properties in the measured object can be visualized (Shiotani, T. et.al., 2016). The EWT technique is an emerging local NDE technique for civil engineering applications which utilizes the principal of elastic wave propagation to detect defects in a medium. Therefore, it can be utilized to evaluate the soundness of a concrete medium by analyzing the changes in stress wave propagation. Tomogram can be plot by several elastic wave parameters such as amplitude, frequency and medium quality factor (Q-value) to provide visualized tomograms other than traditionally wave velocity.

2.2 Factors Contributed to Concrete Deterioration

Generally, deterioration in concrete structures can be due to the following factors and were being discussed in this chapter.

- Errors in design calculations and detailing
- Improper selection of materials
- Poor construction method, inadequate quality control and supervision
- Chemical attack

2.2.1 Errors in design calculations and detailing

Structure designing is a preliminary stage of construction project. The objective of structure designing calculations is to ensure that the selection of sizes, slab thickness, reinforcement sizes and spacing specified are adequate to carry the worst combination of design loads. The designs included overall stability, robustness and serviceability and foundation design. Inaccurate detailing was one of the common reasons for failure and cracking in concrete structures. The detailing errors included wrong thickness of cover, maximum and minimum steel areas and bar spacing limit (Bhatt et al., 1990).

2.2.2 Improper selection of materials

The concrete mix design was affected by the environment or soil conditions of the site of concrete structure. Higher grades of concrete mix was considered when the construction site was an aggressive industrial area or nearby sea. Presence of sulphate in concrete causes freezing and thawing and thus leads to air entrainment (Li et al., 2011). The careless mistake made by general worker could lead to the faulty structure.

2.2.3 Poor construction method and inadequate quality control and supervision

The poor construction methods were resulting from bad workmanship and inadequate quality control and supervision. Some examples of poor construction included improper placement, inadequate cover of reinforcement and poor compaction which resulted honeycomb concrete. Besides, grout leakage happened when formwork joints were not sealed properly and causes porous areas of concrete with little or no cement and fine aggregate. The other instance was segregation resulted from the separation of mixed ingredients. Segregation results in uneven concrete mixture or porous concrete.

2.2.4 Chemical attack

Four types of chemical attack that were commonly found on concrete and reinforcement are chlorides, sulphates, carbonation and alkali-silica reaction. The chloride attack causes corrosion of reinforcement and concrete disruption which was found among the concrete structures that are nearby sea or contain high concentration of calcium chloride. On the other hand, sulphate attack causes disintegration of concrete and corrosion of steel where sulphate was found in soils, groundwater, seawater, industrial wastes and acid rain. Carbonation happened when carbon dioxide from the atmosphere slowly transforms calcium hydroxide into calcium carbonate in concrete. However, carbonation does not reduce the concrete strength but it corrodes the reinforcement. Standard carbonation depth of dense concrete is about 6-10mm after 30-40 years but poor concrete may have a depth of carbonation of 50 mm after 6-8 years. The rate of carbonation was affected time, cover, concrete density, cement content, water to cement ratio and presence of cracks. The gel formed in alkali-silica reaction absorbs water, increase in volume and thus resulted in concrete disintegration and crack which commonly take place in cement and aggregate.

2.3 Common Defects in Concrete Structures

The deterioration of concrete structures was found to be due to various physical and environmental damages. Three common types of concrete flaw found were delamination, cracks and voids or honeycomb.

2.3.1 Voids and Honeycomb

Based on Zhu & Popovics (2007) study, the formation of voids and honeycomb were caused by poor consolidation of concrete during construction. The honeycomb was defined as the presence of spaces or voids in concrete because of the incomplete filling of mortar into spaces between the coarse aggregate particles. A few factors that contributed to the honeycomb structures include stiff or unworkable concrete, segregation, congested rebar, insufficient consolidation, and improper placing practices. The honeycomb significantly reduced the strength of concrete and may collapse in the long term. Portland cement grout was used in post-tensioned structures to provide a bond between tendons and surrounding concrete. It acted as corrosion protection for the tendons as it is the last layer against ingress of chlorides to the pre-stressed strands. Poor grout design or procedure may causes trapped air pockets or bleeding water pockets which may form voids in the post-tensioned ducts and thus lead to corrosion. Tendon failures may result from the large tensile stress exerted on it and causes failure of the concrete member which seriously damages the whole structure.

2.3.2 Delamination

Corrosion of reinforcing steel, freezing and thawing of concrete were some of the examples of concrete delamination. It causes serious problem in civil structures' service life which is common in bridge decks and parking garage slabs. Concrete delamination happened when the concrete cover is permeable by water and air. Corrosion of steel destroyed the bond between the steel and the surrounding concrete, which was accelerated when it has a higher permeability. Environmental factor has become the major causes for delamination due to uneven drying as the underlying concrete is still in a plastic state with bleeding water. Vapour barriers that exist in concrete cause water to migrate from a cooler region to warmer region and thus increase the potential for delamination.

The presence of chloride ions (from deicing salts) could accelerated the process of corrosion, chloride ions normally diffused through the cover layer of concrete to the moist region of the reinforcing steel surface. Corrosion causes the reinforcing steel volume to expand which stressing the surrounding concrete and lead to the crack of the structure. Generally, delamination cracking spreads in the plane of the top reinforcing steel layer and parallel to the surface, which is typically 5 cm to 15 cm below the bridge deck surface. The delamination will eventually spread to the surface and resulted in spalled concrete. Polyethylene sheath was a preventive measure used to prevent water from entering the tendons and causes delamination.

2.3.3 Cracks

Concrete crack was caused by drying shrinkage, thermal expansion, freeze-thaw cycles, chemical reaction or mechanical actions such as fatigue or overloading. The crack can be classified into three categories: direction, width and depth of the crack in longitudinal, transverse, vertical, diagonal or random. The existence of crack affects concrete structure's serviceability and reduced its durability. Crack allowed ingress of deleterious chemicals such as waterborne deicing salts may lead to corrosion of steel reinforcement. A distinct single surface-breaking crack was commonly found and significant defect can eventually lead to failure of concrete structures. Determining the size (width and depth) of cracks is essential for structural integrity assessment of the concrete structures (Zhu and Popovics, 2007).

2.4 Non-destructive Testing (NDT) Methods

NDT was used to detect defects and quantify the properties of material, component or structural (Bretsse et al., 2008). NDT is flexible in its operation and easy to implement. The time spent on NDT was shorter and the cost is lower compared to other techniques. It is vital to conduct inspection on a regular basis so that necessary considerations and effective repair action can be implemented on time. The results are useful in providing warning or indication towards imminent failure. There are various non-destructive techniques (NDT) that have been practiced by engineers in detecting defects and evaluating the integrity of structures. There are two types of well-known NDT techniques which are active technique and passive technique. For active technique, the source emitting is applied to the surface of the concrete member as illustrated in Figure 2.1. While, for passive technique the source is generated within the material and it produces as a test signal as illustrated in Figure 2.2. there are various NDT method which includes visual inspection, AE, ground penetrating method (GPR), impact-echo method, impulse response method, IRT, parallel-seismic method, sonic-echo method, SASW method, Elastic Wave Transmission Method (EWTM) and stress wave tomographic reconstruction technique.

Figure 2.1: NDE principle using active techniques.

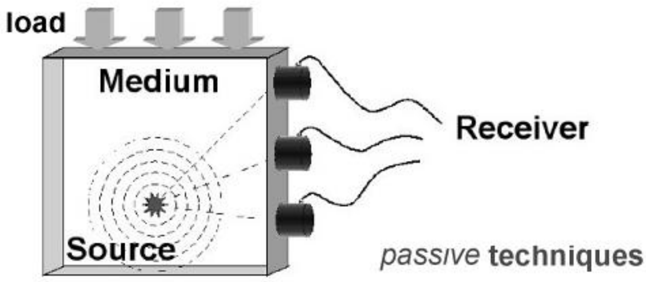

Figure 2.2: NDE principle using passive techniques (Grosse & Ohtsu, 2008).

2.4.1 Visual Inspection

Visual inspection is one of the initial evaluations of a concrete structure to provide information to help in identifying the cause of observed distress (Perenchio, 1989). Visual inspection is very useful and costless but the investigator has to be acquired with skills, knowledge and experience. In order to extract more information from the visual inspection, broad knowledge in structural engineering, concrete materials and construction methods is needed. Some defects that could be noticed by visual inspection are surface cracking, concrete bending, holes, corrosion and impact damage. However, the method is limited as it only applicable on the visible surfaces of concrete but not the internal defects. Furthermore, no quantitative information can be obtained for the findings. Therefore, a visual inspection is usually supplemented by a series of other NDT methods.

2.4.2 Ground Penetrating Radar (GPR)

GPR is a geophysical technique that used EM radio waves to determine or detect thickness, delamination, large voids, extensive defects and reinforcement bars in concrete and reinforced concrete elements. The EM waves are radiated from a transmitter which sends a signal to the ground. The waves are diffracted, refracted and reflected to the surface. The waves are measured by a receiver unit, amplified and digitized by the computer unit that is used to record the measurement as shown in Figure 2.3 (Meyers et al., 1996; Arnevik A. ,n.d.). Radar technique can be used to detect delamination in concrete bridge desks, monitor the strength and determination of water content in fresh concrete, measure thickness of concrete member, and locating rebar (Clemena, 2004).

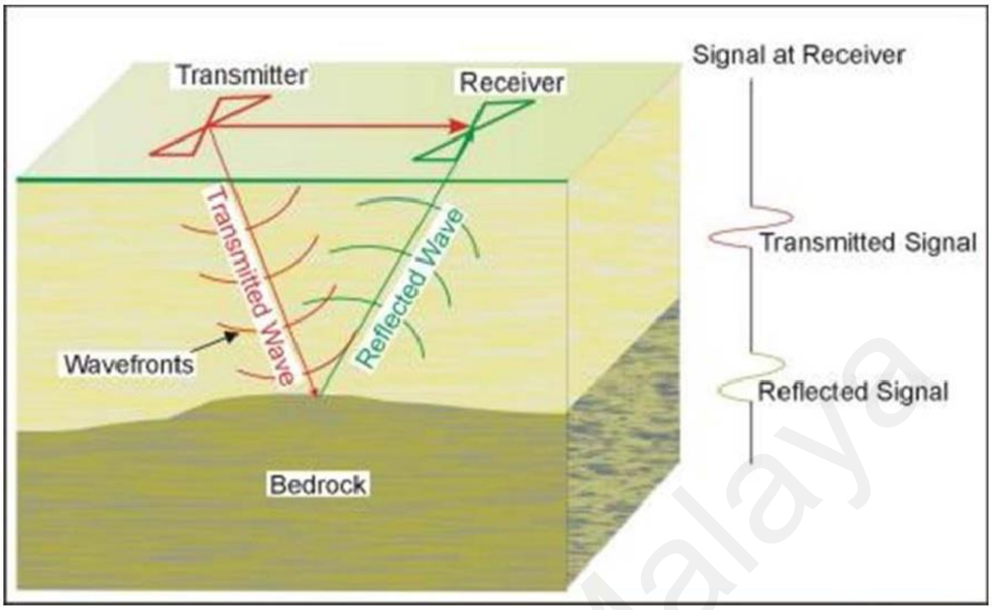

Figure 2.3: Schematic of how the EM wave is transmitted and reflected by a GPR unit (Meyers et al., 1996).

A reflection of the wave is due to the subsurface materials having different dielectric properties (Davis and Annan, 1989). When EM transmits from a medium to another medium with different properties, a reflected wave will be produced. The EM wave travel on its own velocity as the material has its own conductivity level. Using the reflections and the two-way elapsed time of the EM pulse's travel, a cross-sectional reflection profile can be created. The profile can be made in real time from a computer where the collection of the reflected EM data took place.

The typical instrumentation for GPR included an antenna/sensor unit, a control unit, a display device and a storage device. The antenna, which is dragged across the surface or attached to a survey vehicle, transmits short pulses of EM energy that penetrate into the surveyed material. Each pulse travels through the material and a portion of the energy is reflected back to the antenna where an interface between materials with dissimilar dielectric properties is encountered. The antenna receives the reflected energy and generates an output signal proportional to the amplitude of the reflected EM field. The GPR method is very sensitive to the presence of embedded metal objects, but not cracks and delamination unless the defect region is moist (ACI Committee 228, 1998). Buyukozturk (1998) reviewed that radar technique such as the EM wave method can rapidly locate and image defects in the concrete structures effectively. However, radar technique was found to have imaging limitations such as diffraction, which might affect the visualization, lack of exact inversion algorithms, loss of polarization information due to scalar inversion and high attenuation of EM waves in moisture (Buyukozturk, 1998). A study done by Langenberg et al. to assess the condition of pre-stressed concrete tendon duct by using EM wave found that the EM wave was limited as it was being shielded by the steel grid and the tendon duct itself (Langenberg et al., 2006).

2.4.3 Infrared Thermography

IRT is a process in which heat at any temperature can be converted into a thermal image using specialized scanning cameras. IRT has been used to detect subsurface anomalies within and below concrete elements. It has been observed that buildings or structures with defects emit different amounts of infrared radiation. If a concrete surface with an even colour and texture is viewed with an infrared camera, it will appear quite uniform when the concrete is free from defects. However, if there is any crack or delamination within the concrete, the surface will heat up faster under solar irradiation in this area and hot spot can be observed in the thermal record. Thus, this area can be examined more closely and marked on the surface for identification and future investigation (McCann & Forde, 2001). IRT covers a greater area than other test methods. However the depth and thickness of a subsurface anomaly cannot be measured and it is more difficult to detect as the depth of the anomaly increases. This method is effective for penetration up to 10 cm and identification is only good at an early stage of concrete hardening (Rieck & Hillemeier, 2003). However, Clark et al. found that weather and surface conditions can affect the accuracy of imaging by impulse thermography (Clark et al., 2003).

2.4.4 Parallel-seismic method

The parallel-seismic method was developed specifically to determine the foundation depth has been built upon and the quality in which the pile head is no longer possible without some demolition (Davis, 1995). This method belongs to low-energy seismic methods and requires a small-diameter access bore hole which is drilled into the soil parallel and close to the foundation to be tested. The bore hole must extend beyond the known or estimated depth of the foundation and lined with a plastic tube to retain water as acoustic couplant. An acoustic receiving probe is placed in the tube at the top and the structure is struck as close as possible to the head of the foundation with a source hammer. The signals from the hammer and receiver are recorded on a data acquisition unit as the time taken for the impact stress wave to travel through the foundation and adjacent soil to the receiving probe. The probe is then lowered in uniform increments and the process repeated at each stage, with the impact at the same point each time. The recorded data were plotted as a vertical profile with each wave transit time from the point of impact to each position down the access tube (ACI Committee 228, 1998). The advantage of using this method is the foundations under existing structures can be tested. The drawback is the necessity of boring a hole in the ground along the side of the investigated element which is not always possible.

2.4.5 Sonic-echo method

The sonic-echo method is the earliest NDT method to become commercially available (Steinbach & Vey, 1975) for deep-foundation integrity or length evaluation. The sonic-echo method can be used to determine the depth of the foundation based on the time separation between the first arrival and the first reflection events or between any two consecutive reflection events. This method used a small impact delivered at the head of the deep foundation (pile or shaft) and the time taken for the stress wave generated by the impact to travel down the pile and to be reflected back to a transducer (usually an accelerometer) coupled to the pile head is measured. The impact is typically from a small sledgehammer (hand sledge) with an electronic source. The time of impact and the pile head vertical movement after impact is recorded either by an oscilloscope or by a digital data acquisition device that records the data on a time base. Sonic echo also can be used to locate defects, intrusions and bulbs in the foundation or pile damage such as breaks or cracks.

2.4.6 Stress-wave methods

Stress wave is generated by the oscillatory motion of particles in a medium and it occurs when pressure or deformation is applied suddenly, such as by impact to the surface of a solid. The velocity of wave propagation is influenced by the material properties of the medium. The speed of stress-wave propagation in an elastic solid is a function of the modulus of elasticity, Poisson's ratio, the density, and the geometry of the solid. The disturbance will be occurring on the wave when it propagates through the solid in a manner analogous to the way sound travels through air. The interdependence between the properties of a solid and the resultant stress-wave propagation behaviour permits inferences about the characteristics of the solid by monitoring the propagation of stress wave. When pressure is applied suddenly at a point on the surface of a solid half-space, the disturbance propagates through the solid as three wave types as illustrated in Figure 2.4. Seismic wave consists of body waves and surface wave (also called as R-waves). Body wave includes P-wave (compression wave) and S-wave (shear wave) in which P-wave is the fastest among all three waves. The P-wave and S-wave propagate into the solid along hemispherical wave fronts. The P-wave is associated with the propagation of normal stress and particle motion is parallel to the propagation direction. The S-wave is associated with shear stress and particle motion is perpendicular to the propagation direction. In addition, an R-wave travels away from the disturbance along the surface. Chai et al. (2010) have utilized R-wave plotted interior defect of concrete by only single-side sensors access. In an isotropic, elastic solid, the P-wave speed C_p is related to Young's modulus of elasticity, E; Poisson's ratio, v; and the density, ρ as follows (Krautkrämer and Krautkrämer, 1990) :

$$C_p = \sqrt{\frac{E(1-\nu)}{\rho(1+\nu)(1-2\nu)}} \qquad \text{Equation 2.1}$$

The S-wave propagates at a slower speed C_s given by (Krautkrämer and Krautkrämer, 1990):

$$C_s = \sqrt{\frac{G}{\rho}} \qquad \text{Equation 2.2}$$

Where G = the shear modulus of elasticity.

The ratio of S-wave speed to P-wave speed is given as

$$\frac{C_s}{C_p} = \sqrt{\frac{(1-2\nu)}{2(1-\nu)}} \qquad \text{Equation 2.3}$$

Since that Poisson's ratio of 0.2, which is typical of concrete, this ratio equals 0.61. The ratio of the R-wave speed C_r to the S-wave speed may be approximated by the following formula (Krautkrämer and Krautkrämer, 1990)

$$\frac{C_r}{C_s} = \frac{0.87+1.12v}{1+v} \qquad \text{Equation 2.4}$$

In the case of bounded solids, the wave speed is also affected by the geometry of the solid. For wave propagation along the axis of slender bar, the wave speed is independent of Poisson's ratio and is given by the following

$$C_b = \sqrt{\frac{E}{\rho}}. \qquad \text{Equation 2.5}$$

Where C_b is the bar wave speed. For a Poisson's ratio between 0.15 and 0.25, the wave speed in a slender bar is from 3 to 9 % slower than the P-wave speed in a large solid.

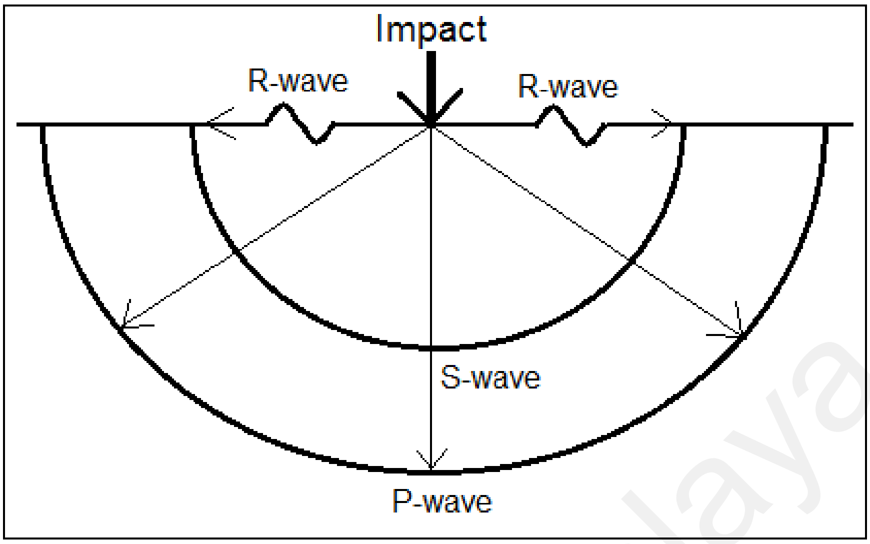

Figure 2.4: An illustration of body wave and surface wave propagates from a source point.

In this study, the main focus is on P-waves of body waves. Body waves travel through the interior of a solid medium and the information on body wave can be utilised to determine the material properties of the medium. P-waves are the fastest propagating waves in solids and can travel through both solids and fluids. P-waves of body waves include primary, longitudinal, dilatational or compression waves.

When seismic waves propagate in a medium, attenuation takes place which will contribute to the reduction in amplitude or energy content of waves. There are five factors that lead to the attenuation of seismic waves occurs:

(a) Geometrical attenuation

This is because the propagation of a wave front passes through a progressively larger volume of material. The effect is changing of the energy content of the wave but not the wave speed.

(b) Material attenuation

It occurs through the conversion of elastic energy into other forms of energy. Material attenuation occurs through internal friction because of the non-elastic response of the material and through friction at the boundaries. The amount of material attenuation mainly depends on the material, velocity of motion and also the frequency of vibration.

(c) Reflection and transmission at interfaces

When the waves propagate across with different elastic properties, the reflection and transmission of waves occur. After waves is reflected and transmitted, the nature and the distribution of wave energy can be determined by the theory of elasticity (Kramer, 1996). The speed and the amplitude of the waves are changed at the interface. The speed of the wave in new medium is depends on the properties of the first medium and direction of incident wave which is described by Snell's law:

$$\frac{Sin\ (\theta_a)}{v_a} = \frac{Sin\ (\theta_b)}{v_b} \qquad \text{Equation 2.6}$$

In which θ_a is the angle of wave and v_a is velocity in incident medium. In addition, $\theta_b$is angle of wave and v_b is velocity in reflected medium. The fraction of the incident wave that are reflected and transmitted, R can be determined by the equation:

$$R = \frac{(Z_2 - Z_1)}{(Z_2 + Z_1)} \qquad \text{Equation 2.7}$$

In which Z_1 and Z_2 are the acoustic impedance (product of the density and velocity) of the incident and reflected wave propagate medium material. Deploys from Sansalone and Carino (1991), the acoustic impedances of various materials compared with its density and velocity of ray path are shown in this table:

Table 2.1 Example of Density, velocity of pulse and acoustic impedance of few materials.

Material	Density (kg/m^3)	Velocity of pulse (m/s)	Acoustic impedance, Z ($g/cm^2s \times 10^5$)
Air	1.205	343	0.413×10^{-5}
Concrete	2300	3000-4500	6.9-10.4
Granite	2750	5500-6100	15.1-16.8
Limestone	2690	2800-7000	7.5-18.8
Marble	2650	3700-6900	9.5-18.3
Quartzite	2620	5600-6100	14.7-16.0
Soils	1400-2150	200-2000	0.28-4.3
Steel	7850	5940	46.6
Water	1000	1480	1.48

(d) Mode conversion

The wave will experience mode conversion when it encounters an interface between materials with different acoustic impedance at an incident angle not normal to the interface; other types of waves than reflection or transmission are generated.

(e) Scattering at interfaces and defects.

When a wave encounters a discontinuity or inhomogeneity in the medium, scattering of waves occur. Therefore, the inhomogeneity of propagate medium causes reflection and transmission of waves in multiple direction. The amount of energy scattered depends on the size of the inhomogeneity and the wavelength of the wave. The wavelength of propagating wave is smaller than the size of the inhomogeneity medium if the scattering is in the form of reflection, refraction and mode conversion. Whereas, if the wavelength of propagating wave is longer than the inhomogeneity medium, the waves will propagate in the medium with properties that reflect the existence of the inhomogeneity. If the size of inhomogeneity is constant, the portion of the energy scattered is inversely proportional to the wavelength.

2.4.6.1 Elastic Wave through Transmission method

Elastic wave transmission method is also known as EWPV method. The principle is based on the speed of propagation of stress waves depends on the density and the elastic constants of the solid. In a concrete member, variations in density can arise from non-uniform consolidation, and variations in elastic properties can occur due to variations in materials, mix proportions, or curing. Thus, by determining the wave speed at different locations in a structure, it is possible to make inferences about the uniformity of the concrete. The compressional wave speed is determined by measuring the travel time of the stress pulse over a known distance.

This approach has been suggested to measure the depth of a fire-damaged surface layer having a lower wave speed than the underlying sound concrete (Chung and Law, 1985) and the depth of concrete damaged by freezing (Teodoru and Herf, 1996). The test is carried out by measuring the travel time as a function of the separation between transmitter and receiver, X. The method assumes that stress-wave arrival at the receiver occurs along two paths: Path 1, which is directly through the damaged concrete, and Path 2, which is through the damaged and the sound concrete as illustrated in Figure 2.5(a). For small separation, the travel time is shorter for Path 1, and for large separation the travel time is shorter for Path 2. By plotting the travel time as a function of the distance X, the presence of a damaged surface layer is indicated by a change in the slope of the data. The distanceX_o, at which the travel times for the two paths are equal, is found from the intersection of the straight lines as shown in Figure 2.5(b). The slopes of the two lines are reciprocals of the wave speeds in the damaged and sound concrete. The depth of the damaged layer is found from the following (Chung and Law, 1985). The studied suggests that lower-frequency transducers are used for mass concrete (20 kHz) and higher-frequency transducers (> 100 kHz) are used for thinner members where accurate travel times have to be measured. In most applications, 50-kHz transducers are suitable.

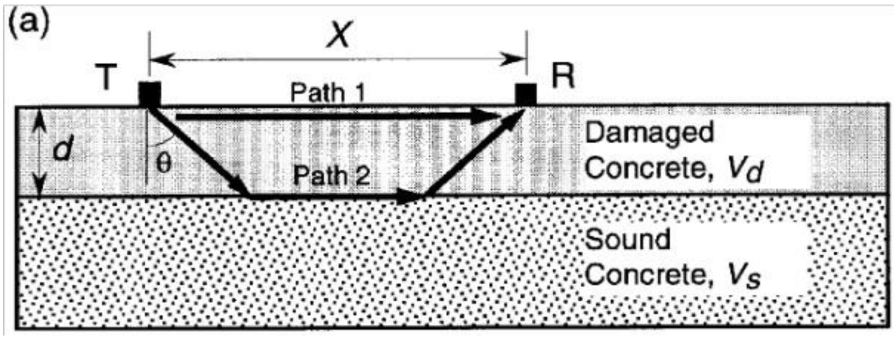

Figure 2.5 (a): Wave paths for EWT through a surface of concrete with damaged surface damaged. (ACI Committee 228, 1998).

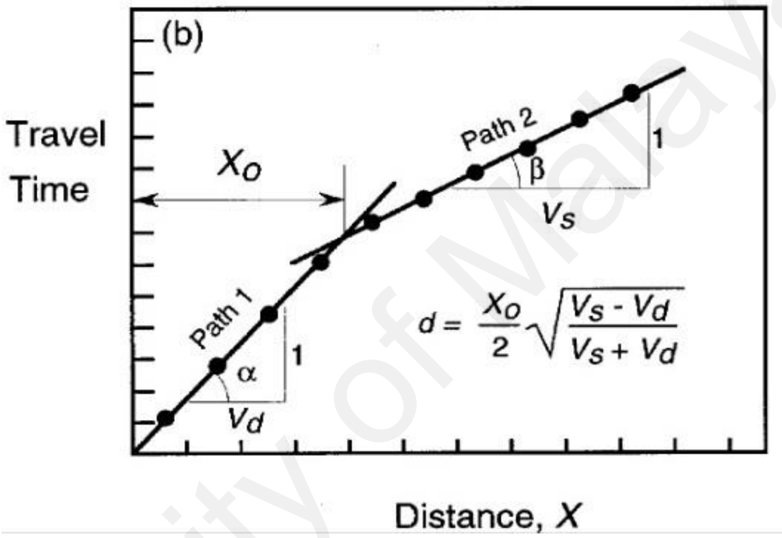

Figure 2.5(b): The relationships between travel time and distance between transmitter and receiver. (ACI Committee 228, 1998).

2.4.6.2 Elastic wave -echo method

There are some structures in which it is impossible to attach sensors on both sides of the member and the lack of information on the location (depth) of a detected anomaly. These limitations can be overcome by using the echo methods, in which the testing is performed on one face of the member and the arrival time of a stress wave reflected from a defect is determined. This approach has been developed for testing metals, and it is known as the pulse-echo method. Since the 1960s, many experimental elastic wave-echo systems have been developed for concrete (Bradfield and Gatfield, 1964; Howkins, 1968). Successful applications have been limited mainly to measuring the thickness of and detecting flaws in thin slabs, pavements, and walls (Mailer, 1972; Alex and Thornton, 1989).

In the pulse-echo method, a stress pulse is introduced into an object on an accessible surface by a transmitter. The pulse propagates into the test object and is reflected by flaws or interfaces. The surface response caused by the arrival of reflected waves, or echoes, are monitored by the same transducer acting as a receiver. This technique is illustrated in Figure 2.6(a). Due to technical problems in developing a suitable pulse-echo transducer for testing concrete, successful elastic wave-echo methods had used a separate receiving transducer located close to the transmitting transducer. Such a system is known as pitch-catch, and is illustrated in Figure 2.6(b). The receiver output is displayed on an oscilloscope as a time-domain waveform. The round-trip travel time of the pulse can be obtained from the waveform by determining the time from the start of the transmitted pulse to the reception of the echo. If the wave speed in the material is known, this travel time can be used to determine the depth of the reflecting interface.

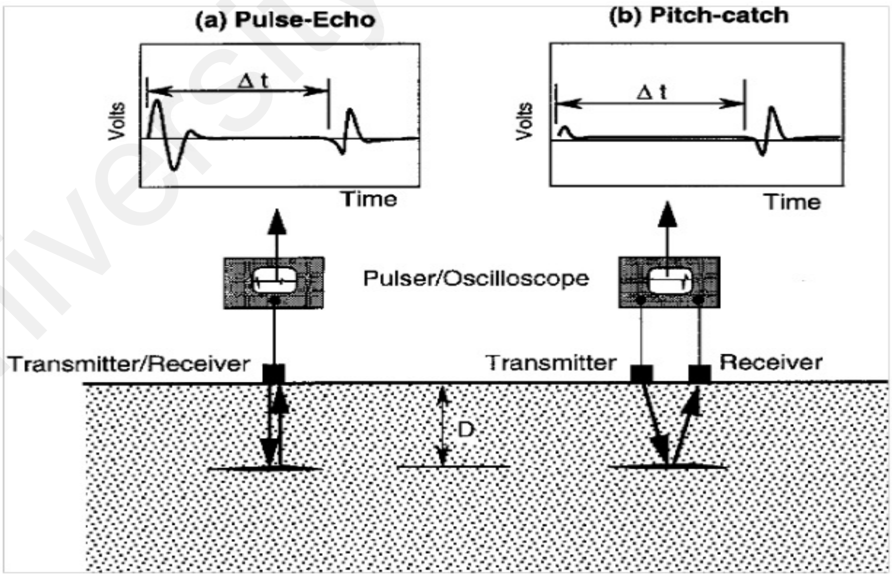

Figure 2.6: Schematic of elastic wave: (a) pulse-echo and (b) pitch-catch methods.

2.4.6.3 Impact-echo method

This method used an impact to generate a stress pulse is an old idea that has the advantage of eliminating the need for a bulky transmitting transducer and providing a stress pulse with greater penetration ability. However, the stress pulse generated by impact at a point is not focused like a pulse from an elastic wave transducer. Instead, the waves propagate into a test object in all directions, and reflections may arrive from many directions. Impact-echo method has been successfully applied to locate defects, flaws, inclusions, and voids in concrete structures (Sansalone and Streett, 1997).

Figure 2.7(a) shows the schematic of impact-echo method. A transient stress pulse is introduced into a test object by mechanical impact on the surface. The P-waves and S-waves produced by the stress pulses propagate into the object along hemispherical wave front. In addition, a surface wave travels along the surface away from the impact point. The waves are reflected by internal interfaces or external boundaries. The arrival of these reflected waves, or echoes, at the surface where the impact was generated produces displacements that are measured by a receiving transducer and recorded using a data-acquisition system. Interpretation of waveforms in the time domain has been successful in seismic-echo applications involving long slender structural members, such as piles and drilled shafts(Steinbach and Vey, 1975; Olson and Wright, 1990).In such cases, there is sufficient time between the generation of the stress pulse and the reception of the wave reflected from the bottom surface, or from an inclusion or other flaw, so that the arrival time of the reflected wave is generally easy to determine even if long-duration impacts produced by hammers are used. For relatively thin structural members such as slabs and walls, time-domain analysis is feasible if short-duration impacts are used, but it is time-consuming and can be difficult depending on the geometry of the structure (Sansalone and Carino, 1986). The preferred approach which is much quicker and simpler is frequency analysis of displacement waveforms (Carino et al., 1986). The underlying principle of frequency analysis is that the stress pulse generated by the impact undergoes multiple reflections between the test surface and the reflecting interface (flaw or boundaries). The frequency of arrival of the reflected pulse at the receiver depends on the wave speed and the distance between the test surface and the reflecting interface. In the case of reflections in a plate-like structure, this frequency is called the thickness frequency, and it varies as the inverse of the member thickness.

In frequency analysis, the time-domain signal is transformed into the frequency domain using the fast Fourier transform technique. The result is an amplitude spectrum that indicates the amplitude of the various frequency components in the waveforms. The frequency corresponding to the arrival of the multiple reflections of the initial stress pulse that is the thickness frequency is indicated by a peak in the amplitude spectrum. For a plate-like structure, the approximate relationship between the distance, D to the reflecting interface, the P-wave speed C_p and the thickness frequency, f is as follows

$$\mathrm{D} = \frac{C_p}{2f} \qquad \text{Equation 2.8}$$

For example, a case 0.5 thick solid concrete slab of Figure 2.7(b) was tested with impact-echo method. The amplitude spectrum corresponds to the case Figure 2.7(b) shows a peak at 3.42 kHz and a velocity of 3420 ms^{-1} is calculated. Figure 2.7(c) shows the amplitude spectrum for a test over a void within the same slab. The peak has shifted to a frequency of 7.32 kHz, which indicates the reflections are occurred from an interface within the slab. The ratio of 3.42 kHz/ 7.32 kHz = 0.46 indicated the interface is at approximately the middle of the slab with a calculated depth of 0.23 m. However, this impact-echo is not always accurate because many peak frequencies are observed in the frequency spectra due to reflection, diffraction, and so forth. To circumvent this, a new procedure was developed by applying an imaging procedure to the impact-echo data, as stack imaging of SIBIE (Alver et al.,2007; Ohtsu & Watanabe, 2002). Alver and Ohtsu had conducted lab tests regarding SIBIE procedure which was found to be efficient in identifying specimens containing grouted and ungrouted ducts (Alver & Ohtsu, 2007). MIRA is a device manufactured by Acoustic Control Systems, which contains four rows of sensors in which each row contains ten transducers. The impact-echo needs one receiver sensor for one measurement, while the MIRA used the same concept as impact-echo. MIRA is an elastic wave tomography device that was developed to determine the depth of concrete pavement and reinforcement location as well as detection of flaws in concrete pavement or PC. However, it is suggested to use the MIRA with combination of other NDT techniques because of the inability of the device to determine the exact location of flaws at big areas by short time (Hoegh et al., 2011).

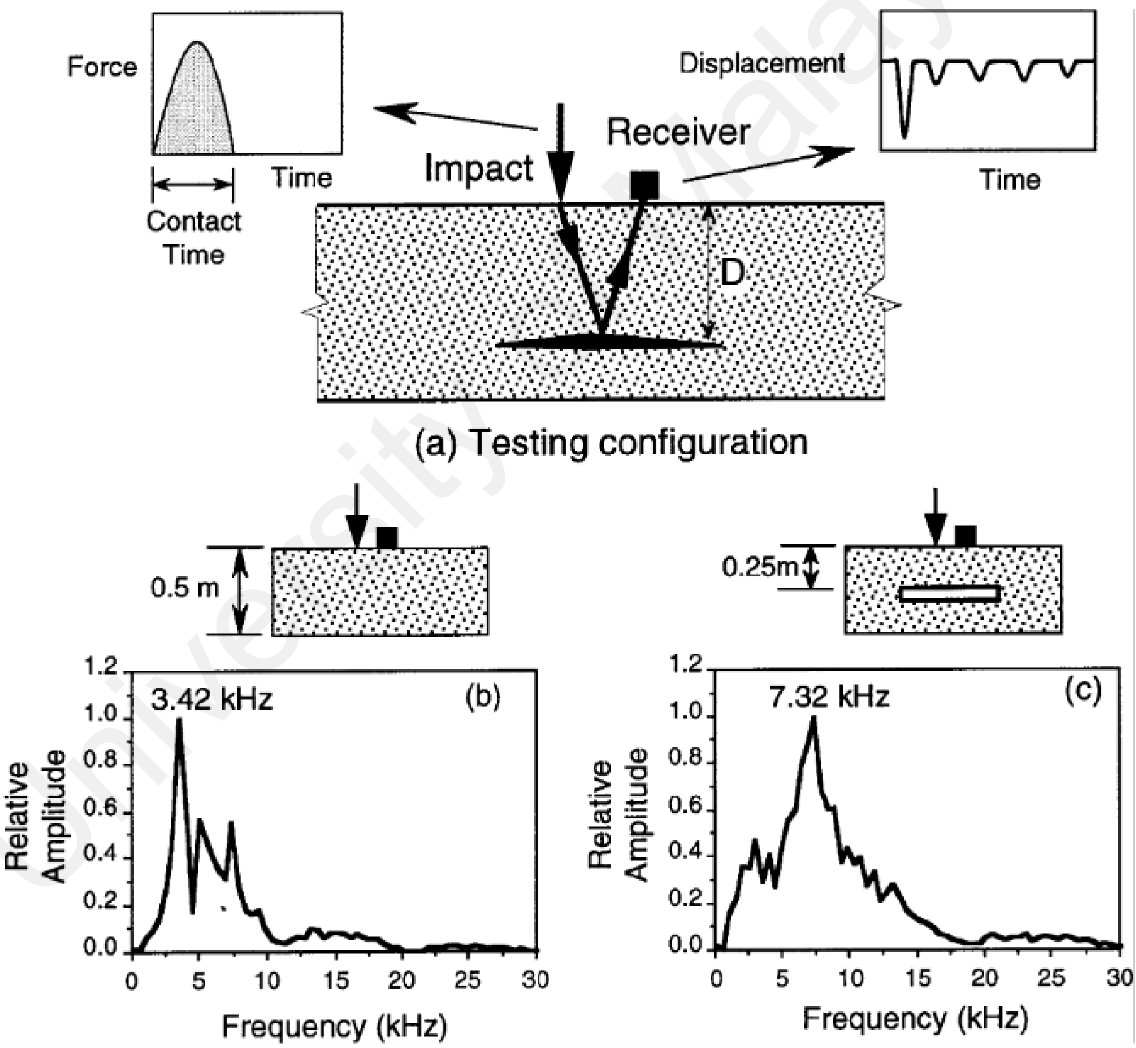

Figure 2.7: (a) Schematic of impact-echo method; (b) amplitude spectrum for the test of solid slab; and (c) amplitude spectrum for the test over void in slab (ACI Committee 228, 1998).

2.4.6.4 Spectral Analysis of Surface Waves (SASW) method

The SASW was developed initially for geotechnical applications at the University of Texas at Austin in 1980s. This method utilizes the propagation R-waves along the surface to determine the thickness, elasticity and stiffness of pavement slabs and of the underlying layers (Jones, 1955; Jones, 1962). The frequency of the waveform can be verified by determining the relationship between wavelength and wave speed of the waveform. Thus, subsurface materials can be evaluated without direct access. The SASW method has been used successfully to determine the stiffness profiles of soil sites, asphalt and concrete pavement systems as well as concrete structural members.

The phase velocities are determined as follows:

$$c_{R(f)} = X\frac{360}{\emptyset_f}f \qquad \text{Equation 2.9}$$

Where

$c_{R(f)}$ = surface wave speed of the component with frequency f,

X = distance between receivers (see Figure 2.8), and

$\emptyset_f$ = phase angle of the component with frequency f.

The wavelength, λ_f corresponding to a component frequency, is calculated using the following equation:

$$\lambda_f = X\frac{360}{\emptyset_f} \qquad \text{Equation 2.10}$$

By repeating the calculations in Equation 2.9and 2.10 for each component frequency, a plot of phase velocity versus wavelength is obtained. A surface wave is generated on the structure using an impact source in SASW analysis, as illustrated in Figure 2.8. The surface wave motion is then measured by two transducers with a certain distance away from the source. The signals measured at each transducer are then analysed and phase velocity is calculated according to the phase difference between signals from the two transducers. The elastic profile for the structure can be estimated from this obtained dispersion curve, which plots R-wave phase velocity versus frequency. However, the SASW method cannot separate different modes of propagation over a layered system since only two receivers are used in the SASW test and therefore measures a superposition of all propagating waves at the specific receiver locations. Furthermore, the complicated signal processing and inversion procedural limit further application to concrete defect detection.

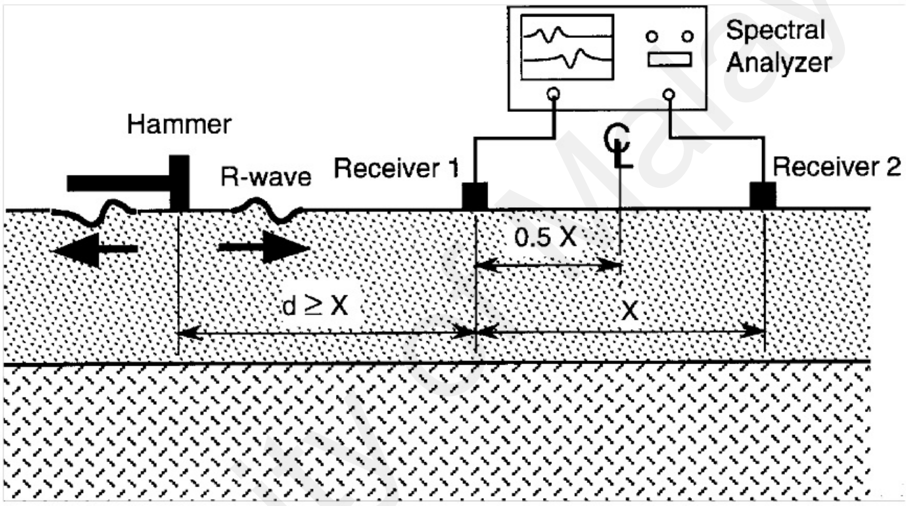

Figure 2.8: Schematic of SASW test (ACI Committee 228, 1998).

2.4.6.5 Impulse Response method

An impulse response method was developed from the vibration method for pile integrity testing (Davis & Dunn, 1974). For the last 25 years, this method has been known variably as the TDR, mobility or impedance method. The impulse response method is useful for detecting voids under concrete and reinforced concrete slabs laid on the ground, detecting the lack of interfacial cohesion (delamination) in multilayer systems, locating defective areas and inhomogeneity (honeycomb) in concrete elements and checking the length and continuity of the piles. The measuring set of impulse response method includes a hammer, a geophone and an amplifier with a laptop which illustrated in Figure 2.9.

Figure 2.9: Impulse response test kit (Hola & Schabowicz, 2010).

In the impulse response method, an elastic wave is induced in the tested element by striking its surface with the calibrated rubber-ended hammer in previously selected measuring points (Davis and Hertlein, 1987; Davis, 2003). The signal of the elastic wave propagating in the element is registered with the geophone and simultaneously amplified by the amplifier with a maximum frequency of 1000 Hz. The registered signals are processed by dedicated software installed on the laptop being part of the measurement set. This method can be readily used to test large concrete and reinforced concrete slabs. However, an impulse response examination cannot be used alone to evaluate a structure and shall always be supplemented and calibrated with other examinations. The sonic echo method is always calibrated with impulse response method (SE/IR system) to determine the length and integrity of deep foundations. Besides that, the SE/IR system also capable to test for cracks, voids, soil intrusions, uncured or weak concrete, diameter changes (bulb or neck), and deep foundation depths (ACI Committee 228, 1998).

2.4.6.6 Acoustic Emission

AE refers to the generation of transient elastic waves produced by a sudden redistribution of stress in the material. When external forces acted on a structure (change in pressure, load or temperature) and trigger the release of energy in the stress wave form to propagate to the surface and recorded by the sensors. AE signals are able to provide valuable information on the origin and importance of a discontinuity in a material (citation). Therefore, AE is widely used to assess structural integrity, detect flaws, test for leaks, or monitor weld quality.

By conducting AE tests on concrete structure, it provides results for better understanding of concrete material under various loadings like flexural loading, cyclic loading, impact loading, freezing-thawing loading, and fatigue effect and even under chemical influence like corrosion (Morton and Harrington et al., 1973; Pollock 1989; Berkovits and Fang, 1995; Labuz and Cattaneo et al. , 2001). AE parameters have been applied in several cases such as the drying shrinkage cracking of fresh concrete (Shiotani et al., 2003) and classify the types of cracking (Farid Uddin, Numata et al., 2004; Grosse and Finck, 2006;Ohno and Ohtsu, 2010). AE had been combined with other NDE techniques to evaluate damage such as bending test (Schechinger and Vogel, 2007; Wu et al., 2000; Chen and Liu, 2004; Kurz et al., 2006), pull-out tests (Grosse et al., 1997) and splitting tests (Grosse and Finck, 2006). Specific AE indexes have been used to identify the moment of critical failures (Shiotani et al., 1994; Colombo et al., 2005) much earlier than visual observation or drop of mechanical load readings. Therefore, AE is employed in the monitoring of large structures like bridges (Ohtsu et al., 2002), railway concrete piers (Shiotani et al., 2004; Shiotani et al., 2005), dams (Shiotani and Aggelis, 2007) and land slide monitoring (Shiotani et al., 2001).

2.4.6.7 Stress Wave Tomographic Technique

Owing to rapid advances in computer and electronic engineering technology, tomography technique is becoming a popular non-destructive method for assessing concrete structures (Chai et.al, 2010). Tomography means section and graphic and it is commonly applied in many areas such as medicine, biology, material science and geology. Tomography shows the particular objects' internal structure by obtaining a cross-section of an object. For example, in the medical field X-ray has been used as a tool to identify bone structures. But the concept of X-ray is by determining the ability of X-ray to penetrate the bone structure while in this study analyses its wave propagation. Elastic wave tomography employs an elastic wave to determine the size and location of defects such as crack, inclusions, air voids and other objects which may be empty or filled with a liquid or material differing in its density and physical-mechanical properties (Schabowicz K., 2014). The tomographic technique produces tomograms of the member and results should be easily understood by the engineers and the owner of the structure. There are several stress wave tomographic reconstruction techniques and each technique has its own parameter based on one of the stress wave physical properties. For example, TTT utilizes travel time of stress wave as its main parameter, the attenuation tomographic reconstruction technique is based on the amplitude of the stress wave while frequency shift tomographic reconstruction technique used the frequency. Some imminent issues of stress wave tomography technique have been studied by D.G. Aggelis concluded that higher frequency produces higher quality tomograms and element size of tomogram should less than the receivers separation distance to overcome the reduced capacity of lower frequency (Aggelis et al., 2010). In this studied, the intension is to develop four tomography algorithms named travel time technique, amplitude technique, frequency technique and Q-value technique that based on several of stress wave parameters.

2.4.6.7(a) Travel Time Parameter of Stress Wave

The TTT is a type of transmission tomography technique that employs elastic waves to propagate on the target structure medium from one source to multiple receivers. The inversion of travel time data enables tomographic imaging of the velocity distribution within the sampled structure. It is known that elastic waves propagate at varying velocities in different materials depends on its physical properties such as elastic modulus and acoustic impedance of laying materials. This is because when there is heterogeneity in a medium or existence of voids, the elastic waves will experience scattering, reflection and diffraction; in such a loss of energy the properties of waves such as frequencies and amplitude may change (Momoki et al., 2013). This method allows better identification of anomalous regions by performing an inversion of boundary measurements to determine the physical properties within the body of a structure. The testing structure is divided into square cells show that the properties of the testing medium can be quantified then quantify. Scientists suggest that the higher the number of the resolution and the better of the accuracy. The visualization of tomogram should be highly presentable and easy to be understood not only by NDT engineers but also by people without the relevant technical background, such as owners of structures.

2.4.6.7(b) Amplitude Parameter of Stress Wave

The studied show that attenuation is important for the characterization of rock and fluid properties, e.g., saturation, porosity, permeability, and viscosity, because attenuation is more sensitive than velocity to some of these properties (Best et al., 1994). The application of attenuation tomography reconstruction technique was aim to get a better visualization of tomography. AT is a generalized, model-based method for estimating and compensating for anomalous amplitude decay caused by loss of intensity or energy of the wave when it propagates in a testing medium. AT technique used attenuation coefficient as parameter to determine rate of wave energy that was attenuated and scattered when it passes through the medium. Therefore, the higher the attenuation coefficient of the medium indicates the weakened is the testing medium.

2.4.6.7(c) Frequency Parameter of Stress Wave

The frequency shift tomography examined the difference of source frequency and destination frequency of waves which due to object inhomogeneity was examined and used as tomography input. Although the frequency shift method appears to be more robust than the amplitude decay method, data interpretation involves an indirect, slightly more complicated approach. The linear system is introduced to the process of wave propagation for the purpose of estimating attenuation. With the $S(f)$ as the incident wave and instrument/medium response is $G(f)H(f)$, then the received amplitude spectrum(f). In general, it expressed as Figure 2.10.

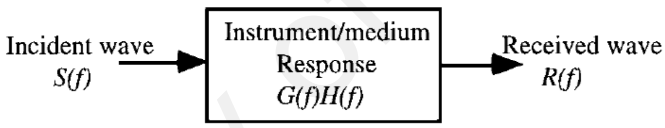

Figure 2.10: Linear system model for attenuation.

$R(f) = G(f)H(f)S(f)$ Equation 2.10

Where

$S(f)$= the incident wave;

$G(f)H(f)$ = the incident wave and instrument/medium response;

$R(f)$= the received amplitude spectrum .

Factor $G(f)$ includes geometrical spreading, instrument response, source/receiver coupling, radiation patterns, and reflection/transmission coefficients, and the phase accumulation caused by propagation, and $H(f)$ describes the attenuation effect on the amplitude. The aim of the attenuation reconstruction technique is to focus on the absorption property of the medium; therefore *H(f)* terms attenuation filter. Studied indicate that attenuation is usually proportional to frequency, that is, response *H(f)* may expressed (Ward and Toksoz, 1971) as

$H(f) = \exp(-f\int_{ray} \alpha_0\ dl)$, Equation 2.11

The attenuation reconstruction technique is used to estimate the medium response $H(f)$or more specifically α_0 , from knowledge of the input spectrum *S(f)* and the output spectrum *R(f).* A direct approach is to solve Equation 2.11 by taking the logarithm and obtaining

$\int_{ray} \alpha_0\ dl = \frac{1}{f} in[\frac{GS(f)}{R(f)}]$ Equation 2.12

The above equation is used to estimate the integrated attenuation at each frequency and is called the amplitude decay method. However, as known that the factor *G(f)* lumps many complicated processes together, and is very difficult to determine.

Furthermore, the calculation is not robust because of poor individual signal-to-noise. To overcome these difficulties, the equation can be rewrite in

$Y(f) = Cf + B$ Equation 2.13

Where *Y(f) is ln[S(f)/ R(f)], C=* $\int_{ray} \alpha_0\ dl$ and *B=-ln(G).* From the Equation 2.13, it can be seen that the integrated attenuation C is the slope of the plot of *Y(f)* versus frequency f. The attenuation estimation based on Equation 2.13 uses the spectral ratio *S(f)/ R(f),* over a range of frequencies, and is called the spectral ratio method. This method may remove the effect of factor *G,* when *G* does not depend on frequency, *f.*

2.4.6.7(d) Medium Quality Factor (Q-value)

Medium's quality factor is a seismic characteristic of attenuation property of a medium (Vladimir Sabinin, 2013). By using the Q-value, one may estimate the quality of the medium and reconstruct the tomogram of testing medium. Medium's quality factor is an alternative approach to plot tomogram. Principally, the lower the Q-value of the medium indicates the weakened is the testing medium.

2.5 Summary

There are many nondestructive techniques for concrete structures which depend on theoretical principle to produce different sets of result and information about the physical properties of the structure (Khan, M. F. H., 2015). Parallel-seismic and sonic-echo method capable to determine deep foundation depth while GPR capable to determine thickness, delamination and voids. Elastic wave-echo is a suitable method if sensor only possible to be attach on one surface while impact-echo method is similar to elastic wave-echo but for impact-echo is providing a stress pulse with greater penetration ability. Impulse response technique is used to detect cohesion such as delamination and inhomogeneity such as honeycomb in concrete. AE is useful to detect flaws and monitor weld quality. IRT is one a technique to convert thermal image into a tomogram in order for engineer to visualize the interior of structure but the accuracy can be affect by weather and surface condition.

In this research, the aim is to develop program algorithms of four stress wave tomography technique, namely TTT, AT, FT and Q-value tomography. Past research found that the acoustic impedance of material can influence the velocity of transmitted wave therefore the acoustic impedance of duct has to be taken into if account if the filling condition of the duct is to be assessed in a reliable way. This research would like to explore the possibility of attenuation as alternative parameter to plot tomography instead of velocity parameter of TTT. This is because attenuation is vital for characterizing properties of rock and fluid and represented by the decay of energy as it propagates through a material (Chai et al., 2011). Attenuation parameter could be more sensitive than velocity parameter due to some of the material condition properties, such as saturation, porosity, permeability and viscosity. Attenuation of waves, which is represented by the decrease in wave amplitude due to reduced propagation energy, is usually caused by both intrinsic properties of material and geometrical spreading.

CHAPTER 3

METHODOLOGY

3.1 Chapter Overview

The following chapter describes the methods used in this research. Four types of tomography were developed based on stress wave parameters. The developed algorithms were verified with various numerical simulation models and specimens. The developed algorithms of tomography were used to detect and visualize defects such as honeycomb, deteriorated surface and incompletely-grouted prestressed concrete (PC) model. The tomography was demonstrate on honeycomb concrete and partially grouted PC because these defects are commonly flaw found on concrete structures. On the last part of this chapter, the instrumentation and calibration of devices used for the research were being described.

3.2 Development of Algorithm

In this study, a computer algorithm was developed to process large amount of elastic wave data for the purpose of tomography reconstruction. Figure 3.1 shows the standard procedures of programme algorithm. The aim was to plot each element of a discretized area of measurement with a specific elastic wave parameter, such as computed velocity, which magnitude would change according to local variation of concrete acoustic properties. To plot a precise tomogram for each element of a discretized cell, it is necessary to assign nodes and define the trigger and receiving points in the model representing the measured area. This is exemplified by a four-element area with nine nodes as in Figure 3.2, in which each element is assigned a value, e.g., velocity that represents the condition of the measured area.

A tomogram is plotted based on the value of each element, indicating the soundness of the measured medium. The developments of algorithms are based on the ray-tracing approach and the SIRT. The algorithm required information such as the dimension of an object and the mesh dimension in order to distribute node and cell numbers. However, with increasing refinement of the mesh, the accuracy of the tomography can be improved. Beside velocity, the amplitude and frequency of the elastic waves are the other two parameters examined for tomography reconstruction. The essence of this approach originated from wave energy diffraction encountering abnormality within the propagated medium (Chaix et al., 2003) [18]. Therefore, these two parameters are presented in the form of an attenuation coefficient, which is related to the amount of energy being scattered and diffracted in the measured area. The developments of algorithms for these methodologies were undertaken based on ray-tracing approach and SIRT. The algorithm required information such as the dimension of an object and mesh dimension in order to distribute node and cell numbers. Besides, the user is required to insert the number of iterations because little iteration has low accuracy of the possibly path way through ray trace. However, with increase refinement of meshed, the accuracy of tomography can be improved. After the values of the mesh that obtained were falling in a range of acceptance, those values were used to plot tomogram.

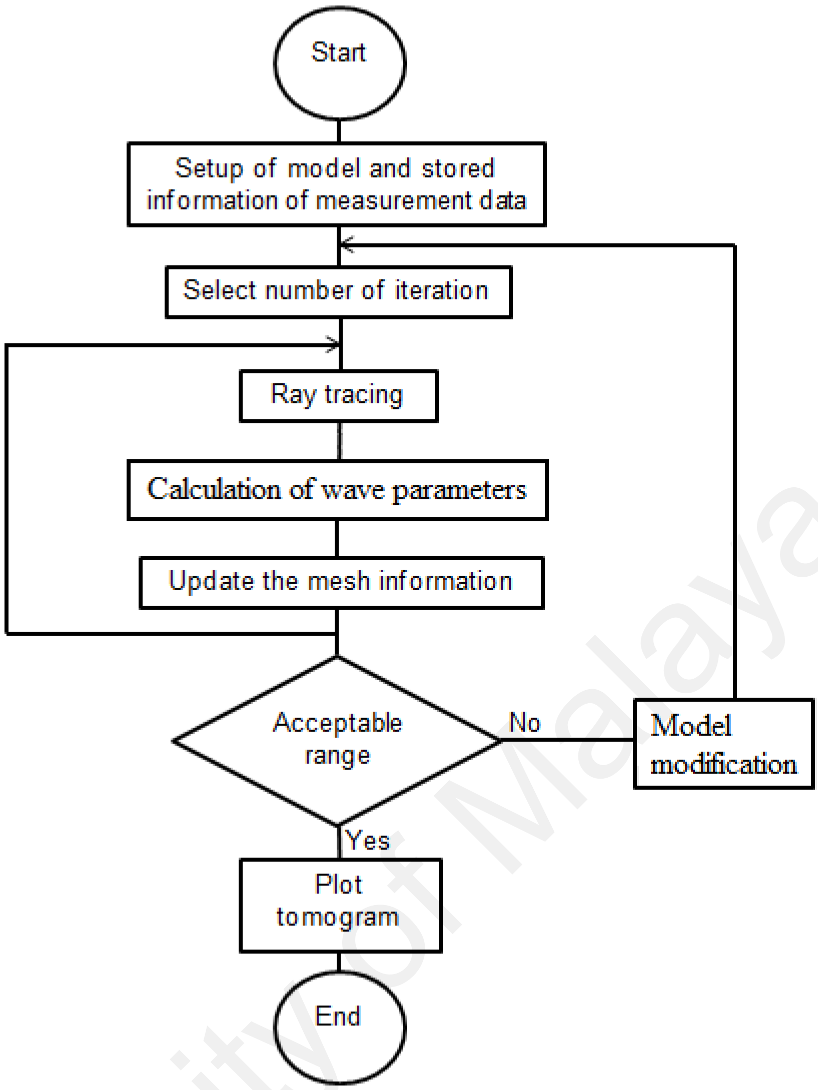

Figure 3.1: Key procedures in elastic wave tomography reconstruction.

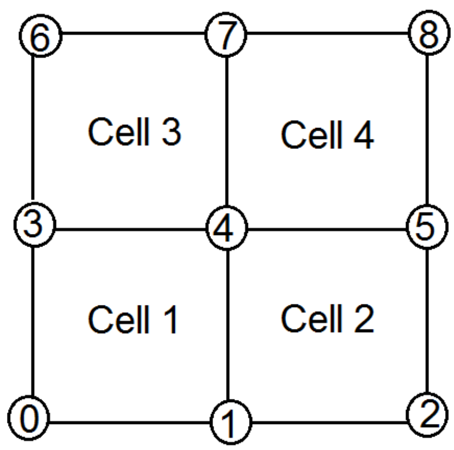

Figure 3.2: Schematic of assigned nodes and cells with number.

3.2.1 Ray tracing

Ray tracing turns out to be a powerful technique for predicting the possible travel path of elastic waves in a medium so that accurate information about any change in the wave propagation behavior can be accurately quantified. The technique relies on analysis of various mechanical and elastic properties of regions and interfaces the wave is passing through to construct a ray-path (Nowers et al., 2014). In a conventional ray-tracing algorithm, the wave velocity distribution is reconstructed by minimizing the differences in the observed and theoretical travel times. Therefore, based on this principle, the proposed algorithm in this study determines and updates the wave propagation path in an iterative computational method. This allows identification of the wave travel path and its length, which is often found to be in a non-linear trend due to the inhomogeneity introduced by defect or anomaly in a medium. With the incorporation of the ray-tracing principle, the developed algorithm is capable of determining the interceptions between element boundaries for each possible ray path.

To describe ray-tracing, an example of a four-cell medium is shown in Figure 3.3. At least seven prospective travel paths for wave propagation from node "a" to node "b" can be identified. The path that gives the shortest travel time is selected as the designated travel path for wave propagation. After travel path selection, the tomography reconstruction process is initiated. This is a process whereby the information of all elements in a meshed model is updated by minimizing the difference between observed and theoretical values (Kobayashi Y., 2013). The process continues in an iterative manner in order to obtain the best possible wave path that could provide accurate information for tomography reconstruction within the acceptable error range. The visualization of tomography can be improved if wave information covers the whole testing area (Tronicke et al.,2001; Osawa et al., 2014). Besides, the study shows that the combination of direct, reflected and heat wave for tomography reconstruction could yield a better visualisation (Tonn , 1991).

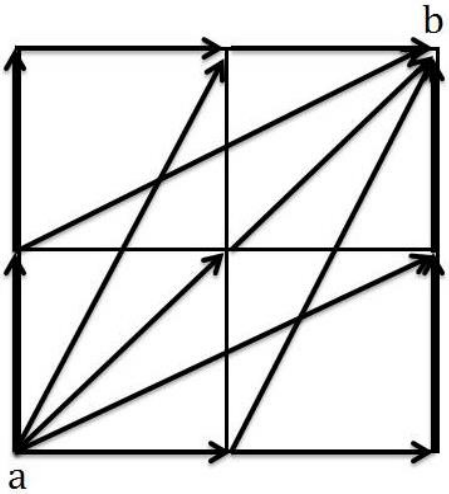

Figure 3.3: Illustration of possible pathway for wave propagates from node “a” to “b”.

3.2.2 Simultaneous Iterative Reconstruction Technique (SIRT)

SIRT is a technique for tomography reconstruction process based on least square principle. SIRT is insensitive to the errors of measurement data so it is capable to provide quality images (Su et al., 2000). SIRT distributed the different value in measurement value and estimated value into the mesh. SIRT was used for large amount of linear equations inversion and problem solving based on the least square method. SIRT combined information of error from all ray paths and then distributed based on weighting system. Therefore, the new value can be obtained and used as data for plotting tomography.

3.2.3 Travel time Tomography

TTT employs the principles of arrival time difference for elastic waves propagating from one source to multiple receiving points in the medium. The inversion of travel time data enabled tomographic imaging of the velocity distribution within the sampled structure. Due to the heterogeneity of the medium or voids existence, elastic waves scattered, reflected and diffracted, causes frequency and amplitude of the waves to change (Momoki et al., 2013). Thus, the waves propagate at varying velocities depend on the physical properties of the medium, such as elastic modulus and acoustic impedance of laying materials. The elastic waves scattered, reflected and diffracted due to medium heterogeneity or voids existence. The properties of waves, such as frequency and amplitude may change due to the loss of energy (Momokiet al., 2013). It allows better identification of anomalous regions by performing boundary measurements inversion to determine the physical properties of a structure. The following section described the inversion of travel-time data which has been practiced in this study.

Based on the ray theory, the travel time t, for the wave to travel from source sensor to destination sensor was given by (Aggeliset al., 2011):

Travel time, $t = \int_A^B 1/v \, dl = \int_A^B s \, dl$ Equation 3.1

Where, v is velocity, s is the wave slowness (also known as reciprocal of velocity) and dl is the element length. The square structure was divided into two cells as show in Figure 3.4. The ray path of source at cell "0" was l_0 and slowness of cell "0"was S_0. The difference between the observed travel time and expected travel time for source "0" was

ΔT =T(observe)-T(theory) . Equation 3.2

The differences in slowness in cell "0" that has to be updated was

$\Delta S_0 = \frac{\Delta T_0}{\mathrm{L}}$. Equation 3.3

In which L is the ray path of wave in the object.

While if there are more than one ray path information, the Equation 3.3 have to be changed into, change of slowness in the cell number "j" is defined as

$\Delta S_j = \frac{\sum \frac{\Delta T_i}{L_i} \mathrm{x}\, l_j}{\sum l_j}$ Equation 3.4

Where i represented source and j represented the numbers of cell.Therefore, the updated of slowness for cell "j" was

$S_j = S_j$(inputted slowness)+ ΔS_j . Equation 3.5

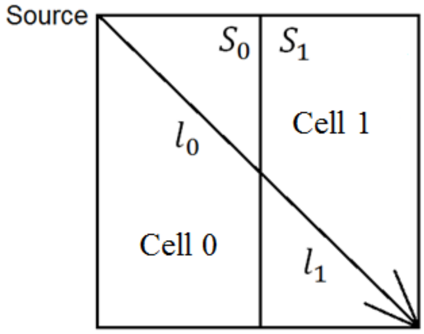

Figure 3.4: Schematic of wave propagates through two elements, from top left to bottom right.

3.2.4 Amplitude Technique

The amplitude technique (AT) technique is similar to the travel time reconstruction. However, the AT technique is determined by the inelastic property of the medium while TTT was determined by the elastic properties and the structure density (Liu L. and Guo T, 2005). A study has shown that the attenuation is important for the characterization of rock and fluid properties such as saturation, porosity, permeability, and viscosity as it is more sensitive than velocity to some of these properties (Best et al., 1994).

The first arrival wave peak amplitude at destination sensor is defined as

$A_i = A_o e^{-\alpha l}$ Equation 3.6

Where, A_i is the amplitude of the wave of the R *(f)*,A_o is the amplitude of the wave of S *(f)*, α is the attenuation coefficient of elements and ∫ is element length.

The attenuation coefficient, α was used to indicate the penetration of the wave and its speed when passed through a medium. Therefore, the higher the attenuation coefficient of the medium, the weaker is the medium. The attenuation of waves was represented by the decrease in wave amplitude due to reduced propagation energy. A study has shown that the reduction in propagation energy was caused by the intrinsic properties of the material and the geometrical spreading (Chai et.al. 2011). The AT technique was used to observe the energy of the elastic wave that was scattered and absorbed when it travelled through a medium. The existence of a void and defect were detected when the arriving wave energy was irregular, large and abnormal. The ray-tracing method of the TTT has been used in AT to determine the wave ray-path. The first receiving offset amplitude from source wave propagations was computed with Equation 3.6. Due to the void or defect, there was a difference in attenuation coefficient value where updates were needed. Thus, the Equation 3.6 becomes:

$A_r = A_o e^{-(\alpha + \Delta\alpha)l}$ Equation 3.7

By assuming the case as shown in Figure 3.4, the change of attenuation coefficient for cell 0 was calculated as

$\Delta\alpha_0 = \frac{[\ln\left(\frac{A_r}{A_o}\right) + \sum \alpha l]}{L}$ Equation 3.8

When are more than one ray path information, the Equation 3.8 has to be changed into the change of slowness at cell number "j" is defined as

$\Delta\alpha_j = \frac{\sum \left(\frac{-ln\left(\frac{A_r}{A_o}\right)_i - \sum \alpha l_i}{L_i}\right) x\ l_{ij}}{\sum l_{ij}}$ Equation 3.9

Where i represented sources and j represented as number of cells.Therefore, the updated of attenuation coefficient for cell "j" was

$\alpha_j = \alpha_j$ (inputted) + $\Delta\ \alpha_j$. Equation 3.10

3.2.5 Frequency Technique

The FT is based on computing the frequency variation of waves as they propagate in a medium from a source to a destination. Although the frequency technique is more robust than the amplitude decay method, the data interpretation involved an indirect and slightly more complicated approach. FT is believed to be more suitable than TTT as central frequency is more sensitive than pulse velocity, especially on the early stage of repair because of fresh cement (Aggelis et al. , 2011). The attenuation coefficient of material times with the length of ray path of wave can be computed as (Quan, Y. and Harris J. M. (1997)

$$\int_{ray} \alpha_0 \, dl = (f_S - f_R)/\sigma_S^2 \,, \qquad \text{Equation 3.11}$$

From Equation 3.11, The intrinsic attenuation coefficient, α_o, can be estimated based on centroid downshift of frequencies of input spectrum *S(f)* and the output spectrum *R(f)*as described in Equation 2.10. Due to the void or defect, there were differences in attenuation coefficient value so the Equation 3.11 becomes:

$$(\alpha + \Delta\alpha)l = \frac{(f_S - f_R)}{\sigma_S^2} \qquad \text{Equation 3.12}$$

By assuming the case as shown in Figure 3.4, the change of attenuation coefficient for cell 0 is calculated as

$$\Delta\alpha_0 = \frac{\left[\frac{(f_S - f_R)}{\sigma_S^2} - \sum \alpha l\right]}{L} \qquad \text{Equation 3.13}$$

While if there is more than one ray path information, the Equation 3.13 have to be changed into, change of slowness in cell number “j” was defined as

$$\Delta\alpha_j = \frac{\sum \left(\frac{\frac{(f_S - f_R)}{\sigma_S^2}_i - \sum \alpha l_i}{L_i} \right) x \, l_{ij}}{\sum l_{ij}} \qquad \text{Equation 3.14}$$

Where i represented sources and j represented the number of cells.Therefore, the updated attenuation coefficient for cell “J” was calculated by using Equation 3.10.

3.2.6 Medium Quality Factor (Q-value) Technique

In section 3.2, it has mentioned that analyse of wave attenuation and offset time of P-wave can be used to estimate the properties of the medium. Q-value is a seismic characteristic of a medium’s attenuation property and they are useful for improving resolution (Vladimir S., 2013). By using the Q-value, one may estimate the quality of the medium and reconstruct the tomogram of the testing medium.Attenuation coefficient of wave amplitudes, α due to dispersion obeys a law (Tonn, 1991) is defined as:

A (t)= α_0(t) $e^{-\beta\int}$. Equation 3.15

Where β is the absorption coefficient of the medium and ∫ is the length of the ray-path.

Q-value is defined (Sheriff, 2002):

$Q=\frac{2\pi E}{\Delta E}$ Equation 3.16

Where E is peak energy and ΔE is energy to be dissipated in a cycle.

From a report that presented by Futterman, α is related as follows

$\frac{2\pi}{Q} = 1- e^{-2d}$. Equation 3.17

Where $d=\frac{\beta l}{tf}$; in which $t$is travel time and f is frequency. For large values of Q , the approximation $Q=\frac{\pi}{d}$ is valid.

So, $Q= \frac{\pi t f}{\beta l}$ and $\alpha=\frac{\beta}{f}$. Equation 3.18

By rearrangement, $\alpha=\frac{\pi t}{Ql} = \frac{\pi}{Qv}$, where v is the wave velocity.

Finally, the Q-value can be defined as

$Q=\frac{\pi}{\alpha v}$. Equation 3.19

Where values for α and v of the cell has been obtained from TTT and AT technique. So the work can be extended to obtain the Q-value for each cell of testing medium.

3.3 Verification of Algorithm

In order to make sure the developed algorithms are functioning and examine the efficacy of proposed algorithms, the algorithms were verified with various numerical simulation models and experimental specimens. Three types of tomography reconstruction algorithms were developed based on stress wave parameters. The developed algorithms were verified with various numerical simulation models and experimental specimens. Data that collected from numerical simulation models and experimental specimens were analyzed in order to obtain first arrival travel time, first peak amplitude and also central frequency and variance from the frequency domain graph.The developed algorithms of tomography were used to detect and visualize defects in the form of honeycomb and partially grouted tendon sheath in concrete block specimens. Some of significant numerical and experimental results will be presented in the Chapter 4. The summary of approach for verifications of proposed algorithms is displayed in Figure 3.5.

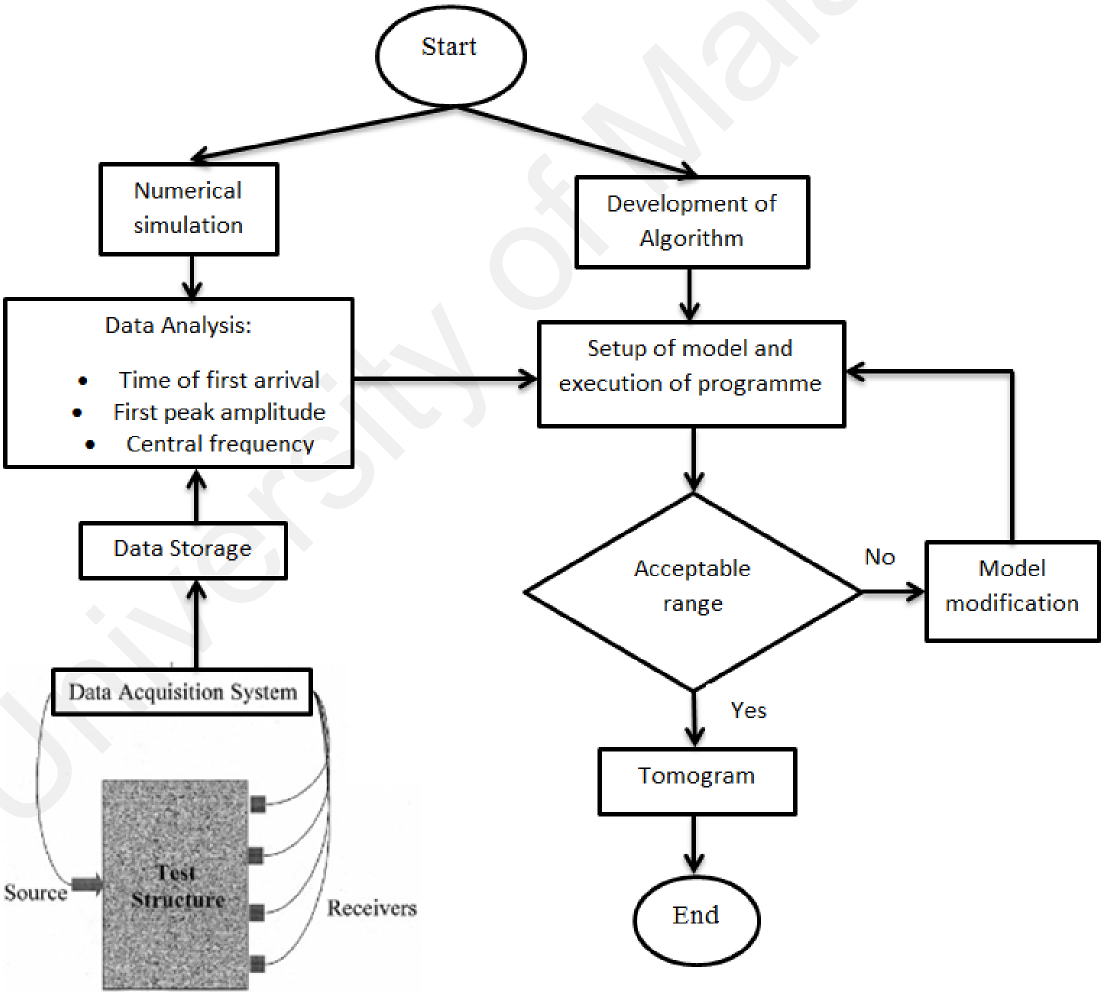

Figure 3.5: General approach for verifications of proposed algorithms.

3.3.1 Numerical Simulation

The analytical work was carried out by two-dimensional (2D) numerical simulations of wave motions. The numerical simulations were conducted with commercially available software named *Wave2000® plus* developed by *Cyber Logic*, in order to produce the raw data (time domain and frequency domain). The simulation results were further processed and the data were used as the input data for tomography reconstruction computation to generate tomograms that indicate the velocity and the attenuation coefficient distribution of the interior measured target. The fundamental equation of two-dimensional propagation of stress waves in a perfectly elastic medium, by ignoring viscous losses is as follows:

$$p\frac{\partial^2 u}{\partial t^2} = \mu\nabla^2 u + (\lambda + \mu).u \qquad \text{Equation 3.20}$$

Where $u=u(x,y,t)$ is the time-varying displacement vector, p is the material density, ϑ and μ are the first and second lame constants and t is the travel time. The software performs computation to solve the Equation 3.20 at discrete points with respect to the boundary conditions of the model, which include the input source that has predefined time-dependent displacements at a given location and a set of initial conditions. The Equation 3.15 is applicable for wave propagation to solve any heterogeneous geometry, while the continuity conditions for stress and strains must be satisfied on the interfaces. The wave speed of simulation is determined by the parameters such as p , ϑ and μ. The longitudinal wave speed, V_L in the medium is given by

$$V_{L=}\sqrt{\frac{\lambda+2\mu}{p}}. \qquad \text{Equation 3.21}$$

The relationship between Young modulus of medium with first and second lame constants, λ and μ is given by

$$E=\frac{\mu(3\vartheta+2\mu)}{\vartheta+\mu}\ . \qquad \text{Equation 3.22}$$

The source was configured as excitations by impacts (point source) which is a single cycle of Sine Gaussian pulses at 50 kHz frequency. In this case studied, the material information that had been applied is listed as below:

Table 3.1 Material properties of testing medium.

Material	Density, p (kgm^{-3})	Young modulus, E_c (GPa)	First lame constants, ϑ (GPa)	Second lame constants, μ (GPa)	Longitudinal wave speed, V_L (ms^{-1})
Concrete	2400	35.71	12.4	13	4000
Surface deterioration	2000	13.57	2.5	5	2500
Honeycomb	1600	12.78	1.6	1	1500
Aluminium	2700	69	61.38	24.95	6420
Polyethylene	920	2	2.962	0.2683	1950
Steel	7830	200	121.2	80.77	6001

3.3.2 Sensors Arrangement

Figure 3.6 shows the schematic diagrams of the sensor arrangement and imaginary wave network. Twenty 10 mm sensors were located as shown in Figure 3.6(a). The distance between two sensors was 88 mm. The source was configured at the side of source sensor by impact (point source) to generate a single cycle of Sine Gaussian pulses at 25 kHz and 50 kHz frequency. In the case of 2-side transducer coverage, when one of the sensors (labelled sensor 1) was set as the source, other sensors (labelled sensors 15 -20) were set as receivers to record the transmitted wave. The recorded wave data was then further analysed for travel time and attenuation properties computation. The ray-path coverage associated with 2-side transducer coverage was shown in Figure 3.6(b). For the case of 4-side transducer coverage (complete coverage), when one of the sensors (sensor 1) was set as trigger sensor, all other sensors at different sides to the source (sensors 7–20) would be set as receivers to record the transmitted wave. The ray-path coverage associated with 4-side transducer coverage is shown in Figure 3.6(c).

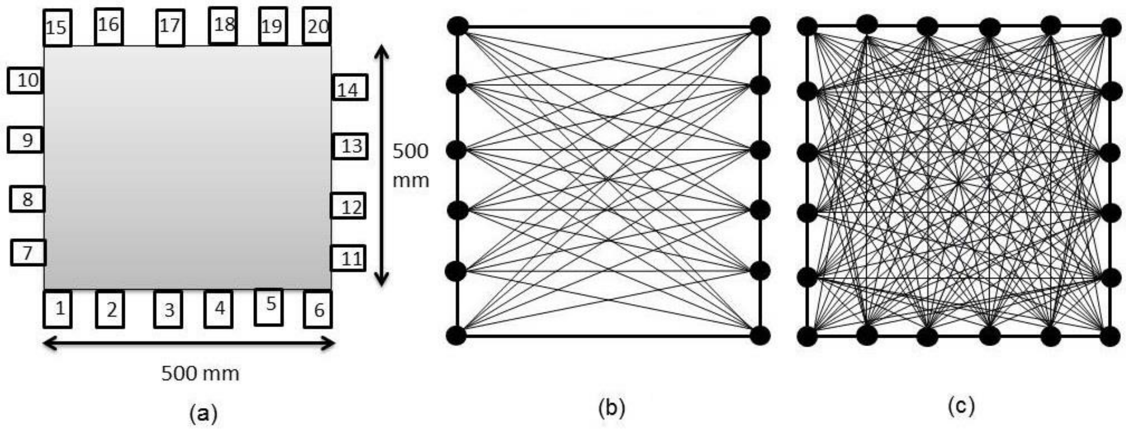

Figure 3.6: (a) Sensors arrangement on concrete model; (b) ray-path coverage for 2-sides sensors array; (c) ray-path coverage for 4-sides sensors array (complete coverage).

3.3.2.1 Concrete with Honeycomb

The first model is a 500mm x 500mm cube concrete that contain honeycomb in the centre as illustrated in Figure 3.7(b), and the other is 500mm x 500mm cube normal concrete which simulated as illustrated in Figure 3.7(a). The purpose of simulated the normal concrete is to set it as a standard to be compared with the defect concrete model.

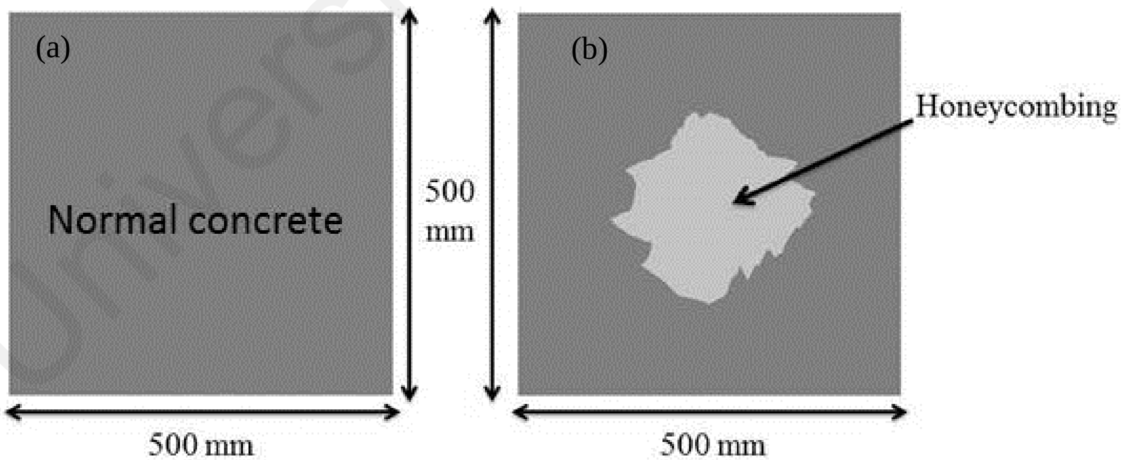

Figure 3.7: Diagrams of simulation models: (a) Normal concrete structure and (b) concrete with honeycomb.

3.3.2.2 Concrete containing Honeycomb and surface deterioration

The second model is a 500mm x 500mm concrete model with 50 mm-thick of surface deterioration at all four sides of the concrete model and honeycomb at the centre as illustrated in Figure 3.8(a) and Figure 3.8(b), respectively. The honeycomb and surface deterioration were modelled by providing lower E_c values. This resulted in lower elastic wave propagation velocities of 1500 ms^{-1} and 2500 ms^{-1} for the deteriorated area and the honeycomb, respectively.

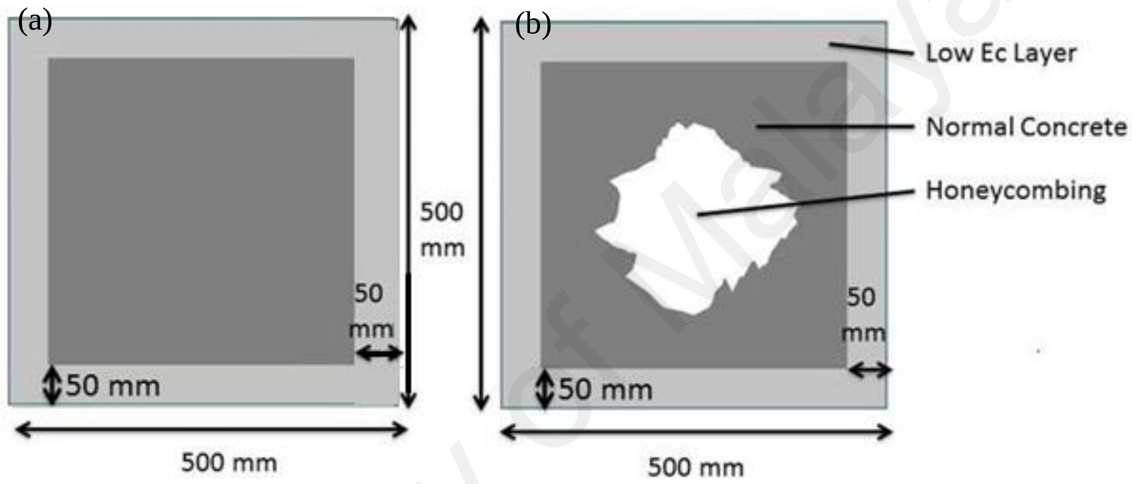

Figure 3.8: Schematic diagrams of simulation models: (a) concrete with surface deterioration and (b) concrete with honeycomb and Low Ec layer.

3.3.2.3 Concrete model with tendon duct

As part of the algorithm verification, the feasibility of using elastic wave tomography for assessing the condition of tendon duct filling in concrete was carried out. In simulation, a 500 mm square concrete with a hollow circular object of 100 mm in diameter located at the centre was modelled, which resembled a prestressed tendon duct in concrete. In the model, the thickness of “duct” was 5 mm. Two types of materials were considered for the “duct” in simulation, namely aluminum and polyethylene, which are commonly used to fabricate the duct. As shown in Figure 3.9, three types of filling conditions were examined in the simulation: 100% fully grouted), 50% and 0% (no grouting at all). The filling material considered in the simulation was defined to have similar properties with the concrete used for the mother medium.

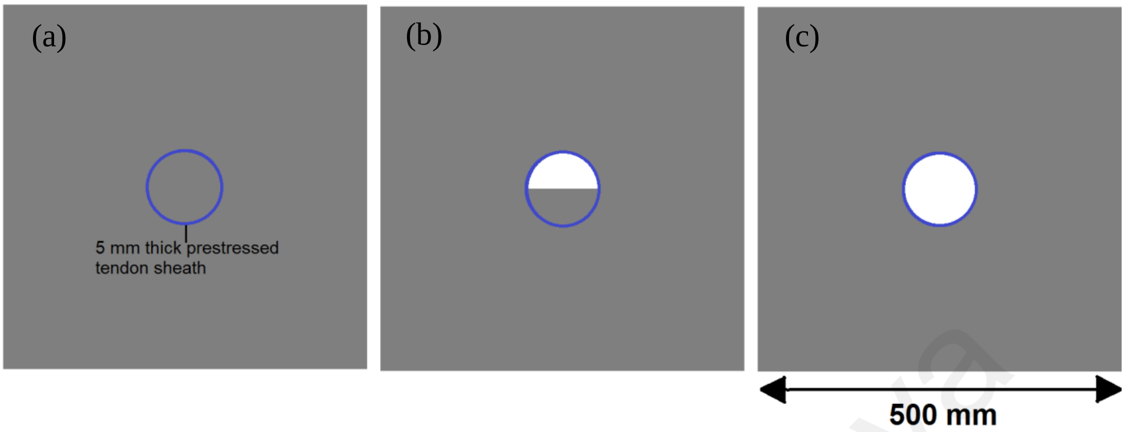

Figure 3.9: Diagrams of simulated prestressed concrete models: (a) 100% filling , (b) 50% filling and (c) 0% filling.

The second type of prestressed concrete model that had been studied is the PC with steel tendon. The conditions had been same as previous that mentioned on subtitle of 3.3.2.3 but with the additional of 50mm diameter steel tendon at the centre of tendon duct.

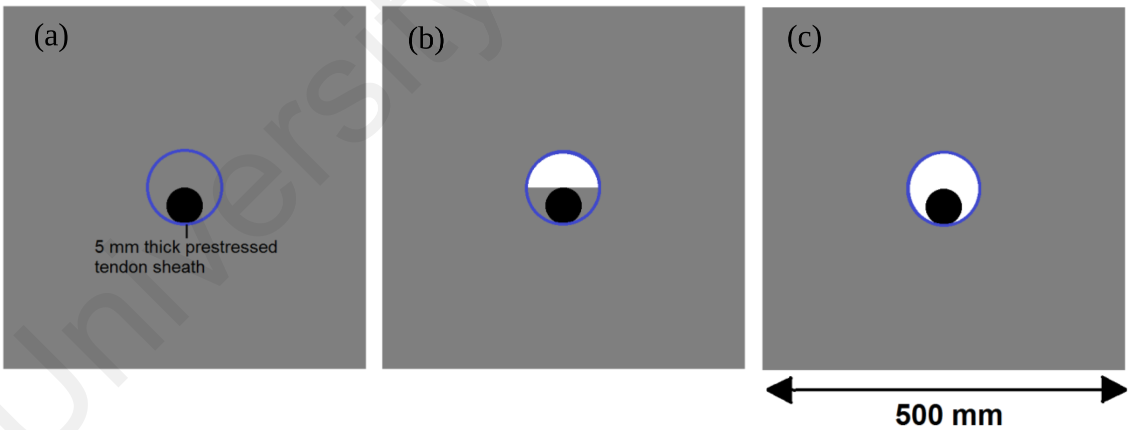

Figure 3.10: Diagrams of simulated prestressed concrete with steel tendon models: (a) 100% filling, (b) 50% filling and (c) 0% filling.

3.3.3 Laboratory Measurement

Experimental measurements were conducted using concrete specimens prepared under laboratory environment. The purpose was to further verify the usefulness of the developed algorithms as well as to establish appropriate measurement instrumentations for in-situ assessment purposes. General purpose wave acquisition system and accelerometers were used in the experimental measurement work.

3.3.3.1 Measurement of Elastic Wave Propagation

To measure the concrete quality in elastic wave speed, two sensors have to be attached on the surface of the testing medium as in Figure 3.11. In the studied by Bond L. J. et al (2008), it is possible to measure the velocity in three directions depending on the accessibility of the structure faces. In this studied, the slowness of medium is calculated based on indirect transmission EWT. The P-waves velocity of the medium was calculated by

$$\text{Slowness of medium, } s = \frac{\text{Travel time, } t}{\text{Distance, } D} \qquad \text{Equation 3.23}$$

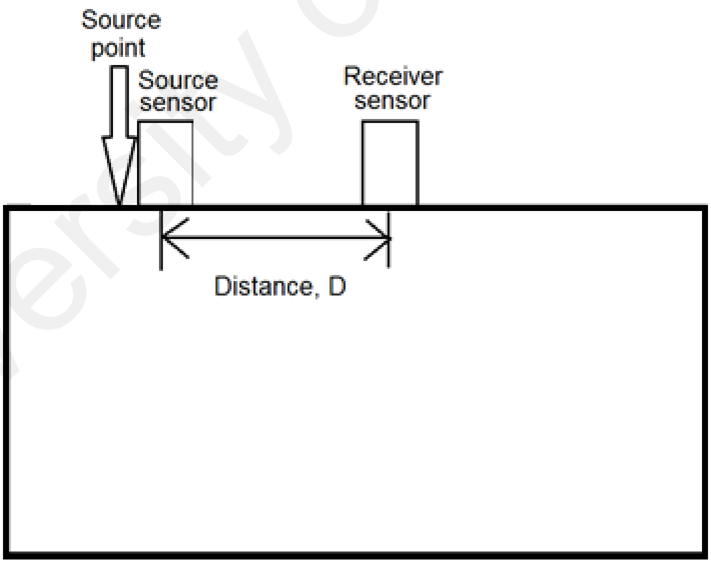

Figure 3.11: Estimate the medium's slowness by the inverse of wave velocity from a short distance of two sensors that attached on the surface of testing medium.

3.3.3.2 Concrete specimen with honeycomb

The 500 mm cubic concrete specimen was prepared with a bag of coarse aggregates being pre-inserted before casting into the centre of specimen to simulate a honeycomb. The “honeycomb” was prepared to be approximately about 200 mm in diameter, with a density of about 2000 kgm^{-3} as shown in Figure 3.12, the “honeycomb” was hung to be placed inside the mould. Grade C30 as per British Standards mix concrete was poured into the mould in three layers with each layer properly compacted. The specimen was cured by covering with wet burlap for 1 week before demoulding. Figure 3.12 shows the specimen after demoulding.

Figure 3.12: “Honeycomb” was hung in the centre of the mould.

Figure 3.13: Specimen with honeycomb after demoulding.

3.3.3.3 Concrete specimen with Tendon Duct

Another concrete specimen was prepared for testing as illustrated in Figure 3.14. Elastic wave tomography was used to measure the cross section of specimen perpendicular to longitudinal direction in order to assess the condition of grout filling inside tendon duct. . Figure 3.15 shows the side cross section profile of the specimen. Tendon duct that was selected is a corrugated aluminium tendon duct with interior diameter of 100 mm and with thickness of 9 mm. Cement grout that used to filled the tendon duct is ASTM C 476 based on Standard Specification for Grout Masonry. Figures 3.16 show the wooden mould specially prepared to accommodate the tendon duct at the centre cross section, while Figure 3.17 shows the condition after concrete casting.

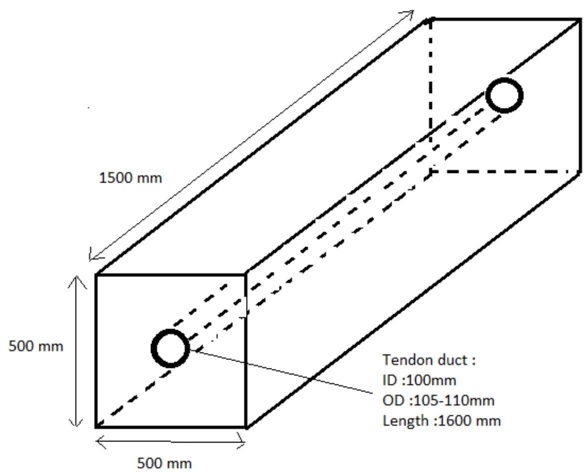

Figure 3.14: 3D illustration of specimen with tendon duct.

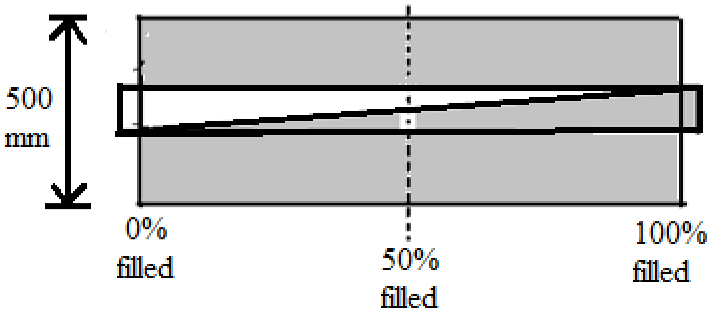

Figure 3.15 : Side cross section profile of concrete specimen showing condition of grout filling in tendon duct.

Figure 3.16: Mould of 500mm x 500mm x 1m concrete block with corrugated aluminium duct.

Figure 3.17 : 500mm x 500mm x 1m concrete specimen that with cast grout inefficiency PC Tendon duct in the centre.

In order to determine the strength of concrete, a cast concrete specimen of 100mm x 100 mm as shown in Figure 3.18(b) were tested for compressive test in accordance with BS EN 12390-3: 2002. For each test, the cubes were tested at the pace rate of 6.00 kN/sec in ELE compression testing machine of capacity 3000 kN as shown in Figure 3.18(a). The test was done at concrete ages of 1, 3,7,14 and 28-day and the test results were plotted as a graph and shown in Figure 3.19. For the concrete that casted for this PC tendon duct model, the 28 days compression strength was achieved 57.25 MPa. While the 28 days compressions test for concrete that cast for honeycomb model has achieved compression strength of 55.39 MPa.

Figure 3.18: (a) Universal testing machine; (b) Cube specimen.

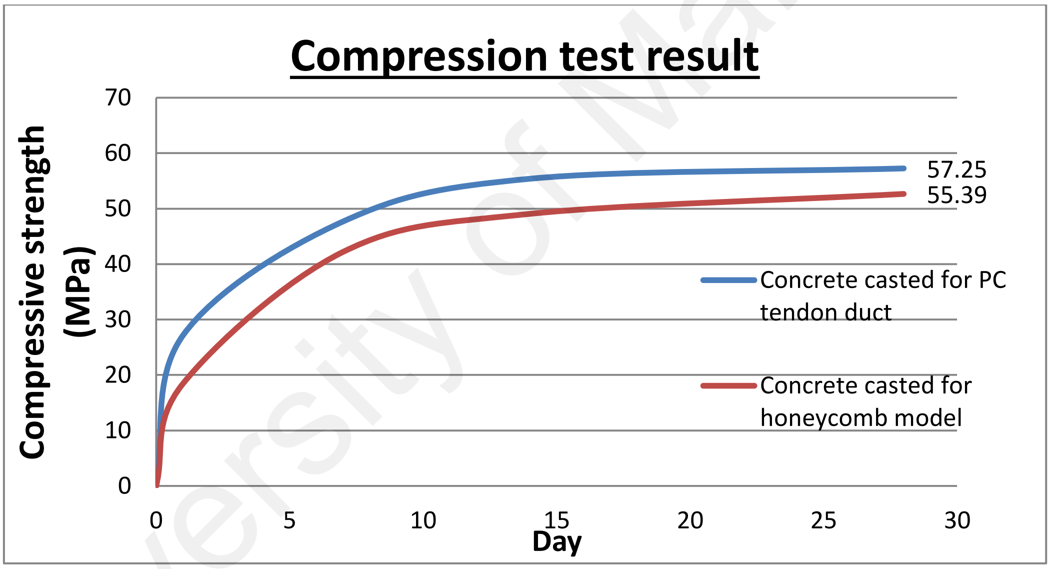

Figure 3.19: Result of cube compression test.

3.3.4 The instrumentation setup of Tomography Technique

The setup for tomography measurement is shown as Figure 3.20. The instrumentation setup for author research consists of several piezoelectric sensors, and a computer-based data acquisition device and system. Additionally, other accessories are necessary such as couplant and connecting cables. In order to generate stress wave that can be detected by piezoelectric transducer, a small steel sphere as shown in Figure 3.21 is tapping against the surface of testing concrete. A small steel sphere is typically range in between 3 mm to 15 mm in diameter. The relationships between duration of impact time, the diameter of the sphere and the kinetic energy of the sphere at impact are explained on the Hertz theory of elastic impact (Goldsmith, 1965; Sansalone, 1986; Sansalone and Carino, 1986). Table 3.2 is a central frequency obtained analysed by FFT based on ten types of steel spheres that tapped on the surface of concrete.

The piezoelectric sensor is acting as a receiver to convert detected changes in pressure, acceleration, strain or force into electric signals. . In this research, single crystal materials piezoelectric sensor as Figure 3.22 had been chosen for testing. The sensors were produced by PCB Piezotronics® and model of 352A60 with sensitivity of 9.63 mV/g and can detect frequency in the range of 5 to 60000 Hz. The couplant should feature low impedance if compared to the material under tested therefor wax were applied on the surface in between the contact of sensors and concrete. Besides that, the couplant layer was made sure to be even and smooth. In addition, the connecting cables should be chosen to eliminate electro-magnetic interference.

The first arrival travel time and first peak amplitude need to be obtained from the waveform data that collected from numerical simulation and laboratory. In order to do that, the computer programme for attracting first travel time and amplitude have been developed by using the Labview software. The screenshot of the design platform has been presented as Figure A1 and the block diagram is shown as Figure A2 at appendix part.

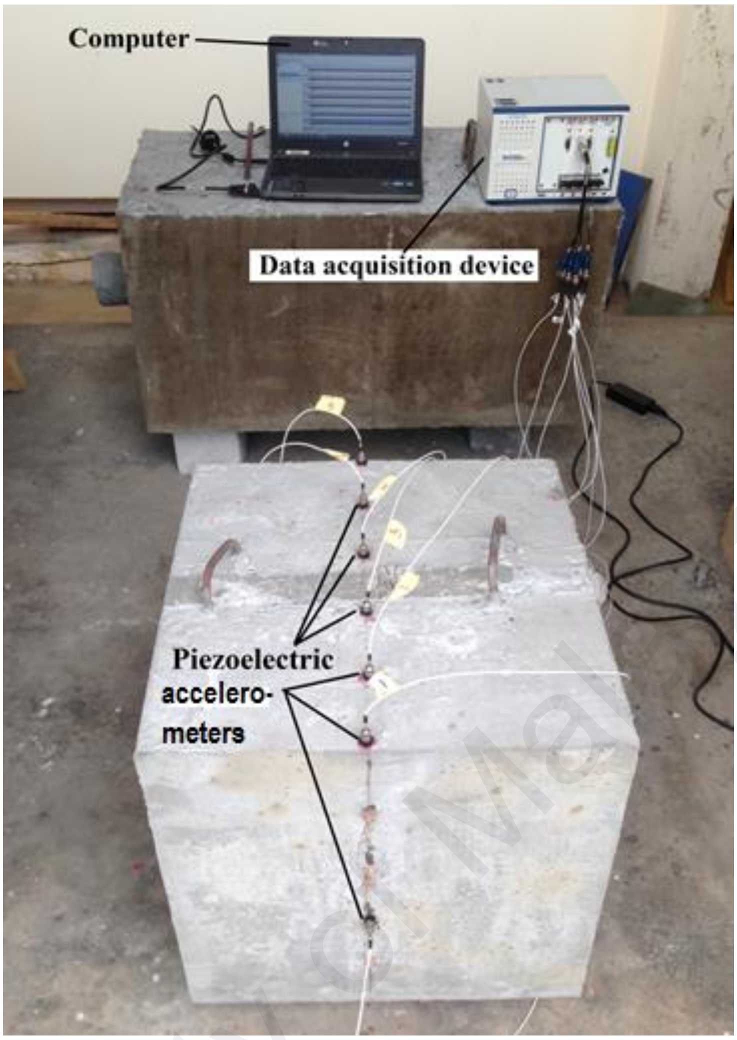

Figure 3.20: The instrumentation setup in research.

Table 3.2: Diameter of steel sphere and its central frequency obtained from the frequency domain graph.

Diameter (mm)	Centre frequency (kHz)
3	25.057
4	22.793
4.7	22.443
6.3	20.762
8	19.803
9.5	18.940
11	18.359
12	17.583
16	16.672
19	12.726

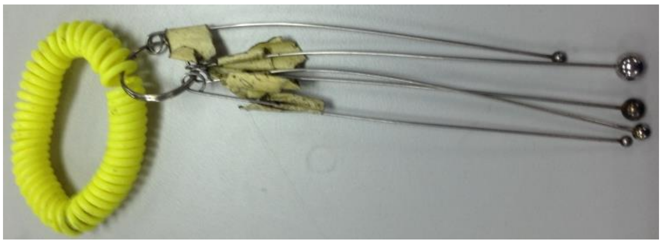

Figure 3.21: Steel sphere.

Figure 3.22: Piezoelectric sensor.

Figure 3.23: NI PXLE-1073 data acquisition device.

CHAPTER 4: RESULTS AND DISCUSSIONS

4.1 Chapter Overview

The collected data were first processed and analysed for travel time, first peak amplitude, central frequency and its variance. Numerical simulations of experimental waves were carried out to obtain data used for verifying the developed algorithms in reconstructing the elastic wave tomography. The first section of this chapter discusses findings behaviour of wave propagation in concrete with defect and describes procedures in obtaining the wave data and reconstruct tomogram. The next section discusses outcomes of numerical simulations, which include results from simulating model of concrete and that with partially grouted tendon duct to resemble prestressed concrete (PC) cross section. The source frequency of numerical simulations for concrete with honeycomb was set at 50 kHz while the source frequency of numerical simulation for concrete with tendon duct was 10 kHz. In experimental measurements, source frequencies of 18 and 25 kHz were adopted, difference of frequency ware used so that the results of tomogram consist of several of frequency source.

4.2 Wave Propagation Behaviour

Figure 4.1 displays four consecutive snapshots of simulated elastic waves propagating a concrete model with honeycomb. It could be observed that as the wave propagated from intact regions and encountered honeycomb regions, refraction, reflection and scattering of the wave took place. As a result, the energy of the wave was distorted and it propagated at a lower speed compared to propagating in homogeneous concrete as indicated in Figure 4.1(b). The delay in wave travel time became more visible as it propagated further into the honeycomb, with reflection and scattering being observed at the honeycomb-concrete interface due to the acoustic impedance difference, as seen in Figure 4.1(c). After a while, the wave arrived at the sides of the model being received by all sensors, as shown in Figure 4.1(d).

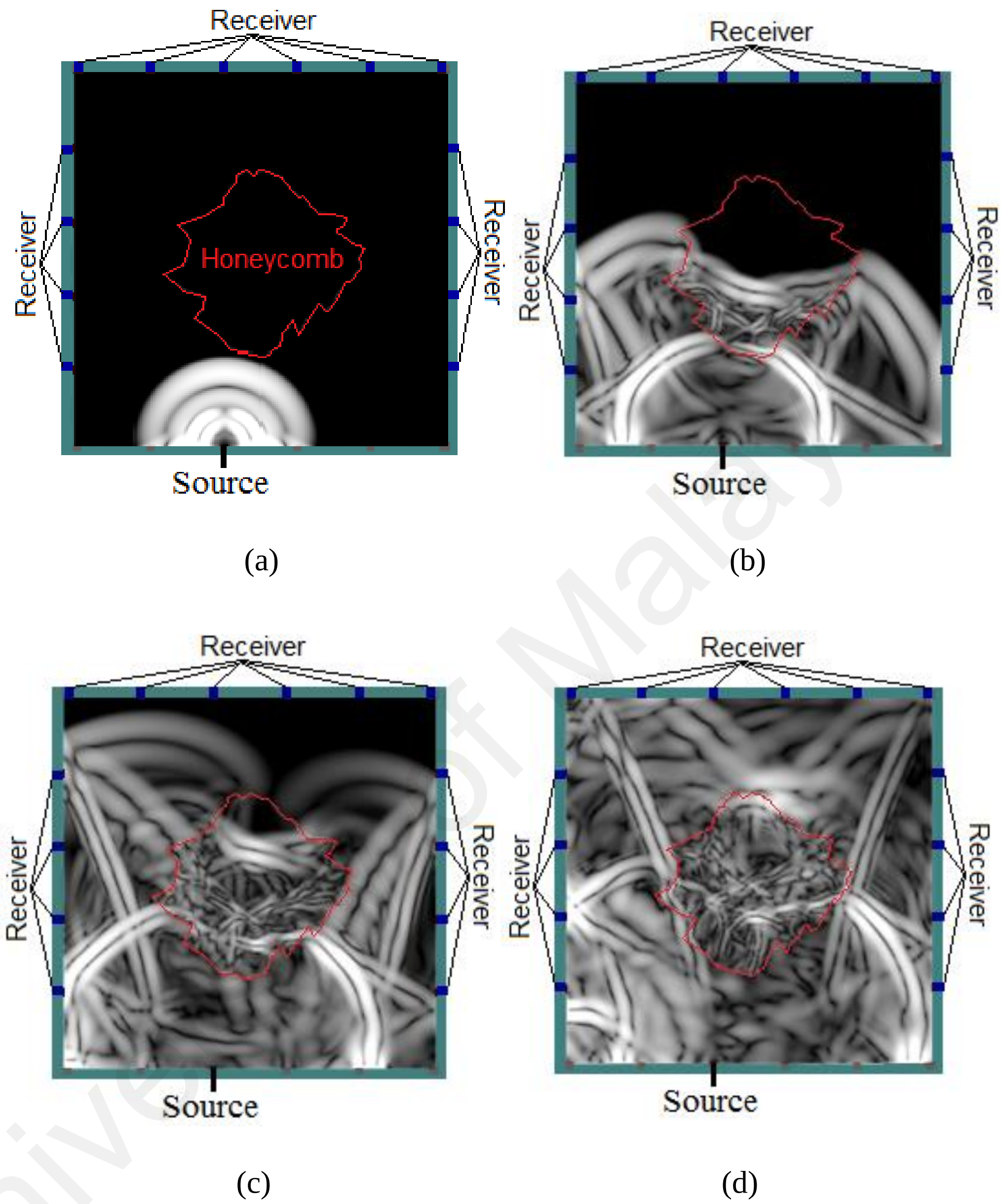

Figure 4.1: Four consecutive snapshots of the simulated transient displacement field in the model with honeycomb: (a) Wave starts to propagate from a source; (b) Wave experiences distortion by honeycomb; (c) Wave propagated faster in normal medium than in honeycomb; (d) Wave-front arrived at the side and being received.

Figure 4.2(a) is an example of time domain data for a trigger and a receiver as simulated. The time difference between excitation from trigger and wave arrival at the receiver is distinguishable. The time domain data was converted to frequency domain by fast Fourier transform (FFT), yielding the amplitude spectrum of the waves as shown in Figure 4.2(b). The centroid frequency and variance could be computed from the amplitude spectrum. It can be noticed that the central frequency at the receiver has been shifted to the left side (lower frequency) which is an implication of the occurrence of attenuation in the higher frequency components as a result of wave distortion by the honeycomb.

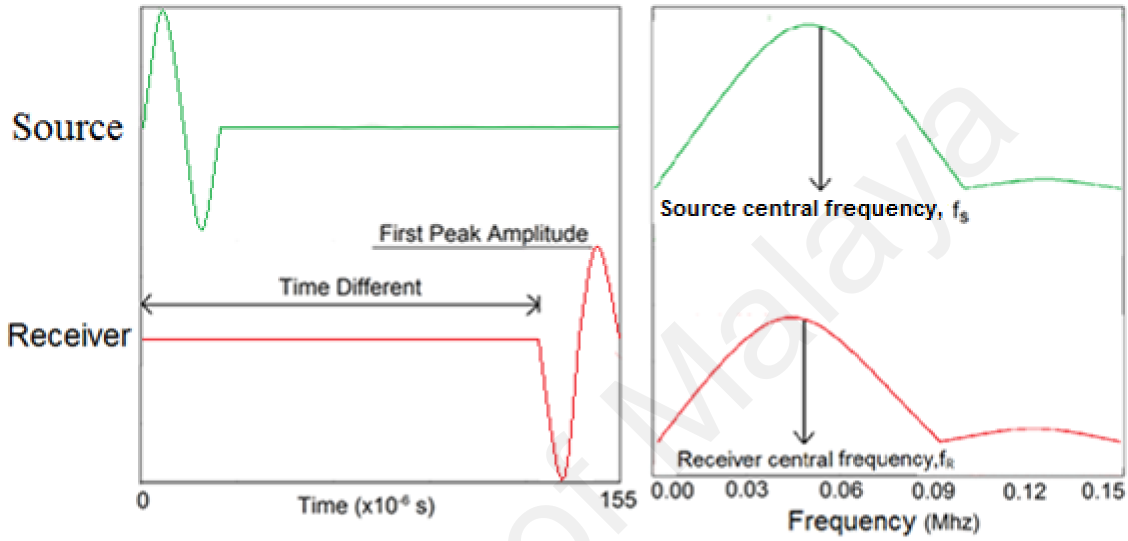

(a) (b)

Figure 4.2: Examples of elastic wave time-domain (a) and their spectral amplitude (b) for sensor at a source and a receiver.

Figure 4.3 is an example of time domain wave data of amplitude versus time of waves captured from experiment as in Figure 3.12, which propagates in two types of medium: intact concrete and concrete with honeycomb. Figure 4.3 demonstrates that waves in intact concrete reached the sensor earlier than waves that were propagated in concrete with honeycomb. It is reasonable that when the honeycomb is positioned on the straight line between the excitation and receiver location, the travel time becomes longer due to the lack of the presence of the shortest path (straight) for the wave to propagate. By referring back to Figure 4.1(a) and 4.1(b), it shows that when P-wave impinges on the boundary of the honeycomb, the wave-front is no longer uniform and the wave propagates on the surface of the honeycomb. This causes a delay in travel time from trigger point to receiver location. Therefore, an additional amount of traveling time from trigger point to receiver results in lower measured velocity for the paths including the honeycomb. Besides, Figure 4.3 shows that the amplitude of the wave propagated in concrete with honeycomb is lower than in intact concrete. The amplitude drops at receiver is due to the result of diffraction, scattering absorption of the waves when propagated through the medium with presence of honeycomb.

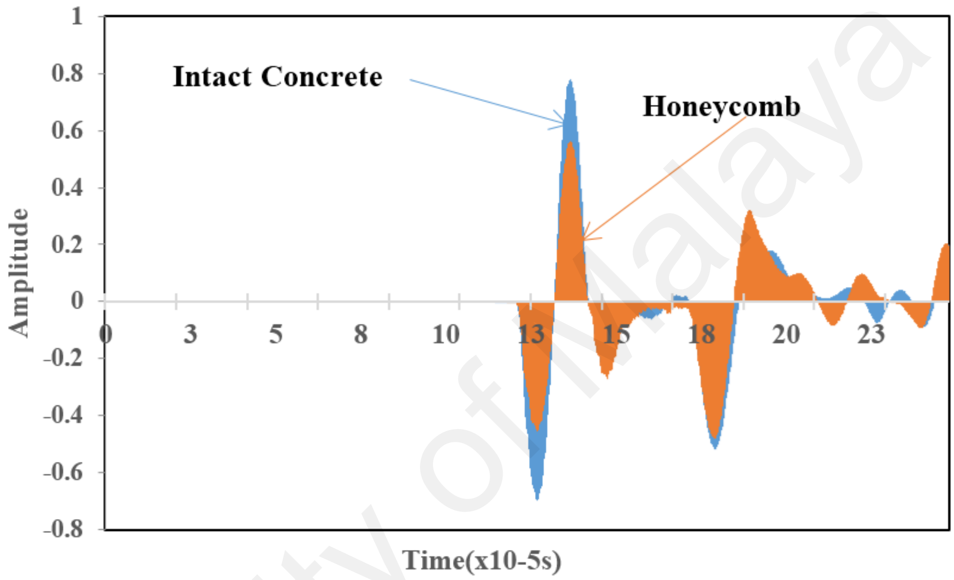

Figure 4.3: Amplitude versus time data of measured waves.

Figure 4.4 is a graph of amplitude versus frequency for a wave that propagates in two types of medium: intact concrete and concrete with honeycomb. Figure 4.4 illustrates that the graph is shifted to the right for intact concrete compared to concrete with honeycomb. In Figure 4.4, the standard deviation of the wave propagated in sound concrete was recorded as 30.02 for amplitude and 0.052 MHz for frequency measurements while for concrete with honeycomb, the registered values were 22.93 and 0.048 MHz for amplitude and frequency, respectively. Thus, the results show that the wave experienced reflection in concrete with honeycomb and some part of the energy was transformed to another form so that the amplitude and frequency that the sensor received for concrete with honeycomb were less than for intact concrete.

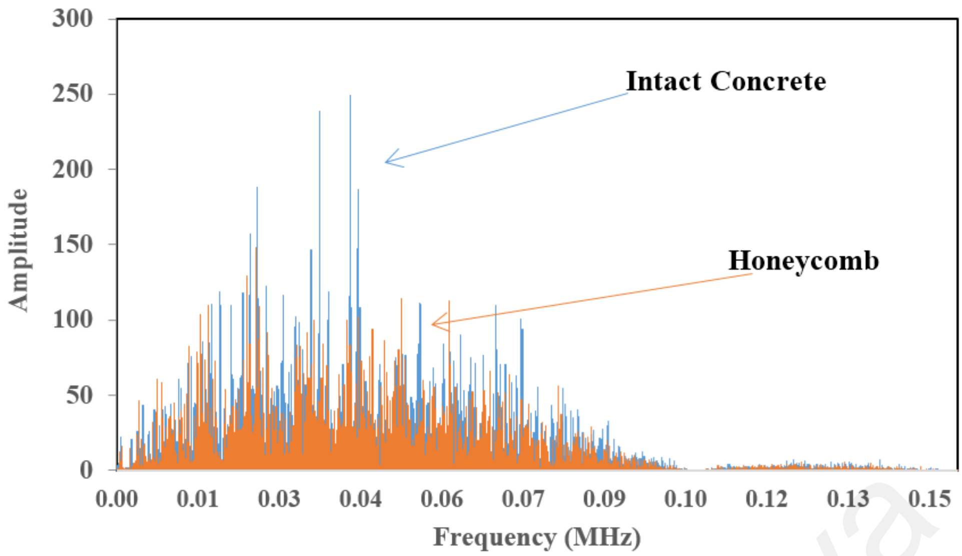

Figure 4.4: Amplitude versus frequency.

4.3 Tomography Reconstruction of Concrete with Honeycomb and Surface Deterioration

4.3.1 Effect of Element Size

Figure 4.5 is shows tomograms generated from numerical simulation of concrete model with honeycomb as in Figure 3.7, tomograms plotted at (a),(c),(e) and (g) are 25 elements and tomograms plotted at (b),(d),(f) and (h) are 100 elements. The results given in Figures 4.5(a) and (b) are constructed based on 2 sided TTT reconstruction, Figure 4.5(c) and (d) are constructed based on 4 sided travel time technique, Figure 4.5(e) and (f) are constructed based on 2 sided amplitude technique, Figure 4.5(g) and (h) are constructed based on 4 sided amplitude technique and the Figure 4.5(i) and (j) are constructed based on 4 sided Q-value technique. For results of TTT, reduction in elastic velocity value is associated with inhomogeneity caused by the honeycomb. For the AT and FT, the attenuation coefficient value becomes higher with the presence of defects. For tomography using Q-value, its magnitude increases with soundness of concrete.

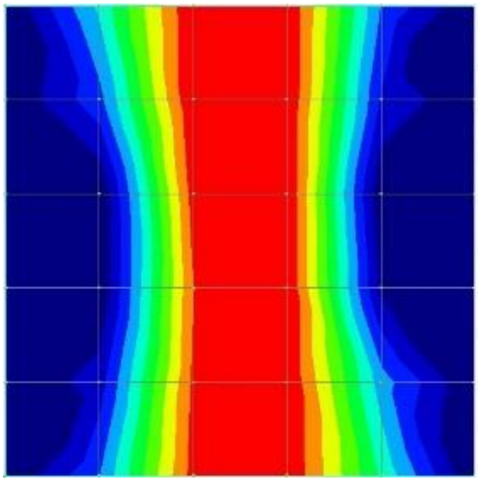

Figure 4.5(a)

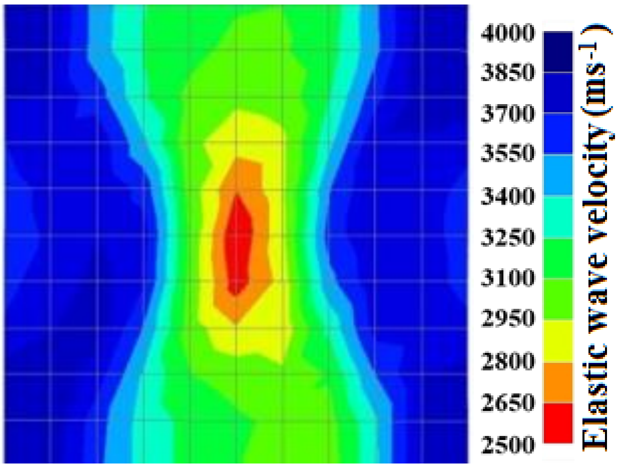

Figure 4.5(b)

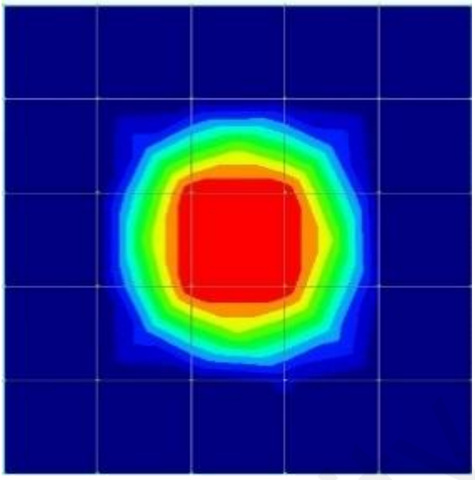

Figure 4.5(c)

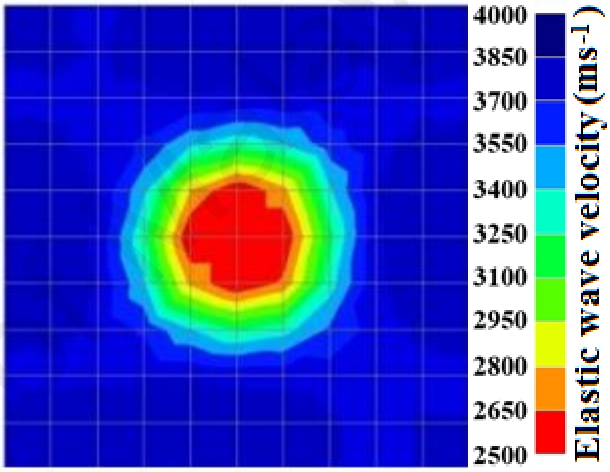

Figure 4.5(d)

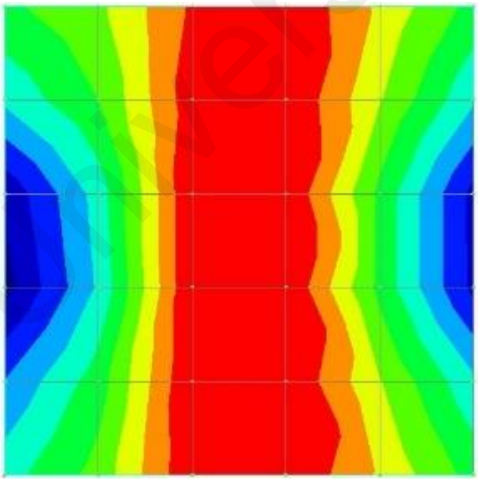

Figure 4.5(e)

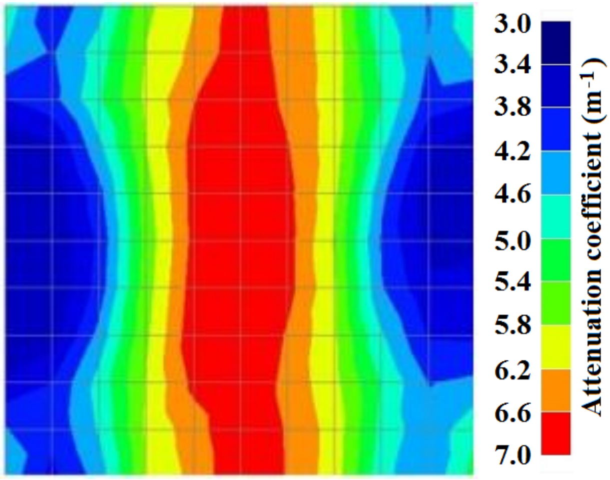

Figure 4.5(f)

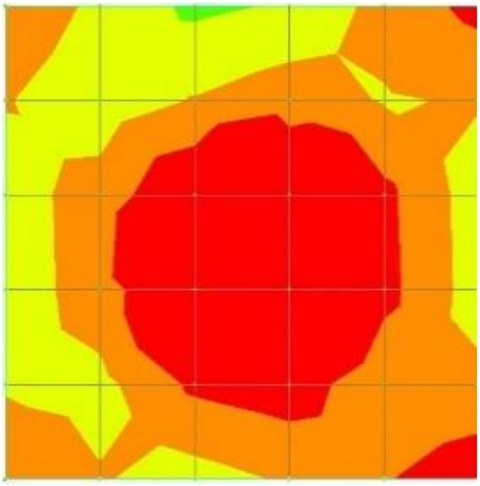

Figure 4.5(g)

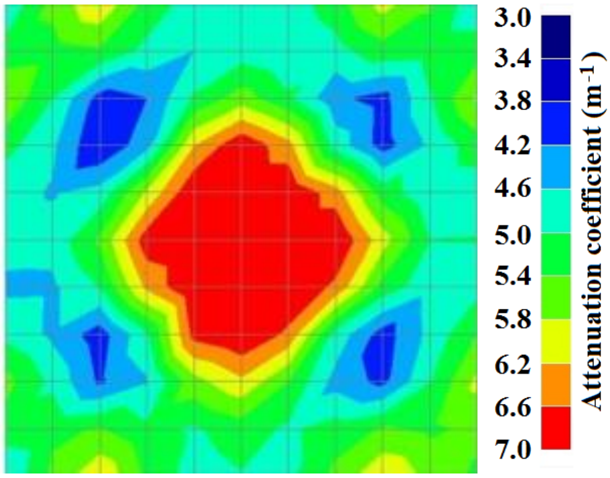

Figure 4.5(h)

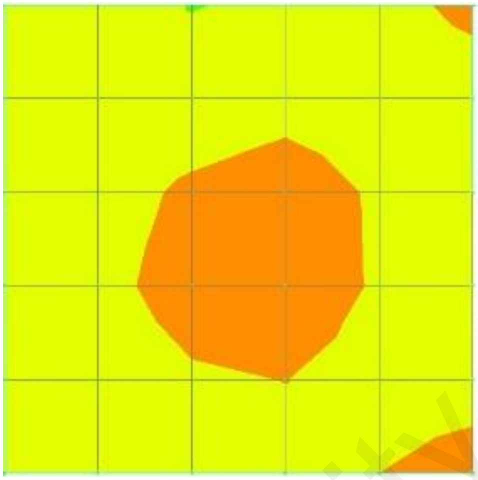

Figure 4.5(i)

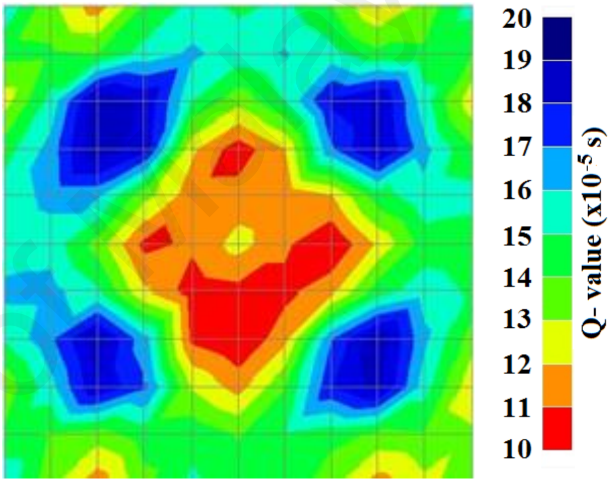

Figure 4.5(j)

Figure 4.5: Comparison of 25 elements (a,c,e,g) with 100 elements (b,d,f,h) for tomogram of concrete with honeycomb that reconstructed from various types of tomography techniques.

The TTT reconstructed by 25 elements demonstrates bigger area of red colour with elastic velocity less than 2650ms^{-1} at the centre than 100 elements. This can be confirmed by comparing the results shown in Figure 4.5(a) with the ones given in Figure 4.5(b), and those in Figure 4.5(c) with the ones in Figure 4.5(d). For AT, tomography plotted by 25 elements shows bigger red colour which with attenuation coefficient higher than 6.6 m^{-1} more than 100 elements. This can be testify by compared Figure 4.5(e) with Figure 4.5(f) and compared Figure 4.5(g) with Figure 4.5(h). This might be attributed to the nature of the amplitude tomogram, for which the decrease of amplitude is due to scattering and absorption of wave energy by the honeycomb. Besides that, the condition of concrete in tomogram plotted with 100 elements has low attenuation coefficient than the tomogram plotted with 25 elements. For example, the concrete in tomogram plotted by 25 elements (Refer Figure 4.5(g)) show attenuation coefficient in range of 6 to 6.6 m^{-1} which tomogram by reconstruction using 100 elements (Refer Figure 4.5(h)) show distribution of attenuation coefficient in a range of 5 to 5.4 m^{-1}. For Q-value tomography, tomogram plotted with 100 elements show its centre with Q-value less than 11 $x10^{-5}$ s which it is in 11 to 12 $x10^{-5}$ s for tomogram plotted by 25 elements. In summary, the tomography plotted by 100 elements shows better visualization than tomogram plotted by 25 elements. 100 numbers of elements has elements size smaller than 25 elements, results show that refines of element size will increase the visualization of tomography. This is because when the element size is decrease, the number of element and number of information for the algorithm to reconstructing the tomogram will be increase. Theoretically, as the number of mesh of algorithm (i.e. j at equation 3.4 for travel time technique, j at equation 3.9 for amplitude technique, j at equation 3.14 for frequency technique) increases, there are more information contributes for the algorithm to reconstruct the tomogram. Therefore, tomograms with 100 elements provide sufficient meshing to compute the amount of scattering and eliminate reflection from the iteration process, whereas tomograms with 25 elements are not able to refine the iteration process.

4.3.2 Effect of Number of Sensors

Figure 4.6 consists of tomograms generated for concrete with honeycomb and surface deterioration as in Figure 3.7, tomograms plotted at left simulated by 12 sensors while tomograms at right are simulated by 20 sensors. Figure 4.6(a) and (b) were constructed based on travel time technique, Figure 4.6(c) and (d) were reconstructed by AT, Figure 4.6(e) and (f) were reconstructed by FT, Figure 4.6(g) and (h) were reconstructed by Q-value tomography.

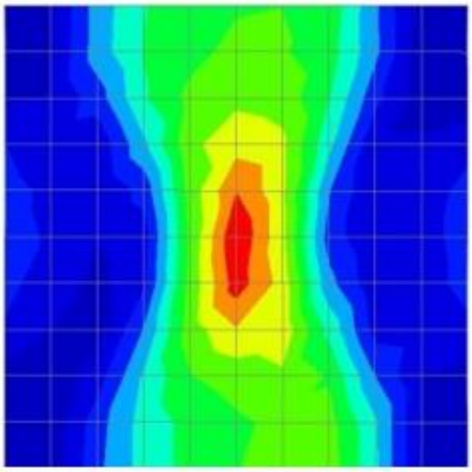

Figure 4.6(a)

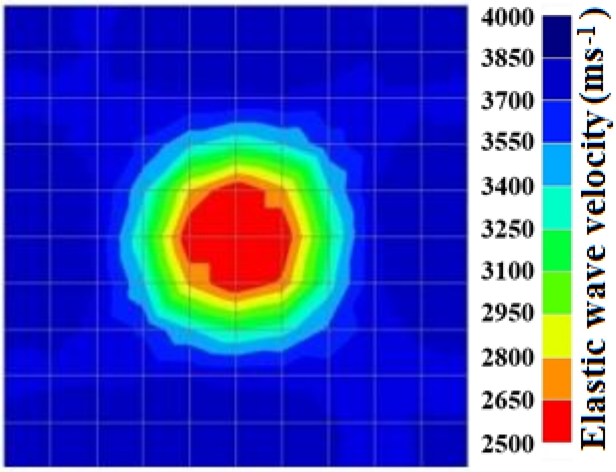

Figure 4.6(b)

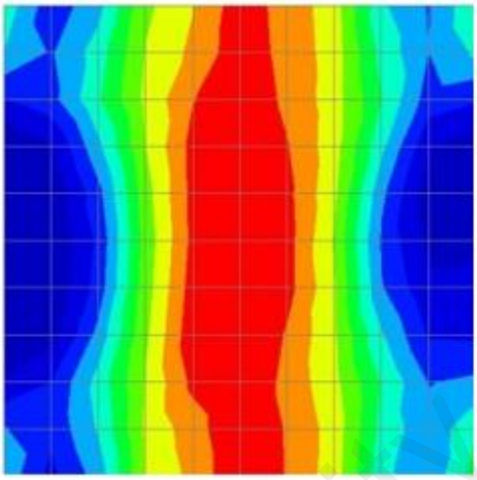

Figure 4.6(c)

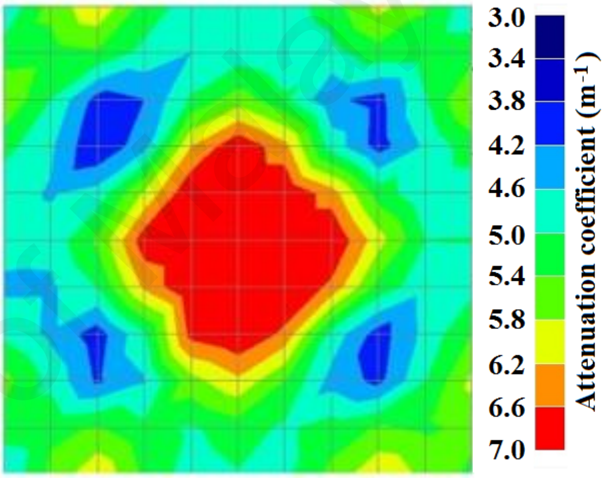

Figure 4.6(d)

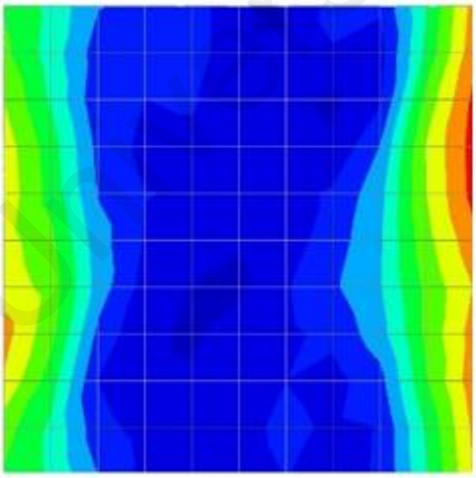

Figure 4.6(e)

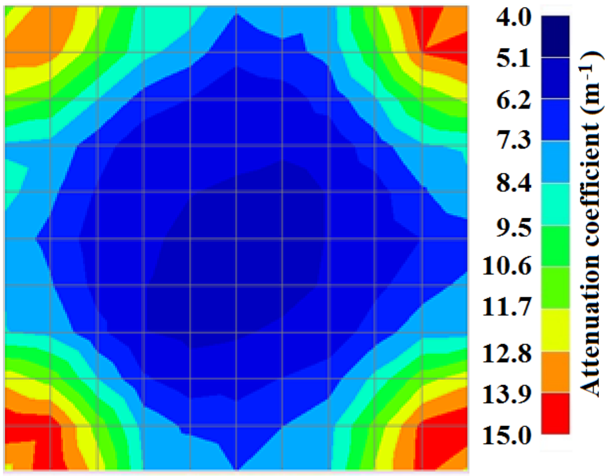

Figure 4.6(f)

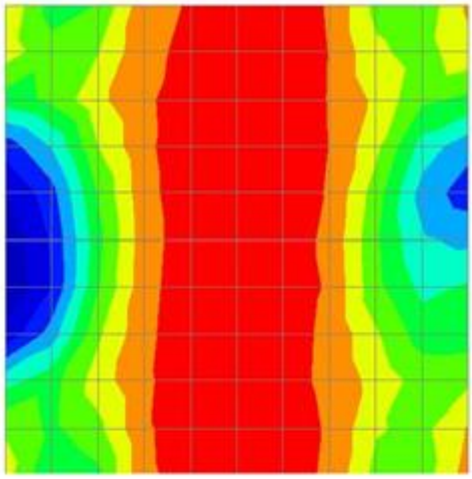

Figure 4.6(g)

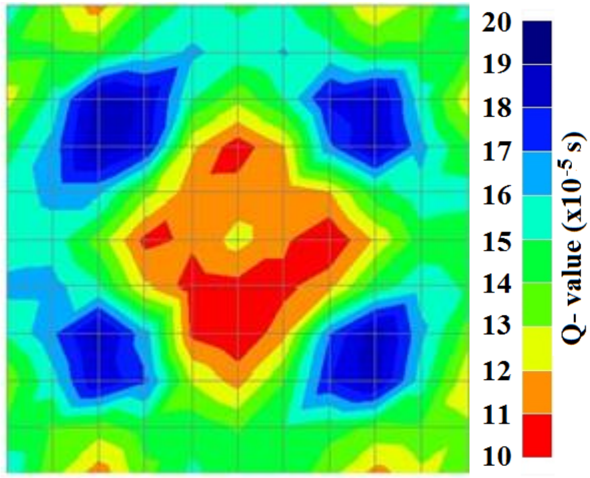

Figure 4.6(h)

Figure 4.6: Comparison of 12 sensors and 20 sensors for tomogram of concrete with honeycomb that reconstructed from various types of tomography techniques.

Tomography of concrete with honeycomb reconstructed by measuring with 12 sensors or 2 sided travel time approach demonstrate the honeycomb with ellipse shape as in Figure 4.6(a) while 20 sensors or 4 sided travel time approach manages to show the honeycomb with cicle shape as in Figure 4.6(b). For AT, 12 sensors indicate the present of honeycomb with an area of indictaed attenuation higher than 6.6m^{-1} while tomography reconstruted by 20 sensors indicate honeycomb with rhombus shape attenuation higher than 6.6 m^{-1} with as in Figure 4.6(c). The results of tomography for concrete with honeycomb that mentioned for AT are same in 2 sided Q-value as of Figure 4.6(g) and 4 sided Q-value as of Figure 4.6(h). For FT, 12 sensors present the centre with blue colour which with attenuation coefficient lower than 7.3 m^{-1} while the left and right sides of tomogram show green colour with 14 m^{-1} which with attenuation coefficient higher than its centre relatively. This is because the left and right sides of the model are falling into an uncover or less coverage of wave information coverage region as show in Figure 4.6(e). However for FT plotted by measureing with 20 sensors, the centre area presented with a big rhombus shape blue colour with attenuation lower than 6.2 m^{-1} as in Figure 4.6(f). The result of FT are not able to explain the present of honeycomb, however the result can be further analyse with superimposed technique which will be explain in soundness section in order to indicate the presence of honeycomb. Overally, surroundings or four corners of tomogram reconstructed by the amplitude, frequency and Q-value techniques show higher attenuation value. This is because of the wave reflection when it arrives at the side and adjacent to the receiver sensor. The reflected wave is normally weak in elastic energy with low amplitude compared to the original wave front. In short, the four-sided measurement provides better visualization than four sided measurement and resolution with higher level of precision due to the increase of input data for the reconstruction process compared to the two sided tomography. Theoretically, as the number of source trigger for algorithm increases, (i.e. i at equation 3.4 for travel time technique, i at equation 3.9 for amplitude technique, i at equation 3.14 for frequency technique) increases, there will be more information available for the algorithm to reconstruct the tomogram and contributes to improve the resolution of tomogram.

4.3.3 Effect of Deterioration Type

Figure 4.7(a) is a tomogram of sound concrete model and Figure 4.7(b) is a tomogram of sound concrete model with surface deteriorate later (V=2500ms^{-1}), both reconstructed by 4-sided travel time approach. Figure 4.7(a) shows the whole concrete with elastic velocity higher than 4000 ms^{-1}. While for Figure 4.7(b), tomogram show the part of surface deteriorate with elastic velocity velocity lower than 3100 ms^{-1}. In addition, the four corners of tomogram show elastic velocity lower than 2650 ms^{-1}. Besides, the centre of cross section shows concrete with elastic velocity higher than 4000 ms^{-1}.

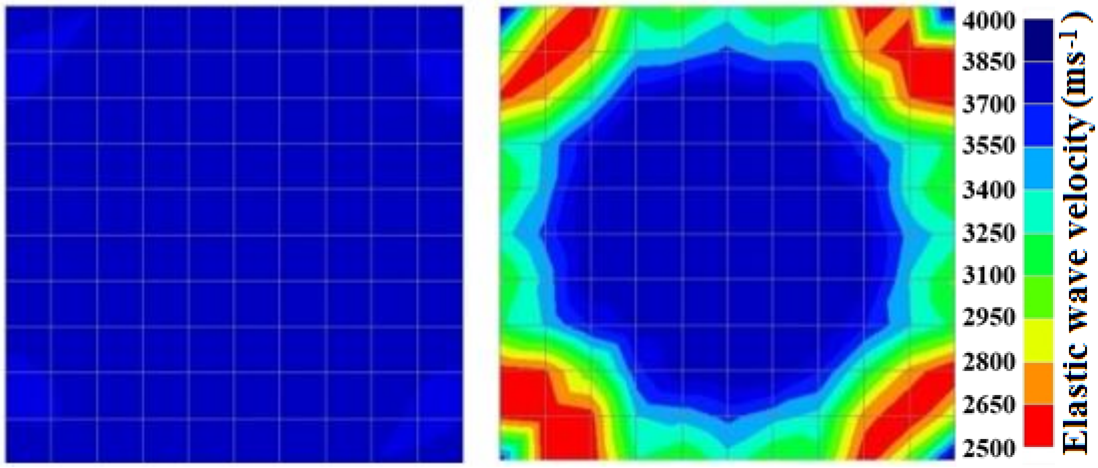

(a) (b)

Figure 4.7: 4-sided TTT:(a) Sound concrete;(b) Concrete with surface deteriorate ($V=2500ms^{-1}$).

Figure 4.8(a) is a tomogram of concrete with honeycomb ($V=1500$ ms^{-1}) and surface deteriorated ($V=2500$ ms^{-1}) and Figure 4.8(b) is a tomogram of concrete model with honeycomb ($V=2500$ ms^{-1}) and surface deteriorated ($V=1500$ ms^{-1}) measuring with 4 sided travel time technique. The tomogram Figure 4.8(a) is able to indicate the presence of honeycomb by showing the circle at the centre with elastic velocity lower than 2650 ms^{-1}. Besides, Figure 4.8(a) and Figure 4.8(b) manage to show that there is a gap in between the surface deterioration and honeycomb with elastic velocity higher than 4000 ms^{-1}. In tomogram Figure 4.8(b), the centre of the tomogram show circle with elastic velocity around 3000 ms^{-1} . However for 4.8(b), the areas of surface deteriorate show elastic velocity lowers than 2650 ms^{-1}. This is because the elastic velocity of the honeycomb was set higher than surface deteriorates for case of Figure 4.8(a).

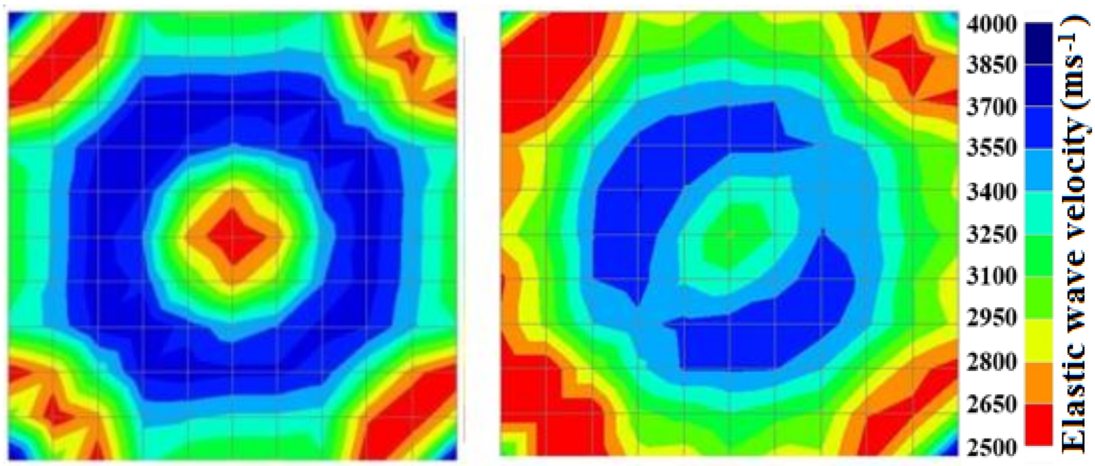

(a) (b)

Figure 4.8: 4-sided TTT:(a) concrete model with honeycomb(V=1500 ms^{-1}) and surface deteriorated(V=2500 ms^{-1}) ;(b) Concrete model with honeycomb(V=2500 ms^{-1}) and surface deteriorated(V=1500 ms^{-1}).

Figure 4.9(a) is a tomogram of concrete model with honeycomb (V=1500ms^{-1}) and Figure 4.9(b) is a tomogram of concrete model with honeycomb (V=1500ms^{-1}) and surface deteriorated (V=2500ms^{-1}) that reconstructed by 2 sided amplitude technique. The tomogram of Figure 4.9(a) indicates the present of honeycomb at centre by showing red colour with attenuation coefficient higher than 6.6 m^{-1}. However, the tomogram Figure 4.9(b) indicates the presence of surface deterioration by showing the left and right sides of the concrete cross section with attenuation coefficient higher than 6.6 m^{-1}. The centre of tomogram Figure 4.9(b) shows green colour which indicate the attenuation coefficient in around 5.4 m^{-1}.

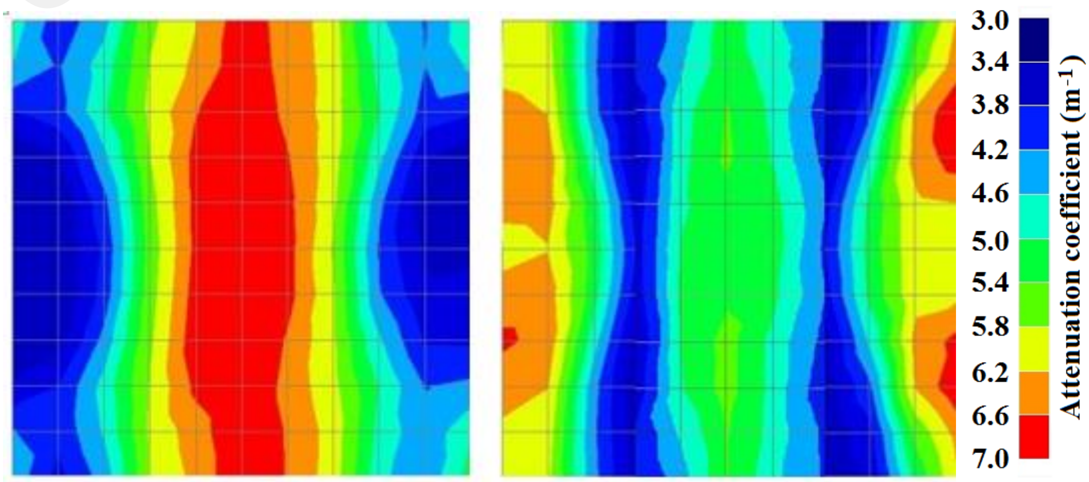

(a) (b)

Figure 4.9: 2 sided AT: (a) concrete with honeycomb only and (b) Concrete with honeycomb and surface deterioration.

Figure 4.10(a) and Figure 4.10(c) are tomograms of concrete model with honeycomb and surface deterioration, Figure 4.10(b) and Figure 4.10(d) are tomograms of concrete model with honeycomb and deteriorated surface. Both Figure 4.10(a) and Figure 4.10(b) are reconstructed by 4-sided amplitude technique while both Figure 4.10(c) and Figure 4.10(d) are reconstructed by 4 sided Q-value technique. 4.10(a) and Figure 4.10(c) able to show the presence of surface deteriorate with four corners with attenuation coefficient higher than 6.6 m^{-1} by amplitude technique while lower than $11x10^{-5}$ s by Q-value technique. Besides, Figure 4.10(a) and Figure 4.10(c) show same pattern of rhombus shape at the centre which with attenuation coefficient in around 5.4 m^{-1} by amplitude technique while in between $15x10^{-5}$ s by Q-value technique. Nevertheless, Figure 4.10(a) and Figure 4.10(c) did shows that there is a gap in between the surface deterioration and honeycomb with attenuation coefficient lower than 4.2 m^{-1} by amplitude technique while in between $17x10^{-5}$ s by Q-value technique. In tomogram Figure 4.10(b), the tomogram at centre show blue colour with attenuation coefficient lower than 4.2 m^{-1} and the wider angle of tomogram show red colour which with attenuation coefficient higher than 6.6 m^{-1}. The result of tomogram Figure 4.10(b) and Figure 4.10d) show that the wave had reflected when it propagated at deteriorated surface as the wave was unable to reach to the location of honeycomb. Thus, the amplitude and Q-value techniques are unable to detect honeycomb because of the presence of surface deterioration that with condition of deteriorated surface is poorer than honeycomb.

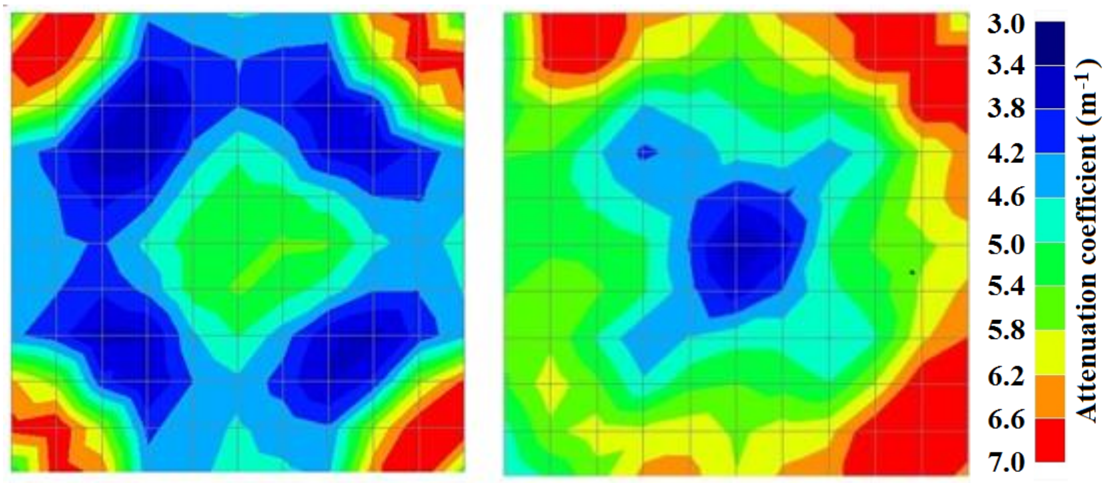

Figure 4.10 (a) Figure 4.10 (b)

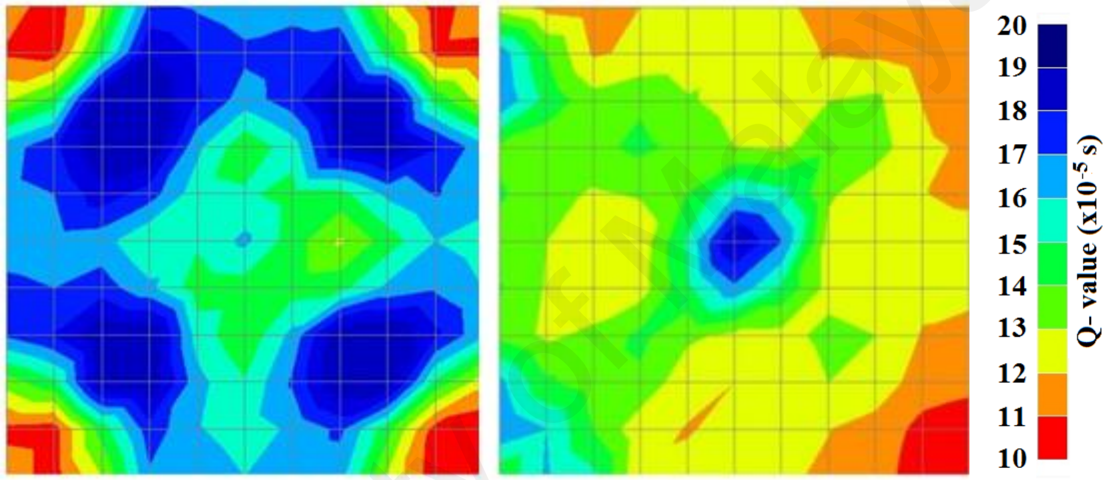

Figure 4.10 (c) Figure 4.10 (d)

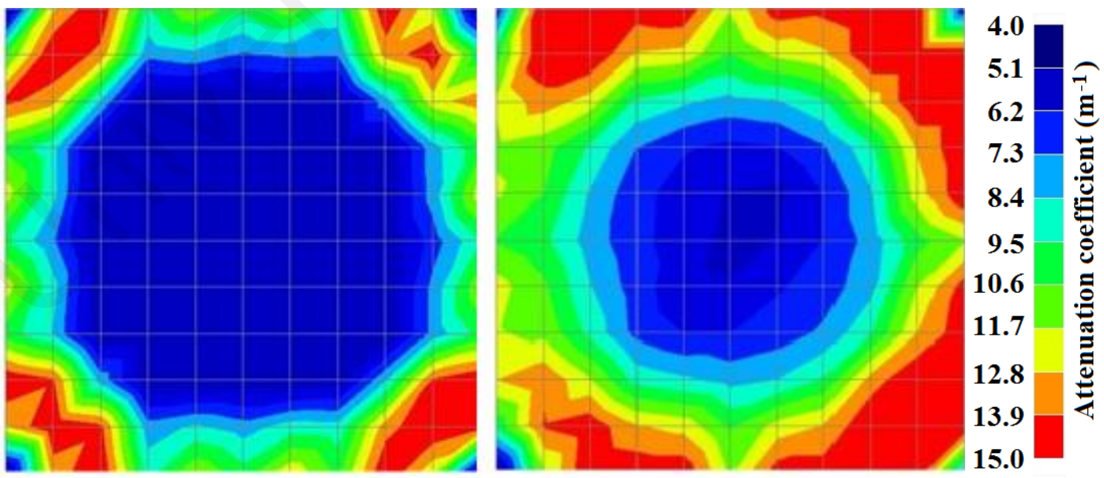

Figure 4.10 (e) Figure 4.10 (f)

Figure 4.10: Comparison between tomography of concrete with honeycomb and concrete with honeycomb and surface deteriorated by 4 sided amplitude and Q-value techniques.

Figure 4.11(a) is a tomogram of concrete model with honeycomb (V=1500 ms^{-1}) and Figure 4.11(b) is a tomogram of concrete model with honeycomb(V=1500 ms^{-1}) and surface deterioration (V=2500 ms^{-1}) reconstructed by 4-sided frequency technique. The four edges of 4-sided frequency tomogram for sound concrete are in green colour with attenuation coefficient in between 11m^{-1}. It shows that the four edges of frequency tomogram always have low soundness although it is a sound concrete. Tomogram Figure 4.11(b) shows the attenuation coefficient at the centre is higher than centre of Tomogram Figure 4.11(a) because of the presence of honeycomb. Besides that, the four edges of tomogram show red colour with attenuation coefficient higher than 13.9 m^{-1} which is higher than four edges of Figure 4.11(a).

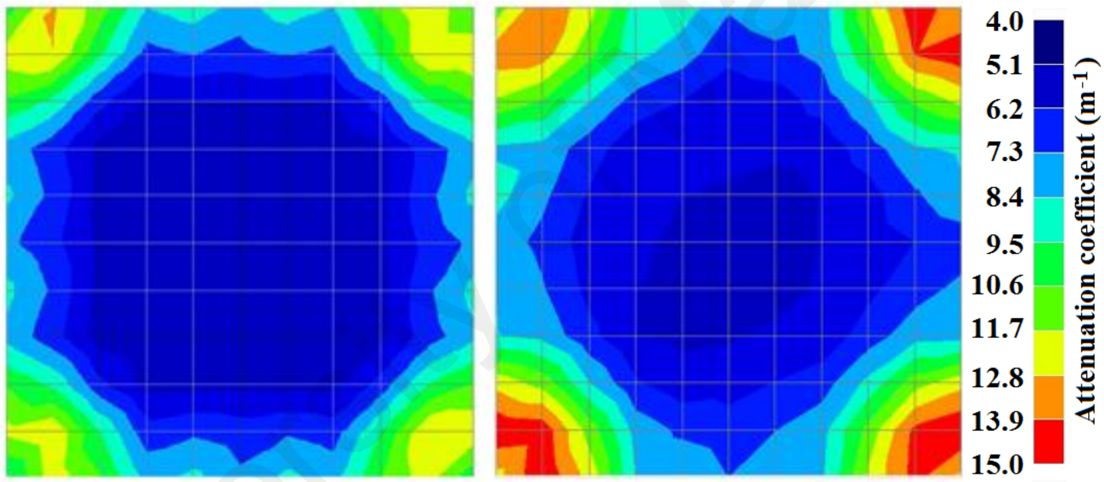

Figure 4.11 (a) Figure 4.11 (b)

Figure 4.11: 4-sided FT:(a) Sound concrete model;(b) Concrete model with honeycomb.

Figure 4.12(a) is a tomogram of concrete model with honeycomb(V=1500 ms^{-1}) and surface deteriorated (V=2500 ms^{-1}) and Figure 4.12(b) is a tomogram of concrete model with honeycomb (V=2500 ms^{-1}) and surface deteriorated (V=1500 ms^{-1}), both are that reconstructed by 4-sided frequency technique. Both of Figure 4.12(a) and Figure 4.12(b) show it four sides with higher attenuation coefficient than its centre. However, the area at centre for Figure 4.12(a) with attenuation coefficient lower that 7.3 m^{-1} is bigger than figure 4.12(b) because of honeycomb of Figure 4.12(b) is weak than honeycomb of Figure 4.12(a).

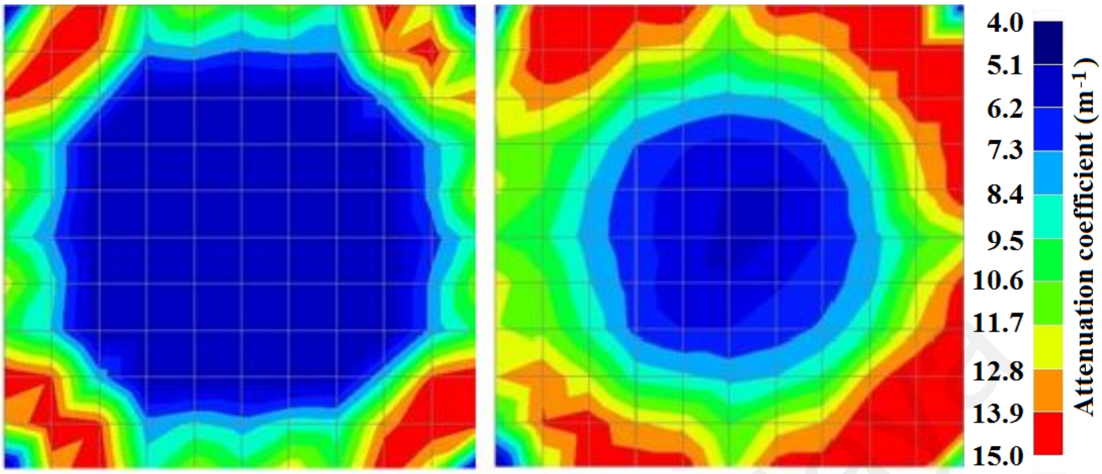

(a) (b)

Figure 4.12: 4-sided FT:(a) Sound model with honeycomb(V=1500 ms^{-1}) and surface deteriorated(V=2500ms^{-1}) ;(b) Concrete with honeycomb(V=2500 ms^{-1}) and surface deteriorated(V=1500 ms^{-1}).

4.3.4 Soundness

Soundness of tomogram is outcome of superimposing the results of the model with honeycomb with those of sound concrete model. Figure 4.13(a) and 4.13(b) are soundness of concrete with honeycomb while Figure 4.13(a) and 4.13(b) are soundness of concrete model with surface deterioration (V=2500 ms^{-1}) and honeycomb (V=1500 ms^{-1}). Figure 4.13(a) and 4.13(c) are tomograms obtained from 2 sided travel time technique while Figure 4.13(b) and 4.13(d) are obtained from 4-sided travel time technique. The Figure 4.13(a) and Figure 4.13(c) implies that the honeycomb with soundness around 85% and with the shape of defect as oval. However, the visualization has become better with 4-sided measurements with the honeycomb seem to be in circle and is more representable to the size of defect. With the incorporation of surface deterioration into the concrete model, the area with soundness lower than 90% at Figure 4.13(d) is seems to be smaller than the area of the red spot in Figure 4.13(b). Thus, the incorporation of surface deterioration had caused that travel time technique to be less sensitive towards honeycomb.

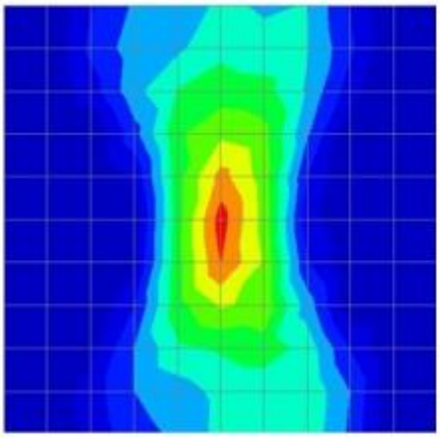

Figure 4.13 (a)

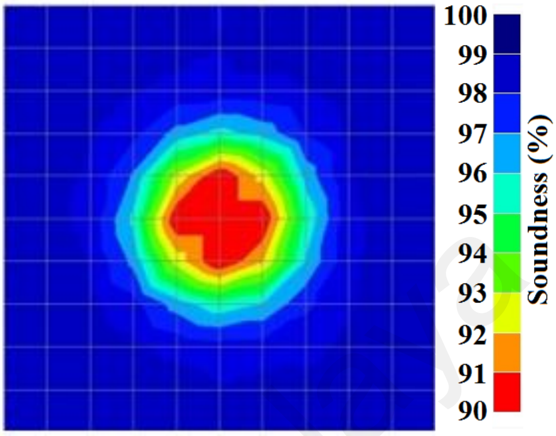

Figure 4.13 (b)

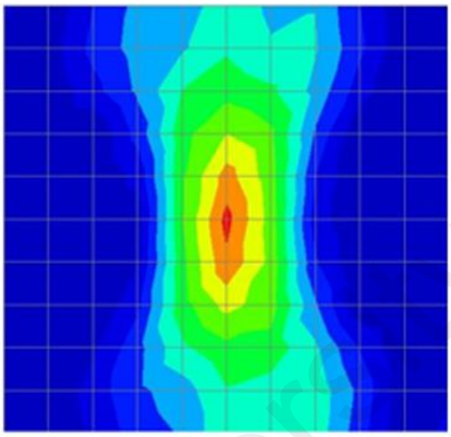

Figure 4.13 (c)

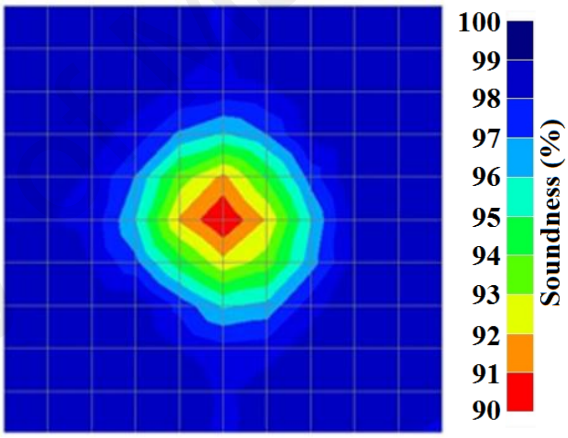

Figure 4.13 (d)

Figure 4.13: Soundness of Tomogram reconstructed by: (a) (c):2 side travel time technique ;(b) (d): 4-sided travel time technique.

Figure 4.14(a) and 4.14(b) are soundness of concrete with honeycomb while Figure 4.14(a) and 4.14(b) are soundness of concrete model with deterioration surface (and honeycomb. Figure 4.14(a) and 4.14(c) are tomograms obtained from 2 sided amplitude technique while Figure 4.14(b) and 4.14(d) are obtained from 4 sided amplitude technique. Figure 4.14(a) and 4.14(c) both show the centre with yellow colour of soundness in between 76 to 79%. The four-sided measurements as in Figure 4.14(b) and 4.14(d) have better visualization than two-sided measurements of Figure 4.14(a) and 4.14(b) as Figure 4.14(b) and 4.14(d) both show honeycomb with red colour of soundness lower than 73% and in circle shape.

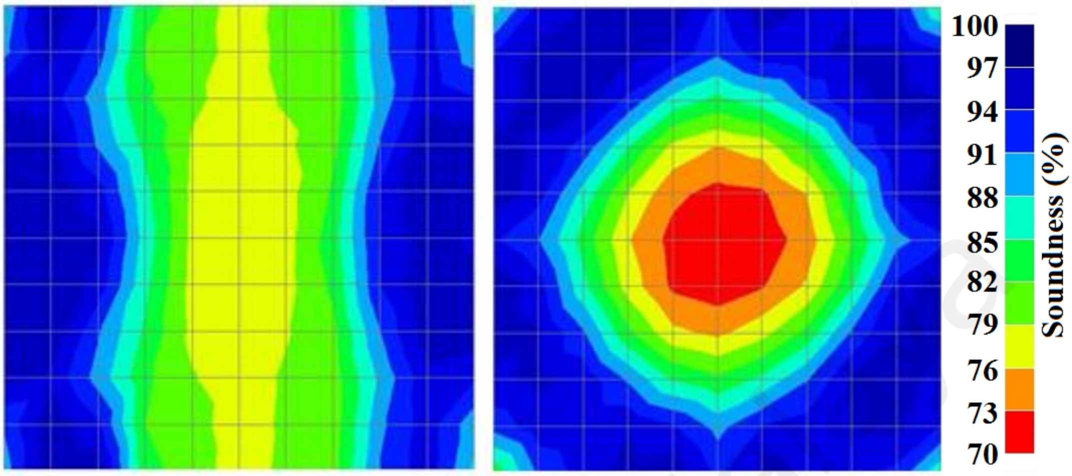

Figure 4.14 (a) Figure 4.14 (b)

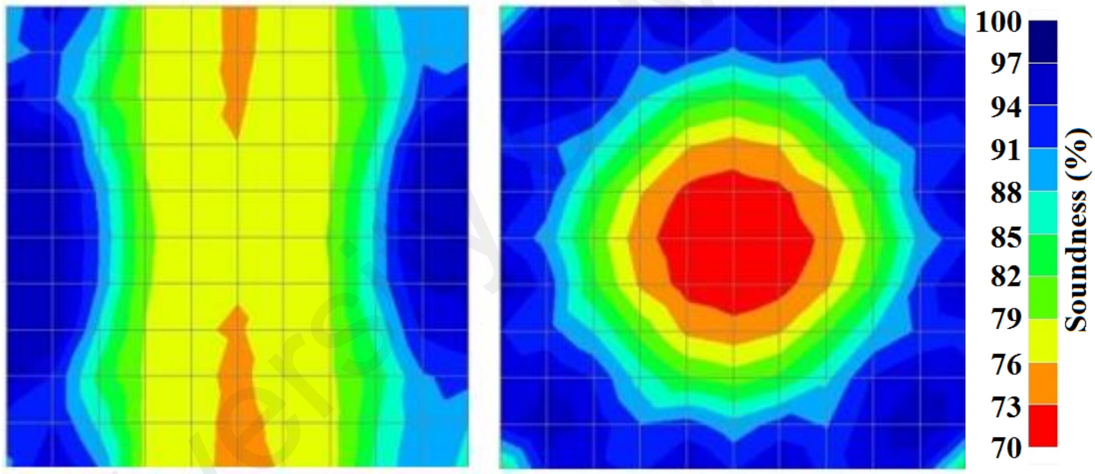

Figure 4.14 (c) Figure 4.14 (d)

Figure 4.14: Soundness of Tomogram case Figure 3.7 with honeycomb by: (a) 2 side amplitude technique ;(b) 4 sided amplitude technique.

Figure 4.15 (a) is a tomogram measuring by 2 sided frequency technique while Figure 4.15(b) is a tomogram measuring by 4 sided frequency technique, both are concrete model with honeycomb. The tomogram Figure 4.15(a) shows that soundness at the centre are low than left and red sides. For four-sided measurements, the centre of tomogram shows red colour of soundness lower than 59.5% and lower than its surrounding. Previously, the tomogram of Figure 4.6(e) and Figure 4.6(f) are unable to display defect by FT. However, with the superimposed technique, Figure 4.15(a) and Figure 4.15(b) are able to show the presence of defect. By superimposed of case normal concrete and concrete with defect, tomogram is able to show the presence of flaw in concrete by showing the reduction in their respective soundness at the part where presence of flaw.

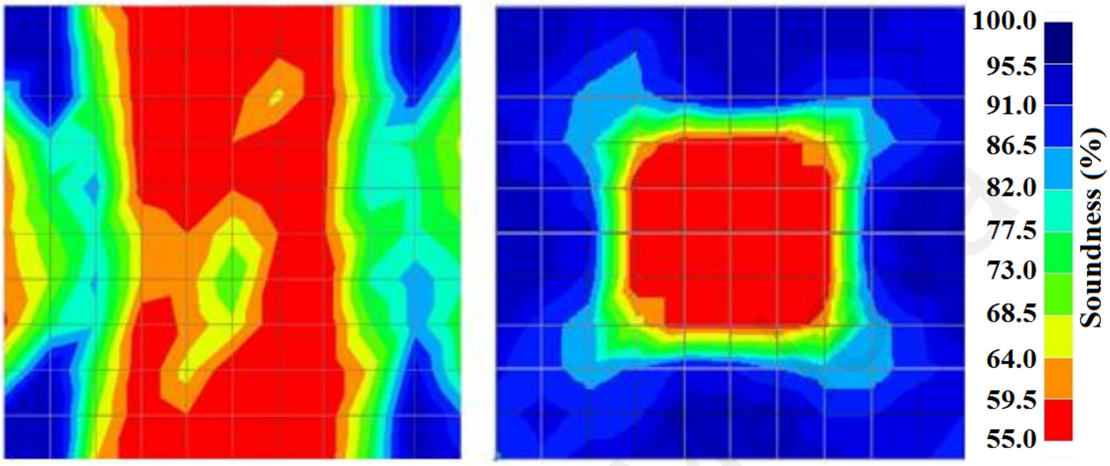

(a) (b)

Figure 4.15: Soundness of Tomogram case Figure 3.7 with honeycomb by: (a) 2 side measurements frequency technique ;(b) 4 sided measurements frequency technique.

Figure 4.16(a) is a tomogram obtained from 2 sided frequency technique while Figure 4.16(b) from 4-sided frequency technique, both are concrete model with surface deterioration and honeycomb with the incorporation of surface deterioration into concrete model, the soundness at the centre of Figure 4.16(a) had increased to 70% and it is in green. By comparing the Figure 4.15 with Figure 4.16, the incorporation of surface deterioration causes frequency technique to be less sensitive towards honeycomb.

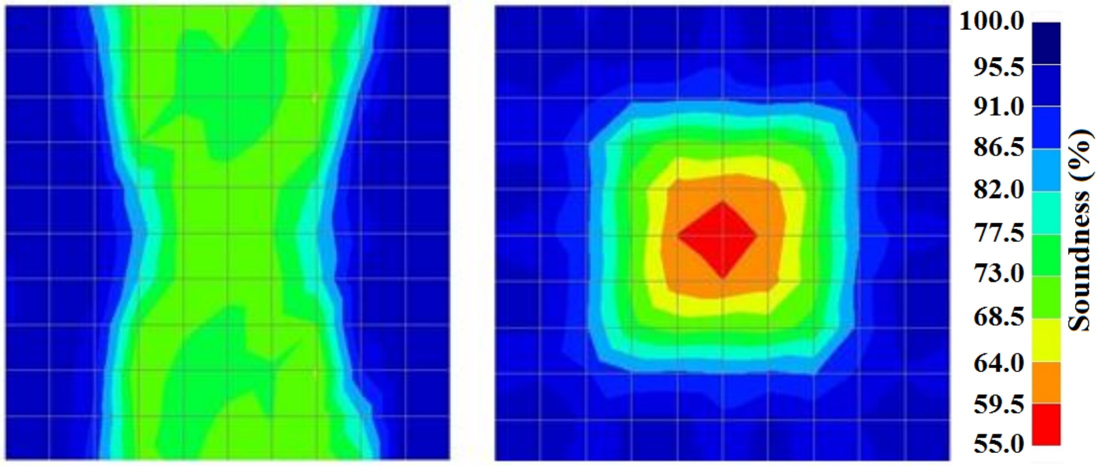

(a) (b)

Figure 4.16: Soundness of Tomogram case Figure 3.8 with honeycomb and surface deteriorated by: (a) 2 side measurements frequency technique ;(b) 4-sided measurements frequency technique.

Figure 4.17(a) is a tomogram obtained from 2 sided travel time technique while Figure 4.17(b) from 4 sided travel time technique, both are concrete specimens with honeycomb. The Figure 4.17(a) shows that the centre of tomogram with red and orange colour in which the soundness is under 92 %, while the left and right side of tomogram have soundness higher than centre relatively. For four-sided measurements, the centre of tomogram indicates the honeycomb by showing lowest soundness among the whole cross section of tomogram which is under 92 %.

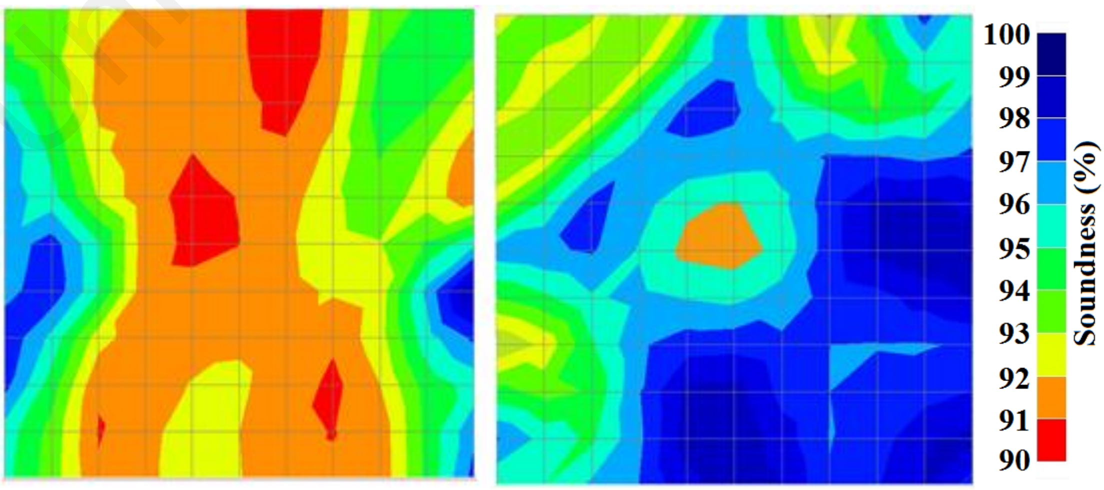

(a) (b)

Figure 4.17: Soundness of Tomogram case Figure 3.7 by laboratory raw data: (a) 2 side measurements travel time technique ;(b) 4 sided measurements travel time technique.

Figure 4.18(a) is a tomogram obtained from 2 sided amplitude technique while Figure 4.18(b) from 4 sided amplitude technique, both concrete specimens with honeycomb. The centre of Figure 4.18(a) show soundness of 88% has low soundness lower its left and right sides with soundness higher than 94%. For four-sided amplitude technique measurements as in Figure 4.18(b), the centre of tomogram show yellow, orange and red colours with soundness less than 85% and this imply that four-sided measurements is more sensitive than two-sided amplitude technique.

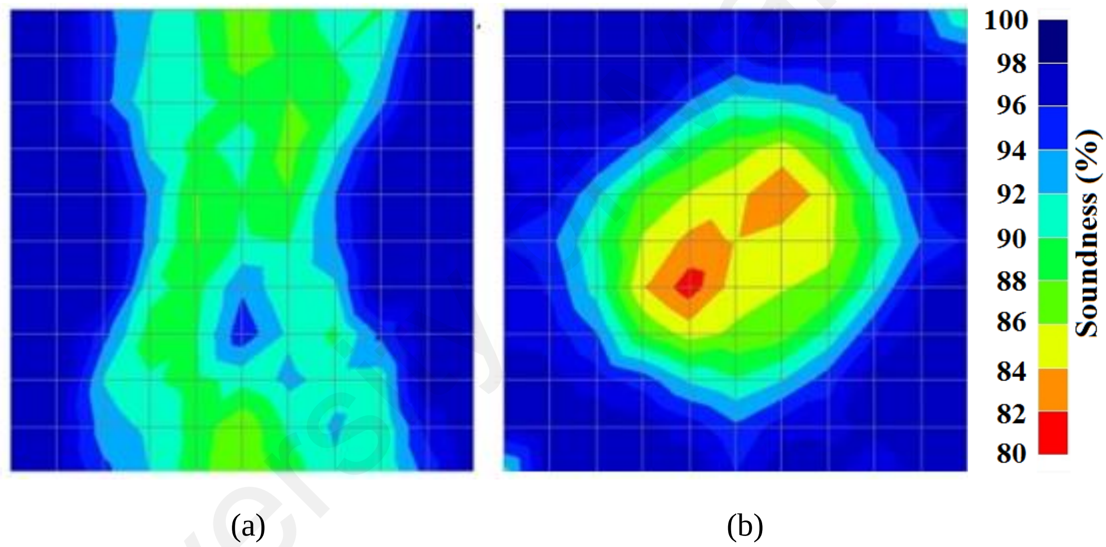

Figure 4.18: Soundness of Tomogram case Figure 3.7 by laboratory raw data: (a) 2 sided amplitude technique ;(b) 4 sided amplitude technique.

Figure 4.19(a) is a tomogram obtained from 2 sided frequency technique while Figure 4.19(b) from 4 sided frequency technique, both concrete specimens are with honeycomb. The centre of Figure 4.19(a) has low soundness if compared to its left and right sides respectively. For four-sided frequency measurements as in Figure 4.19(b), the centre of tomogram show red colour with soundness less than 59.5% which indicated the presence of honeycomb. Besides, the location of the flaw that displays by four-sided measurement is more accurate and sensitive than two-sided measurements.

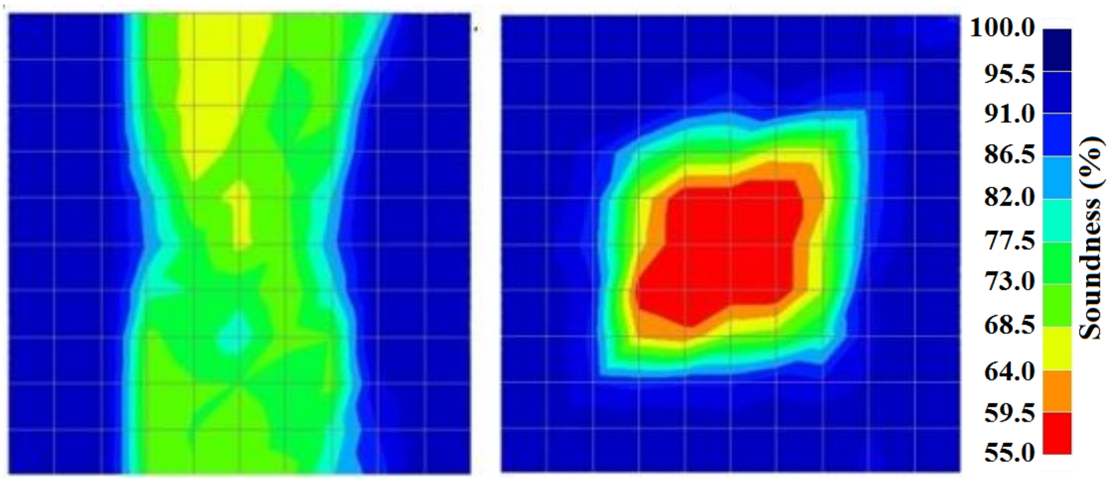

(a) (b)

Figure 4.19: Soundness of Tomogram case Figure 3.7 by laboratory raw data: (a) 2 sided frequency technique ;(b) 4 sided frequency technique.

Figure 4.20 presents average soundness of concrete model with honeycomb by two-sided and four-sided measurements of four types of tomography technique which is travel time, amplitude, frequency and Q-value. The average soundness is calculated by taking the percentage of total soundness and divided with the total number of cells. The travel time technique is the less sensitive among four techniques studied because the two-sided travel time measurements have average soundness of 95.74% while four-sided measurements have 97.61%. The amplitude technique is second sensitive among four techniques because of the two-sided amplitude measurements have average soundness of 80.483% while four-sided measurements have 75.71%. The Q-value technique is third because of the two-sided Q-value measurements have average soundness of 65.19% while four-sided measurements have 68.13%. The FT sometime may be too sensitive as the average of the two-sided frequency measurements has average soundness of 53.31% while four-sided measurements have 57.25%.

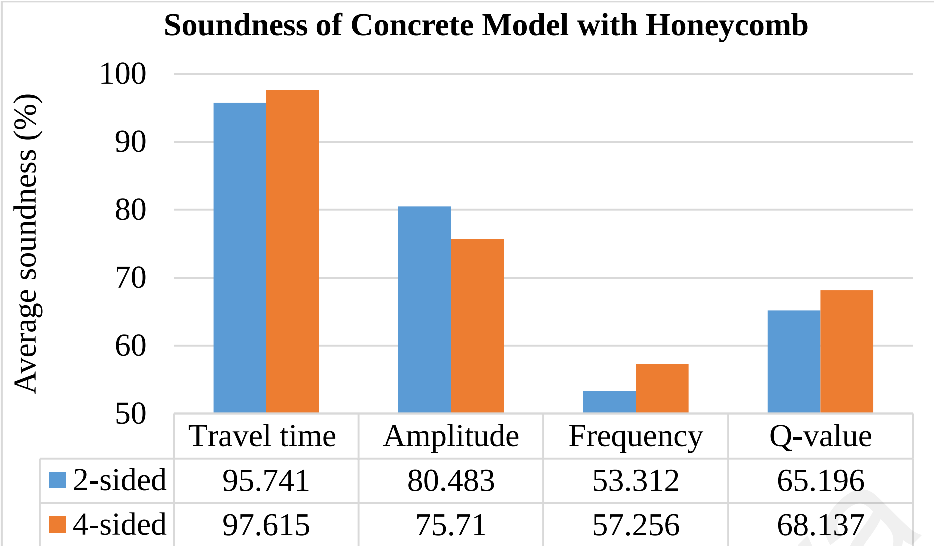

Figure 4.20: Histogram of average soundness for concrete model with honeycomb.

Figure 4.21 presents average soundness of a concrete specimen with honeycomb by two-sided and four-sided measurements of four types of tomography technique which is travel time, amplitude, frequency and Q-value. The topography of the four techniques were reconstructed based on raw data that acquired laboratory. The travel time technique is the less sensitive among four techniques studied because the two-sided travel time measurements have average soundness of 93.72% while four-sided measurements have 98.73%. The amplitude technique is second sensitive among four techniques because of the two-sided amplitude measurements have average soundness of 86.38% while four-sided measurements have 74.82%. The average soundness of two-sided measurements by frequency technique is 70.31%, while the Q-value is 72.41%. Besides that, the average soundness of four-sided measurements by frequency technique is 62.32%, while the Q-value is 79.82%.

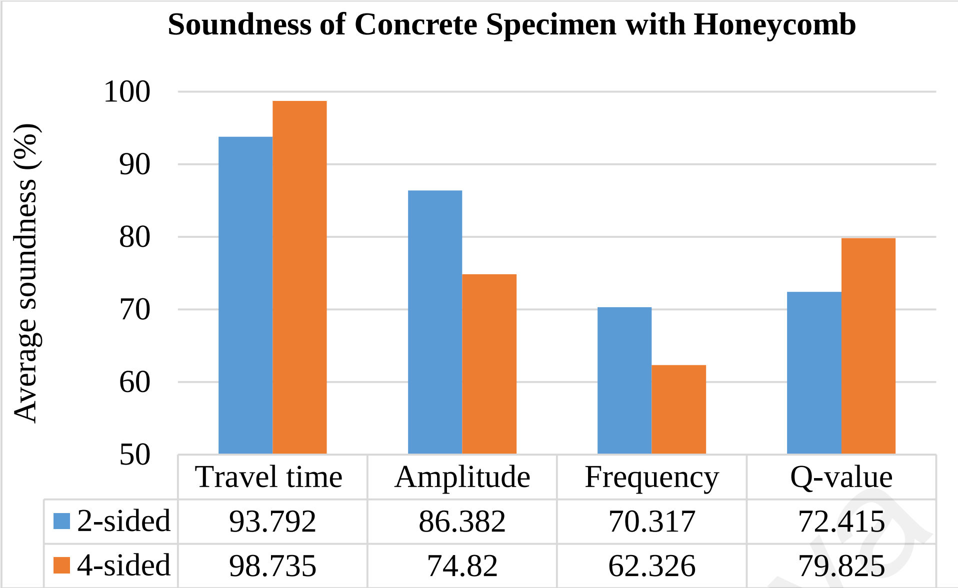

Figure 4.21: Histogram of average soundness for concrete specimen with honeycomb.

4.4 Tomography reconstruction of Grout Partially Grouted PC

4.4.1 Travel time technique

Figure 4.22(a) is a tomogram plotted by comparing sound condition of 0% grout filling with 100% grout filling of aluminium sheath PC model from 2 sided travel time measurements tomogram. Figure 4.22(a) illustrated the presence of void by showing red colour with soundness in between 91%. The Figure 4.22(b) is soundness for 50% grout filling and the centre show yellow colour with soundness of 93% which is less critical than in Figure 4.22(a). Figure 4.23(a) is a soundness of 0% grout filling of aluminium sheath PC model with four-sided travel time measurements. The display of void has become a circle in shape on Figure 4.23(a) if compared to oval in Figure 4.22(a). Besides, the soundness on the centre has increased from 95% in figure 4.23(a) to 97% in Figure 4.23(b) because of 50% grout filling.

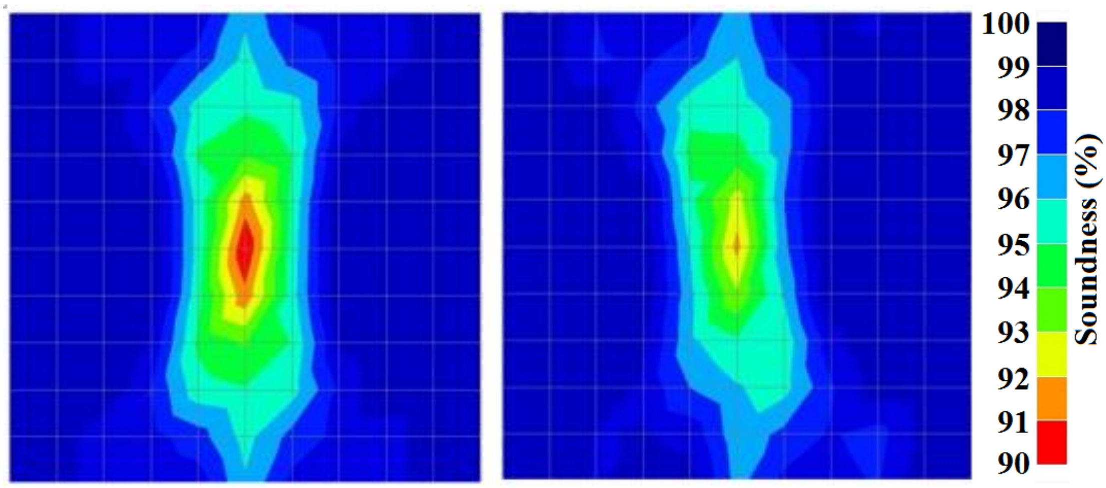

(a) (b)

Figure 4.22: Soundness of tomogram case Figure 3.9 with aluminum sheath PC model that tested by 2 sided travel time technique:(a) 0 % grout filling; (b) 50 % filling.

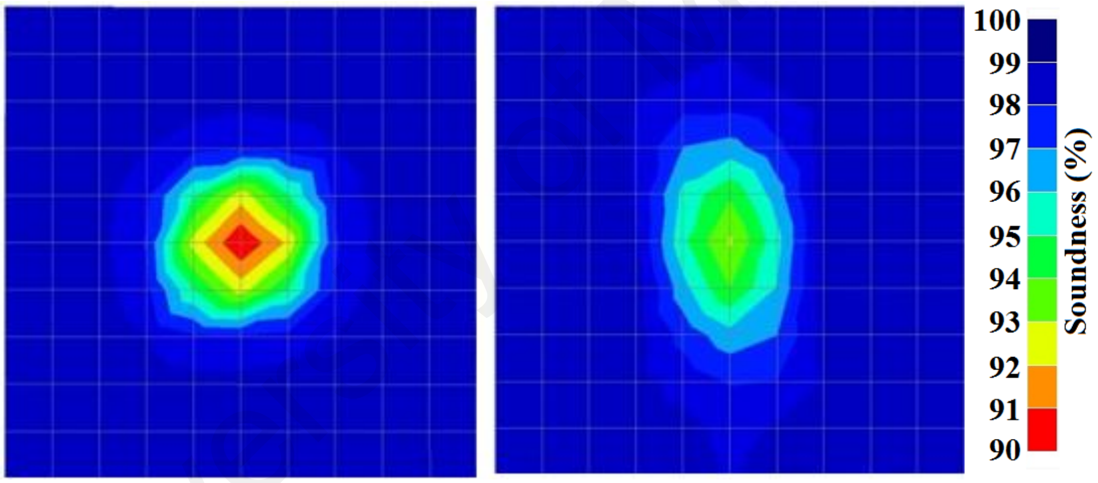

(a) (b)

Figure 4.23: Soundness of tomogram case Figure 3.9 with aluminum sheath PCmodel that tested by 4 sided travel time technique:(a) 0 % grout filling; (b) 50 % filling.

Figure 4.24(a) is a tomogram plotted for soundness of 0% grout filling of aluminium sheath PC model with steel tendon while Figure 4.24(b) is soundness of 50% grout filling of aluminium sheath PC model with steel tendon, both from 2 sided measurement travel time technique. By the incorporation of a steel tendon into an aluminium sheath PC model, the soundness of 0% grout filling is dropping if compared to Figure 4.22(a). Similarly, to the soundness of 50% grout filling in Figure 4.24(b), the adding of a steel tendon into PC model had increased the sensitivity of the travel time technique towards the void. Figure 4.25(a)is a tomogram measuring by soundness of 0% grout filling of aluminium sheath PC model with steel tendon while Figure 4.25(b) shows soundness of 50% grout filling of aluminium sheath PC model with steel tendon, both from 4 sided measurement travel time technique. The indicators of void in Figure 4.25(a) and Figure 4.25(b) are better than Figure 4.23(a) and Figure 4.23(b).

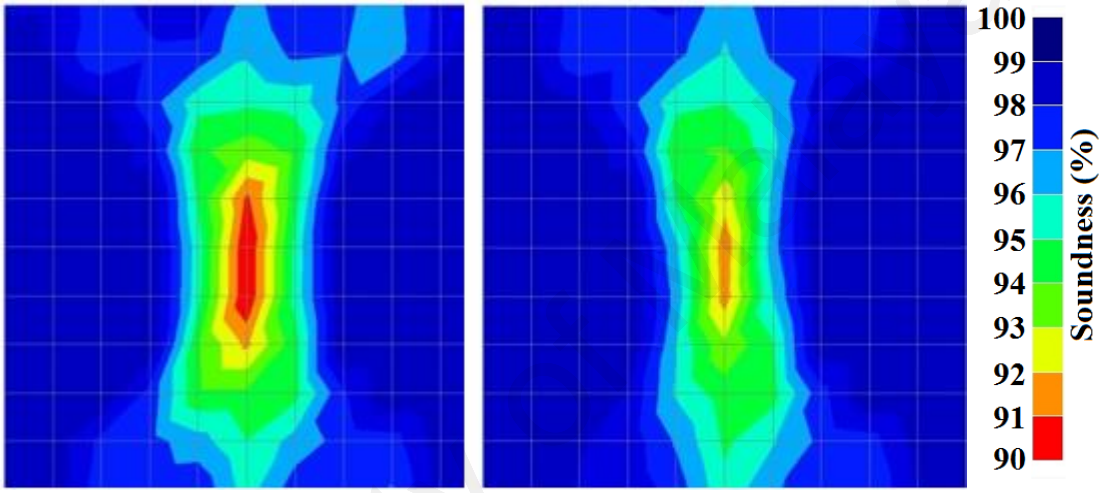

(a) (b)

Figure 4.24: Soundness of tomogram case Figure 3.10 for aluminium sheath PC model with steel tendon that tested by 2 sided travel time technique:(a) 0 % grout filling; (b) 50 % filling.

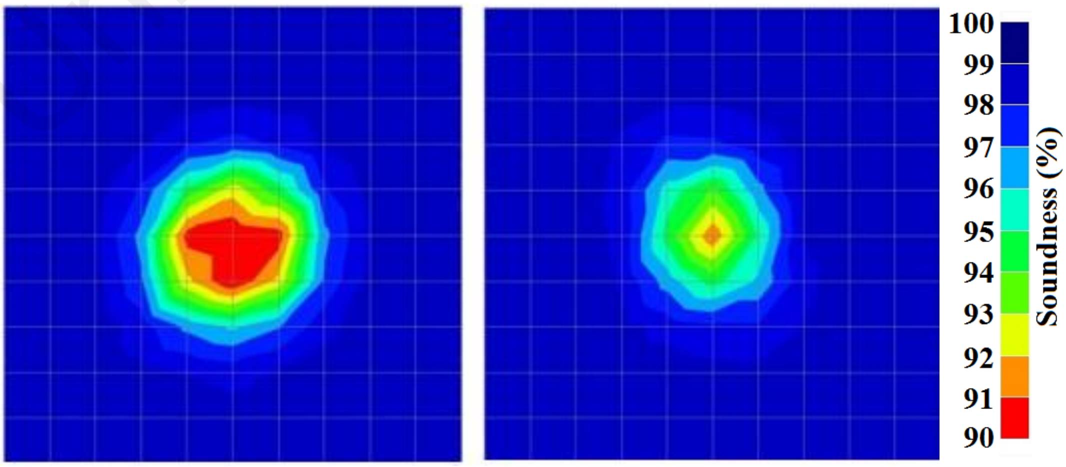

(a) (b)

Figure 4.25: Soundness of tomogram case Figure 3.10 for aluminium sheath PC model with steel tendon that tested by 4 sided travel time technique:(a) 0 % grout filling; (b) 50 % filling.

Figure 4.26(a) is a tomogram reconstructed form soundness of 0% grout filling of polyethylene sheath PC model while Figure 4.26(b) is soundness of 50% grout filling of polyethylene sheath PC model, both are from 2 sided measurement travel time technique. From the visualization of Figure 4.26(a) and (b), there are not much difference between soundness of 0% grout filling and 50 grout filling of polyethylene sheath PC model in 2 sided measurements travel time technique. However, both tomograms are able to identify the presence of void on the centre have less soundness if compared to the whole cross section. With four-sided measurements, the tomogram Figure 4.27(a) is a soundness of polyethylene sheath PC model with 0% grout filling and it is able to identify the existence of the void at the centre with soundness at 91%. However, the tomogram Figure 4.27(b) which is from soundness of 50% grout filling has soundness of 95% at the centre.

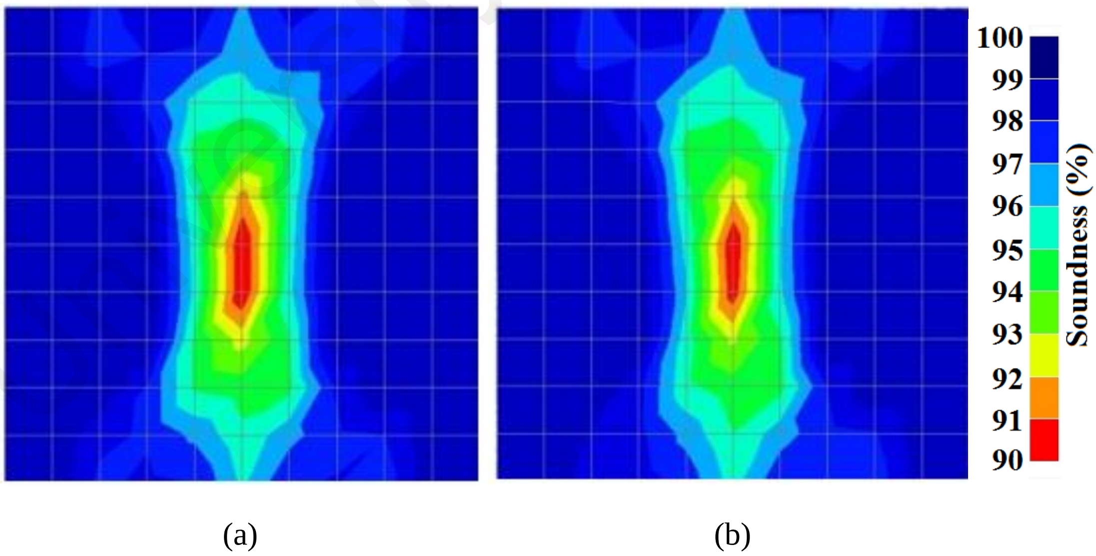

Figure 4.26: Soundness of tomogram case Figure 3.9 with polyethylene sheath PC model that tested by 2 sided travel time technique :(a) 0 % grout filling; (b) 50 % filling.

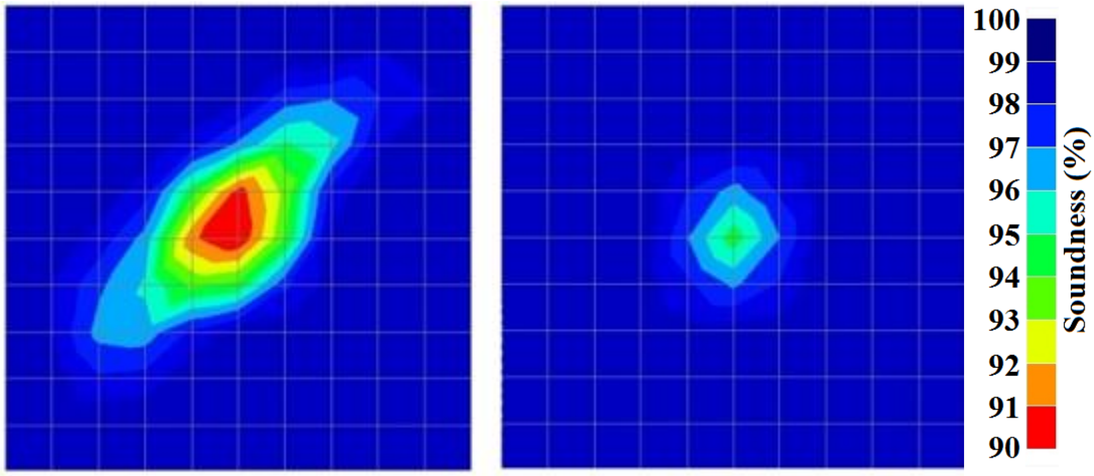

(a) (b)

Figure 4.27: Soundness of tomogram case Figure 3.9 with polyethylene sheath PC model that tested by 4 sided travel time technique: (a) 0 % grout filling; (b) 50 % filling.

4.4.2 Amplitude technique

Figure 4.28(a)is a tomogram of soundness of 0% grout filling aluminium sheath PC model while Figure 4.28(b) is a tomogram of soundness of 50% grout filling aluminium sheath PC model, both by 2 sided measurements amplitude technique. Figure 4.28(a) displays that the centre of tomogram has worst condition than its left and right side. However, the centre of 50% grout filling at Figure 4.28(b) has sounder condition than Figure 4.28(a) because of the green colour with soundness of 82% in the centre is bigger than that in Figure 4.28(a). Figure 4.29(a) is a tomogram for soundness of 0% grout filling of aluminium sheath PC model with four-sided amplitude measurements while Figure 4.29(b) is a tomogram for soundness of 50% grout filling of aluminium sheath PC model by four-sided amplitude. The four-sided amplitude measurements are able to detect void with soundness of 70% and with circle in shape. Nonetheless, the tomogram soundness of 50% grout filling in Figure 4.29(b) has a smaller red area than Figure 4.29(a).

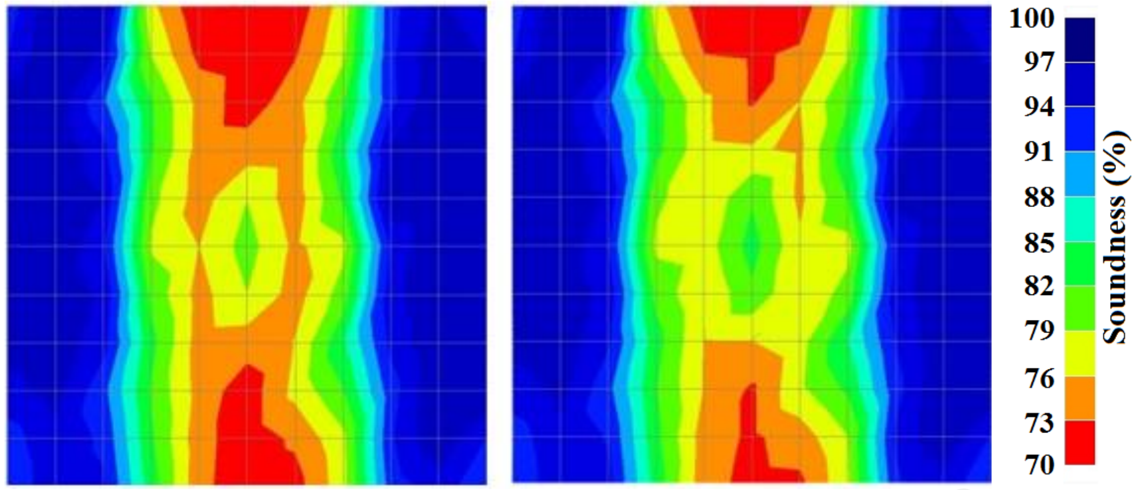

(a) (b)

Figure 4.28: Soundness of tomogram case Figure 3.9 with aluminum sheath PC model that tested by 2 sided amplitude technique:(a) 0 % grout filling; (b) 50 % filling.

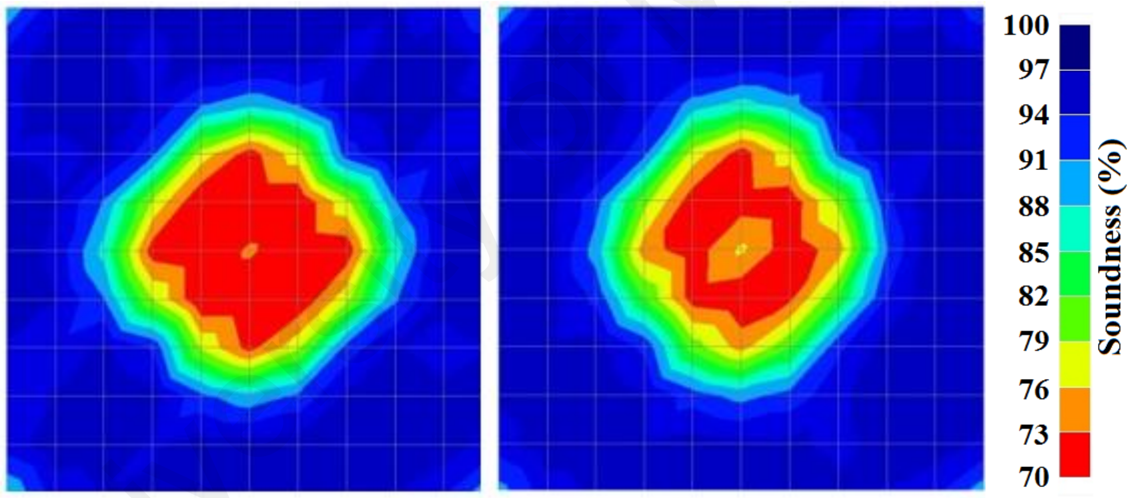

(a) (b)

Figure 4.29: Soundness of tomogram case Figure 3.9 with aluminum sheath PC model that tested by 4 sided amplitude technique:(a) 0 % grout filling; (b) 50 % filling.

Figure 4.30(a) is a tomogram of soundness of 0% grout filling aluminium sheath PC model with steel tendon while Figure 4.30(b) is a tomogram of soundness of 50% grout filling aluminium sheath PC model with steel tendon, both are from 4 sided measurements amplitude technique. With the incorporation of steel tendon into aluminium sheath PC model, although the soundness is still able to indicate the presence of honeycomb but the soundness value has increased at the centre of tomogram if compared Figure 4.30(a) with Figure 4.29(a). Besides that, the centre of 4 sided amplitude measurements of 50% grout filling PC model with a steel tendon in Figure 4.30(b) have soundness more than 50% grout filling PC model in Figure 4.30(b) because of the red colour with soundness less than 73% in Figure 4.30(b) is less than in Figure 4.29(b).

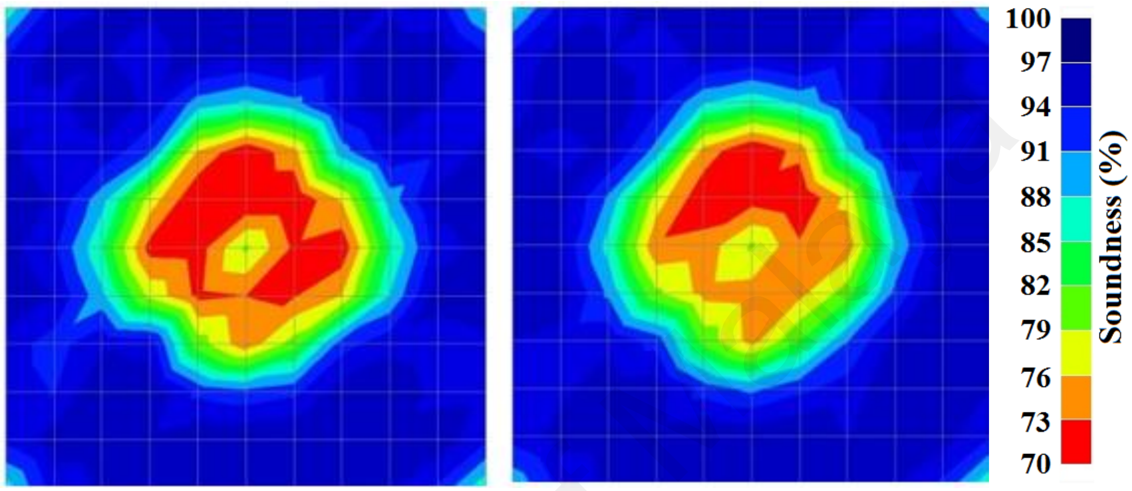

(a) (b)

Figure 4.30: Soundness of tomogram case Figure 3.10 for aluminium sheath PC model with steel tendon that tested by 4 sided amplitude technique:(a) 0 % grout filling; (b) 50 % filling.

Figure 4.31(a) is a tomogram of soundness of 0% grout filling polyethylene sheath PC model while Figure 4.28(b) is a tomogram of soundness of 50% grout filling polyethylene sheath PC model, both by 2 sided measurements amplitude technique. The soundness of 50% grout filling in Figure 4.31(b) is higher than 0% grout filling in Figure 4.31(a) as the orange and red colours which with soundness lower than 76% in Figure 4.31(a) is bigger than tomogram in Figure 4.31(b). For two-sided AT, the sensitivity of the amplitude technique towards polyethylene is lower than aluminium because the shape of the flaw in Figure 4.28 is bigger than in Figure 4.31. Figure 4.32(a) is a tomogram for soundness of 0% grout filling of polyethylene sheath PC model by four-sided amplitude measurements while Figure 4.29(b) is a tomogram for soundness of 50% grout filling of polyethylene sheath PC model by four-sided amplitude. Both the soundness of two-sided and four-sided measurements for amplitude technique are able to detect the presents of the void.

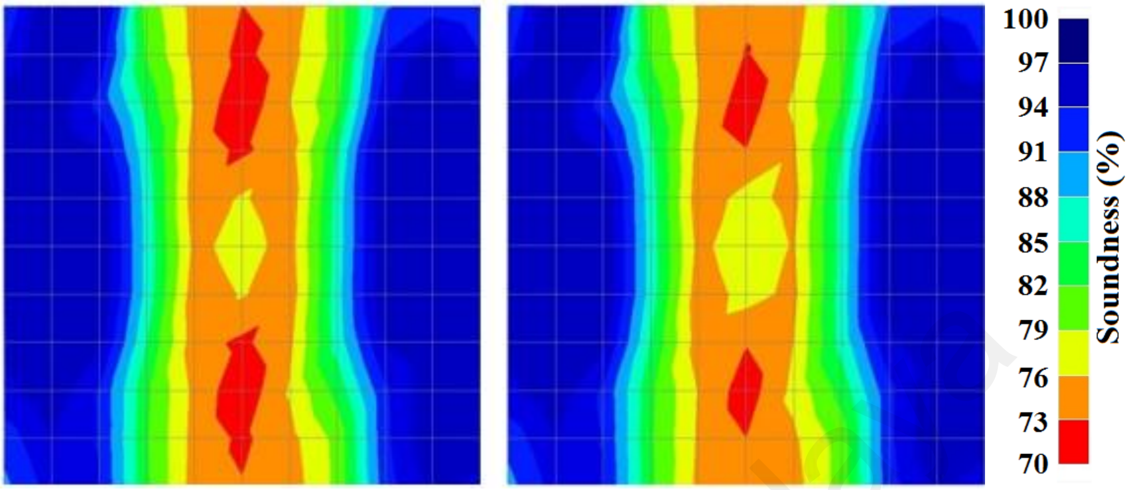

(a) (b)

Figure 4.31: Soundness of tomogram case Figure 3.9 with polyethylene sheath PC model that tested by 2 sided amplitude technique :(a) 0 % grout filling; (b) 50 % filling.

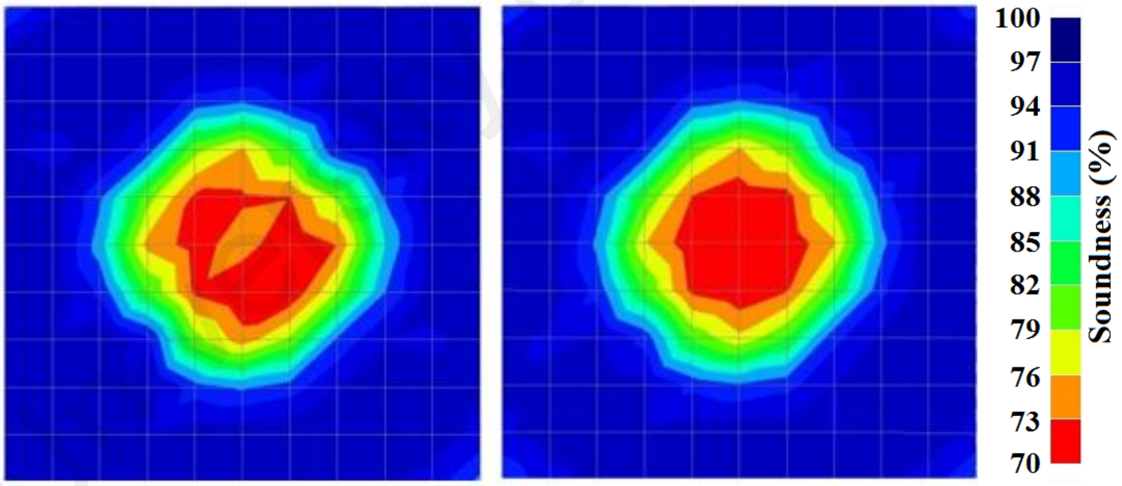

(a) (b)

Figure 4.32: Soundness of tomogram case Figure 3.9 with polyethylene sheath PC model that tested by 4 sided amplitude technique: (a) 0 % grout filling; (b) 50 % filling.

Figure 4.33(a) is a tomogram of soundness of 0% grout filling polyethylene sheath PC model with steel tendon while Figure 4.30(b) is a tomogram of soundness of 50% grout filling polyethylene sheath PC model with steel tendon, both are from 4 sided measurements amplitude technique. With the incorporation of steel tendon into aluminium sheath PC model, the area red colour with soundness lower than 73% in Figure 4.33 seems to be smaller than the area of red colour that display in Figure 4.32. Thus, with the adding of adding of steel tendon into the PC model, both aluminium and polyethylene PC model will show less sensitive on soundness of four-sided measurements AT.

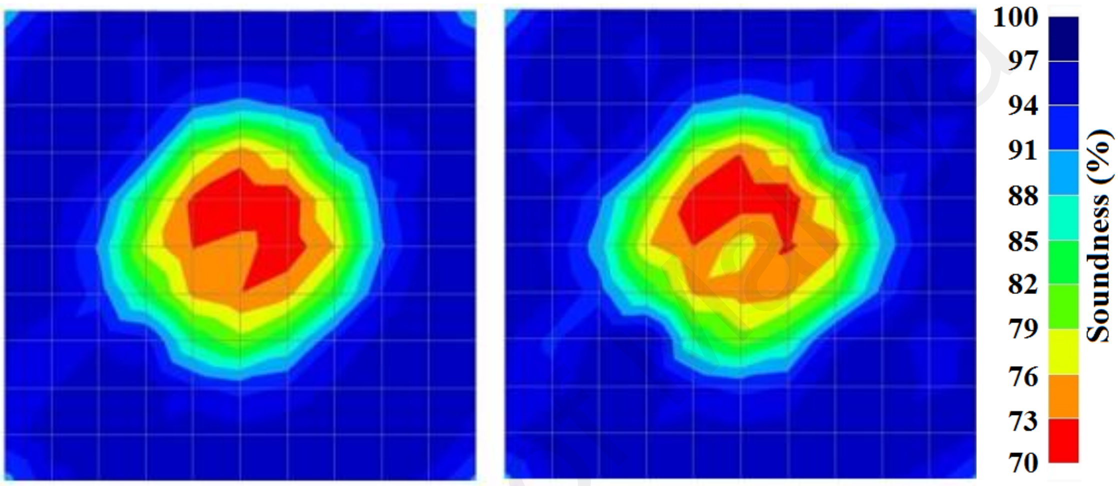

(a) (b)

Figure 4.33: Soundness of tomogram case Figure 3.10 for polyethylene sheath PC model with steel tendon that tested by 4 sided amplitude technique:(a) 0 % grout filling; (b) 50 % filling.

4.4.3 Frequency technique

Figure 4.34(a) is a tomogram of soundness of 0% grout filling aluminium sheath PC model with steel tendon while Figure 4.34(b) is a tomogram of soundness of 50% grout filling aluminium sheath PC model with steel tendon, both are from 2 sided measurements frequency technique. The centre of Figure 4.34(a) shows orange colour which is soundness in between 55 %. While for 50% grout filling, the centre of 2 sided FT have soundness of 70%. With the four-sided frequency measurements, the tomogram of Figure

4.35 is from plotting the soundness of 0% grout filling of aluminium sheath PC model with steel tendon. The visualization of tomogram Figure 4.35(a) is better than 2 sided measurements. Similarly to soundness of 50% grout filling from four-sided frequency measurement, the visualization and accuracy of tomogram result had improved significantly. Figure 4.36(a) is a tomogram outcome from soundness of 0% grout filling polyethylene sheath PC model with steel tendon by 4 sided frequency measurements. The soundness at the centre of Figure 4.36(a) has reduced if compared to Figure 4.35(a) because of polyethylene sheath. Likewise the Figure 4.46(b) is a soundness of 50% grout filling and the soundness at the centre is more than that in centre of Figure 4.36(a) but less than that in the centre of Figure 4.35(b).

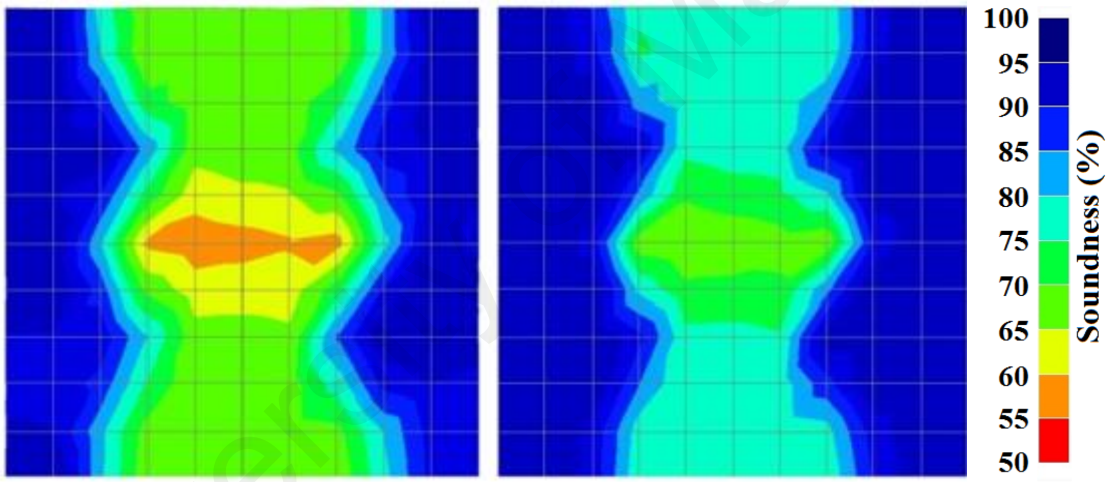

(a) (b)

Figure 4.34: Soundness of tomogram case Figure 3.10 for aluminium sheath PC model with steel tendon that tested by 2 sided frequency technique:(a) 0 % grout filling; (b) 50 % filling.

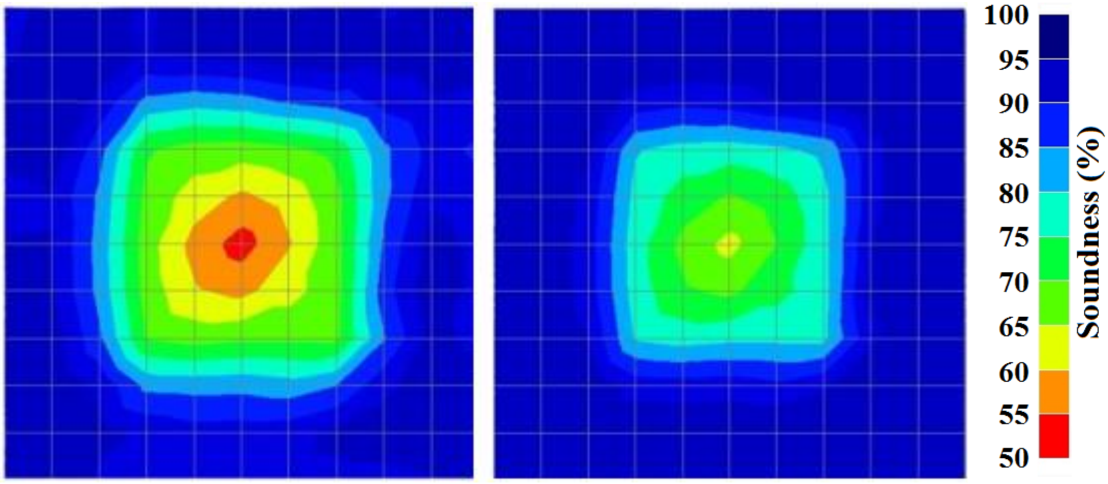

(a) (b)

Figure 4.35: Soundness of tomogram case Figure 3.10 for aluminium sheath PC model with steel tendon that tested by 4 sided frequency technique:(a) 0 % grout filling; (b) 50 % filling.

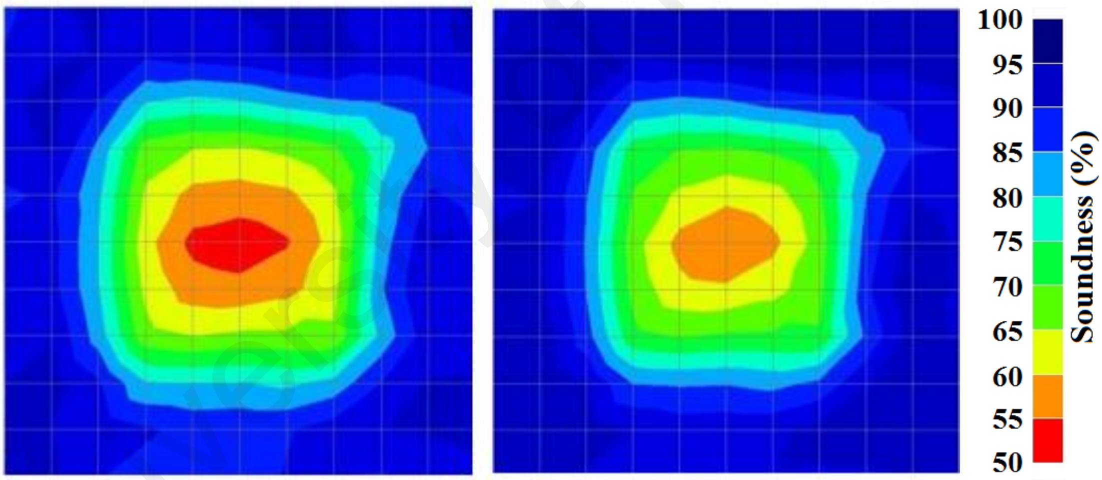

(a) (b)

Figure 4.36: Soundness of tomogram case Figure 3.10 for polyethylene sheath PC model with steel tendon that tested by 4 sided frequency technique: (a) 0 % grout filling; (b) 50 % filling.

4.4.4 Q-value Technique

Figure 4.37(a) shows a tomogram of soundness of 0% grout filling aluminium sheath PC model while Figure 4.37(b) with 50% soundness of grout filling aluminium sheath PC model, both by 4 sided measurements Q-value technique. The soundness indicates the presence of honeycomb by showing that the centre of tomogram show red colour with soundness lower than 73% which is less sound than the wider angle. In addition, the soundness at the centre for 50% grout filling as in Figure 4.37(b) is higher than 0% grout filling as in Figure 4.37(a). By incorporated of steel tendon into the aluminium sheath PC model, the soundness of 0% grout filling by 4 sided Q-value at the centre of tomogram Figure 4.38(a) have increased if compared to only aluminium sheath PC model in Figure 4.37(a). This is because the red colour area in Figure 4.38(a) is smaller than in Figure 4.37(a). Similarly, to soundness of 50% grout filling of aluminium sheath PC model with steel tendon as displays in Figure 4.38(b), the green colour with soundness of 82% is shown at the centre of tomogram and it is sounder than the centre of Figure 4.38(a).

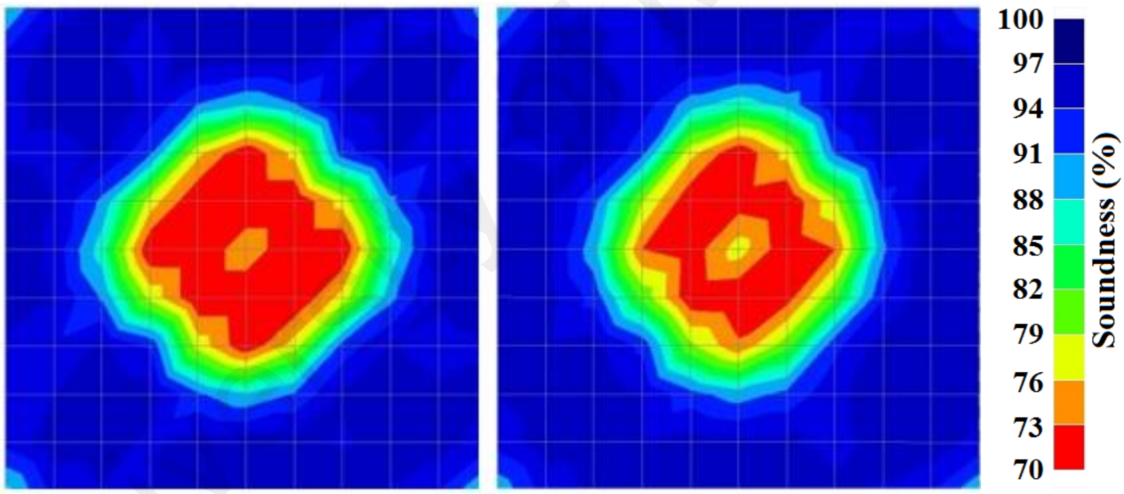

(a) (b)

Figure 4.37: Soundness of tomogram case Figure 3.9 with aluminum sheath PC model that tested by 4 sided Q-value technique:(a) 0 % grout filling; (b) 50 % filling.

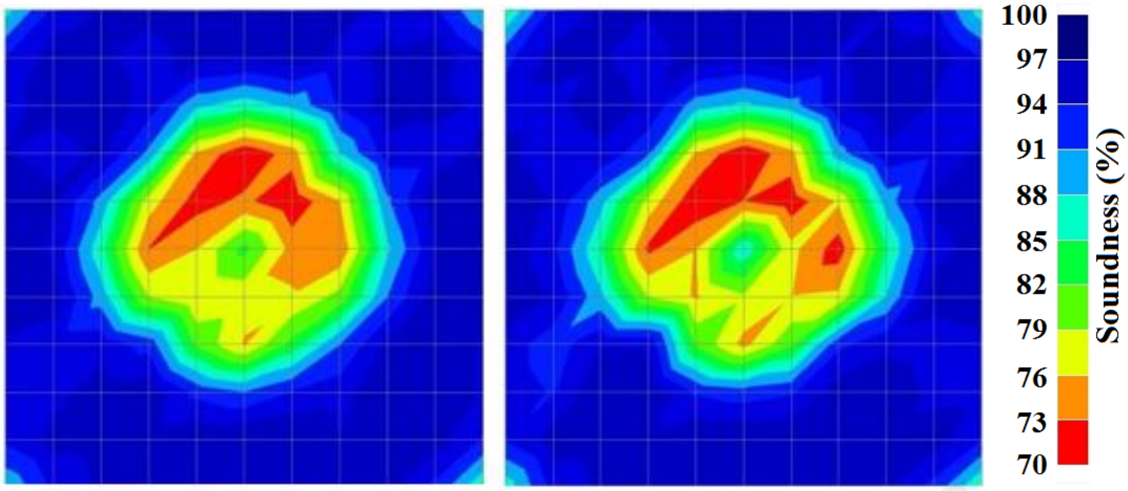

(a) (b)

Figure 4.38: Soundness of tomogram case Figure 3.10 for aluminium sheath PC model with steel tendon that tested by 4 sided Q-value technique:(a) 0 % grout filling; (b) 50 % filling.

Figure 4.39(a) is a tomogram of soundness for 0% grout filling polyethylene sheath PC model while Figure 4.40(b) is a tomogram of soundness of 50% grout filling polyethylene sheath PC model, both are from 2 sided measurements Q-value technique. The soundness of Figure 4.39(a) display yellow colour with soundness of between 76% at the centre and there is red colour with soundness less than 73% at the top and bottom of tomogram. The tomogram Figure 4.39(b) shows the higher soundness at the centre if compared to Figure 4.39(a) because of 50% grout filling inside polyethylene sheath PC model. Similar for 50% grout filling, there is red colour with soundness lower than 73% shown on the top and bottom of tomogram in figure 4.39(b) but are smaller than Figure 4.39(a). Figure 4.40(a) is a tomogram of soundness of 0% grout filling polyethylene sheath PC model while Figure 4.40(b) is a tomogram of soundness of 50% grout filling polyethylene sheath PC model, both are from 4 sided measurements Q-value technique. Both of the tomogram Figure 4.40(a) and Figure 4.40(b) has better visualization than two-sided measurement as in Figure 4.39(b) where the location and size of void are more accurate. In general, Figure

4.40(a) has bigger red colour with soundness less than 73% at the centre if compared to Figure 4.40(b) because of deference in percentage of grouting.

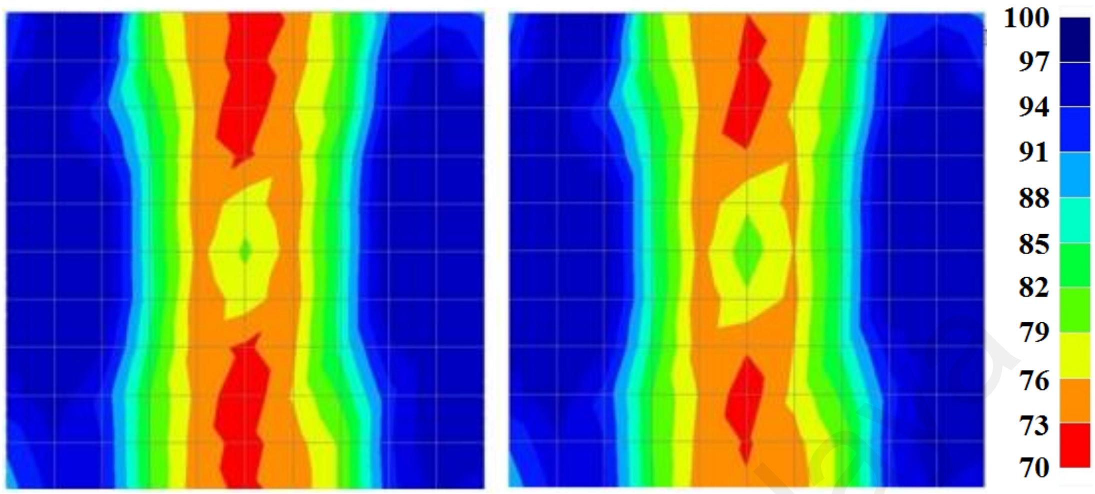

(a) (b)

Figure 4.39: Soundness of tomogram case Figure 3.9 with polyethylene sheath PC model that tested by 2 sided Q-value technique :(a) 0 % grout filling; (b) 50 % filling.

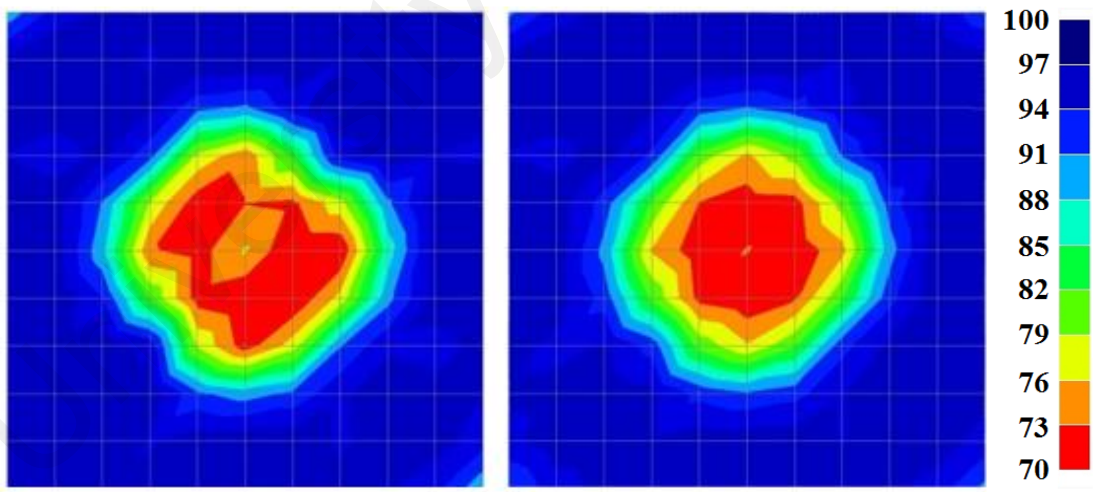

(a) (b)

Figure 4.40: Soundness of tomogram case Figure 3.9 with polyethylene sheath PC model that tested by 4 sided Q-value technique: (a) 0 % grout filling; (b) 50 % filling.

Figure 4.41(a) shows a tomogram of soundness for 0% grout filling polyethylene sheath PC model with steel tendon while Figure 4.41(b) shows a 50% soundness grout filling polyethylene sheath PC model with steel tendon, both are from 2 sided measurements Q-value technique. The centre of tomogram Figure 4.41(a) and Figure 4.41(b) have blue colour with soundness within 88% and it can be a hint for existence of steel tendon inside the structure. Besides that, the green colour with soundness within 82% at the centre of tomogram Figure 4.41(a) and Figure 4.41(b) show that the soundness has been dropped due to void. Furthermore, the blue colour spot at the centre of Figure 4.41(b) is bigger than that in Figure 4.41(a) because of the grout filling at Figure 4.41(b) is 50% while it is 0% at Figure 4.41(a).Figure 4.42(a)is a tomogram of soundness for 0% grout filling polyethylene sheath PC model with steel tendon while Figure 4.42(b) is a tomogram of soundness of 50% grout filling polyethylene sheath PC model with steel tendon, both from 4 sided measurements Q-value technique. Both the centre of tomogram Figure 4.42(a) and Figure 4.42(b) are able to indicate the presence of void and result also show that the condition of Figure 4.42(a) is critical than Figure 4.42(b). In addition, with the incorporation of a steel tendon into polyethylene sheath PC model, the soundness at the centre of Figure 4.42(a) is higher than Figure 4.40(a) in which Figure 4.40(a) is a polyethylene sheath PC model without steel tendon. Similarly, on the 50% grout filling of polyethylene sheath PC model where the soundness at the centre of Figure 4.42(b) is higher than the centre of Figure 4.40(b) because of Figure 4.40(b) is a 50% grout filling of polyethylene PC model.

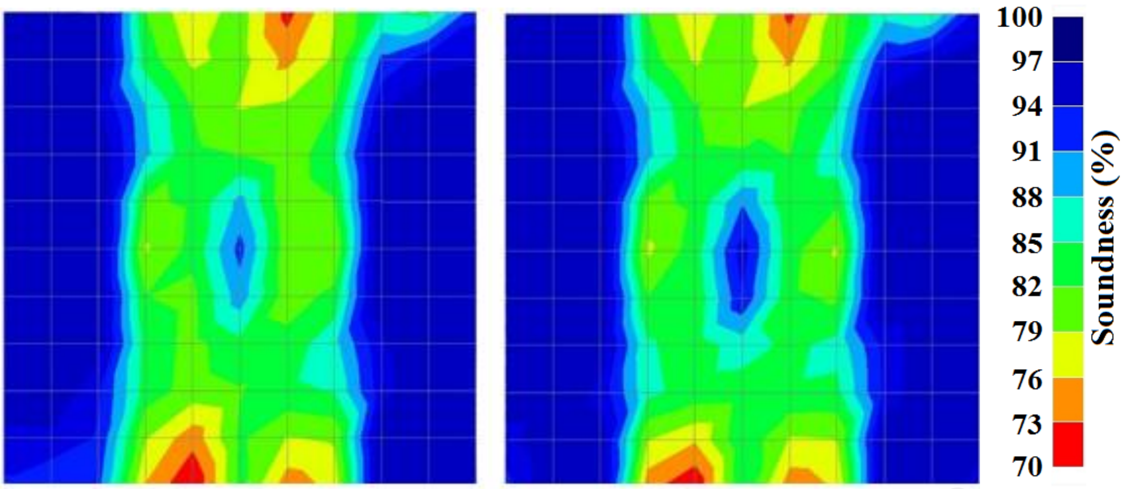

(a) (b)

Figure 4.41: Soundness of tomogram case Figure 3.10 for polyethylene sheath PC model with steel tendon that tested by 2 sided Q-value technique: (a) 0 % grout filling; (b) 50 % filling.

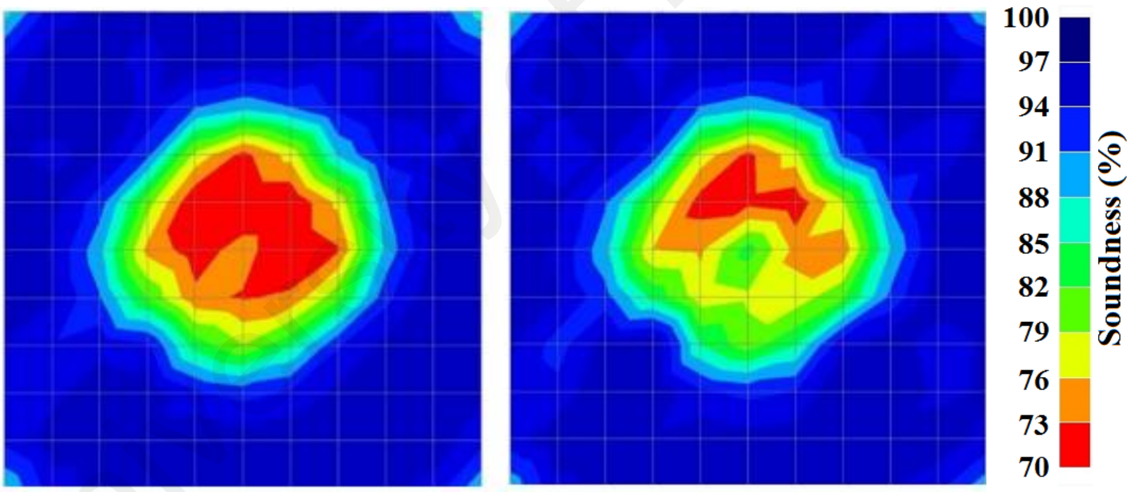

(a) (b)

Figure 4.42: Soundness of tomogram case Figure 3.10 for polyethylene sheath PC model with steel tendon that tested by 4 sided Q-value technique :(a) 0 % grout filling; (b) 50 % filling.

4.4.5 Frequency

Figure 4.43 is a tomogram plotted by compared sound condition of 0% grout filling with 100% grout filling of aluminium PC specimen from 2 sided travel time measurements tomogram. The Figure 4.43(a) is a tomogram that reconstructed from laboratory of 25 kHz while Figure 4.43(b) is a tomogram that reconstructed from laboratory of 18 kHz. The Figure 4.43(a) is able to display the red colour with soundness less than 91% to indicate the presence of void. Generally, the centre of tomogram Figure 4.43(a) is less than the left and right side and this is same as Figure 4.43(b). However, the soundness of tomogram at the centre of Figure 4.43(b) is less obvious in void detection if compared to 4.43(a). The results were verified the statement that suggested by Aggelis et al. (2011) in which the visualization of tomogram that reconstructed from the higher frequency trigger source produces higher quality tomograms. However, it depends on the frequency produced by the impact object and the frequency should be fall in the range of capability of sensors and data acquisition device to detect the waveform.

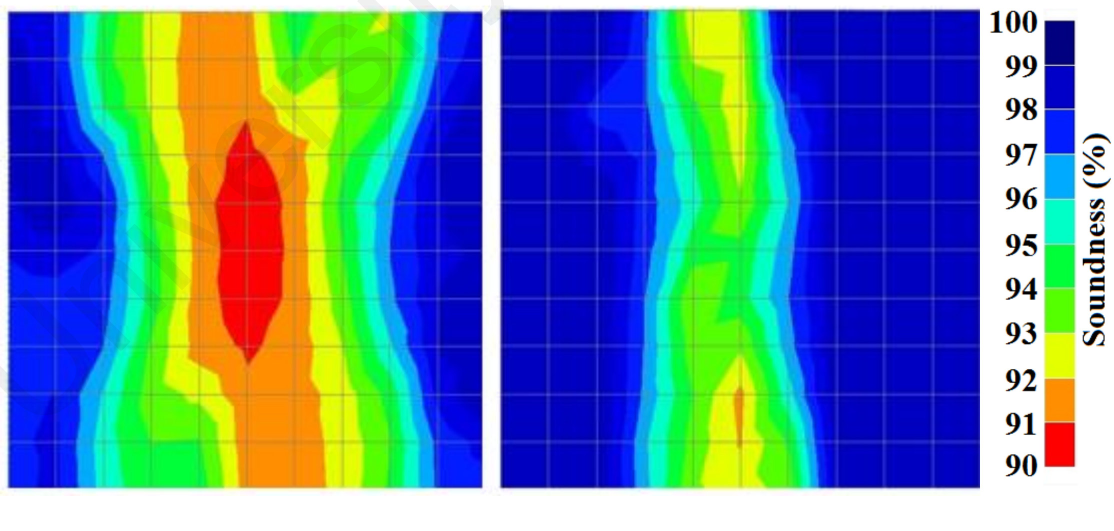

(a) (b)

Figure 4.43: Soundness of case Figure 3.14, PC specimen with 0% grout filling polyethylene tendon sheath plotted by 2 sided AT and frequency of:(a) 25 kHz;(b)18kHz.

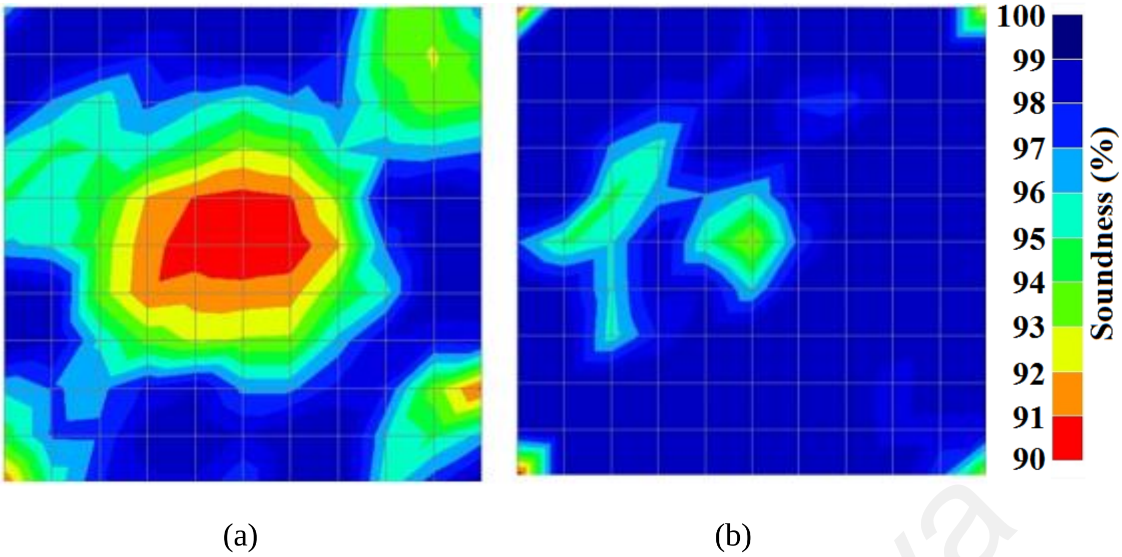

Figure 4.44: Soundness of case Figure 3.14, aluminum sheath PC specimen measuring by 18 kHz frequency laboratory 4 sided travel time technique:(a) 0 % grout filling; (b) 50 % filling.

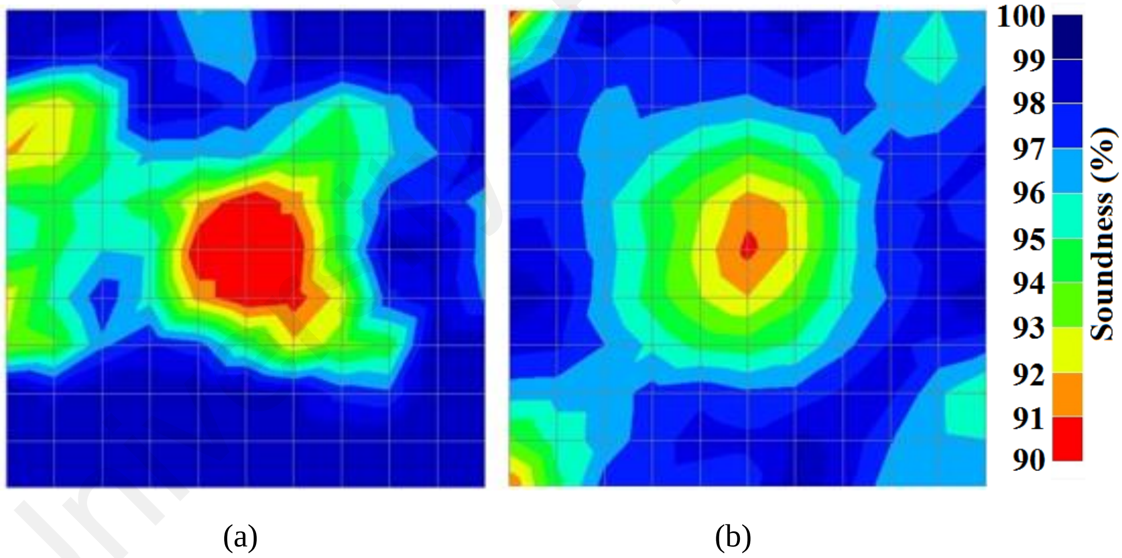

Figure 4.45: Soundness of tomogram case Figure 3.14, aluminum sheath PC specimen plotted by 25 kHz frequency laboratory 4 sided travel time technique:(a) 0 % grout filling; (b) 50 % filling.

4.4.6 Soundness

Soundness is generated from comparing the drop of test condition with sound condition. Figure 4.46(a) is a tomogram plotted by soundness of 0% grout filling of aluminium sheath PC specimen while Figure 4.46(b) is soundness of 50% grout filling of aluminium sheath PC specimen. Both are based on 4 sided AT that reconstructed from raw data obtained from 25 kHz source laboratory. The tomogram Figure 4.46(a) is able to indicate the presence of the void at the centre of tomogram by showing there is drop of soundness to 84% by showing orange colour. The tomogram in Figure 4.46(b) show that the centre of tomogram has lowest soundness among the cross section which is soundness of 88% and it is in green colour. However, the soundness at the centre of Figure 4.46(b) is more than figure 4.45(a) because of 50% grout filling.

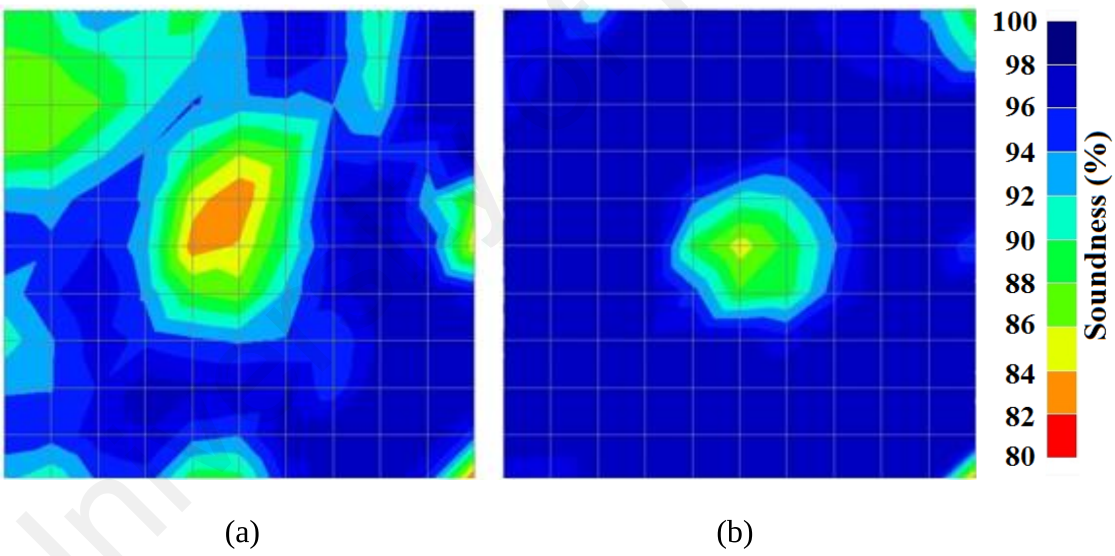

Figure 4.46: Soundness of tomogram case Figure 3.14, aluminum sheath PC specimen plotted by 25 kHz frequency laboratory 4 sided amplitude technique:(a) 0 % grout filling; (b) 50 % filling.

Figure 4.47(a) is a tomogram measuring by soundness of 0% grout filling of aluminium sheath PC specimen while Figure 4.47(b) is soundness of 50% grout filling of aluminium sheath PC specimen. Both are measuring by 2 sided Q-value tomography which raw data were obtained from experiment of 25 kHz source. The tomogram in Figure 4.47(a) show that the centre is with the poor by displays red colour with soundness less than 59.5 %. The Figure 4.47(b) shows that the centre has yellow and green colour which with soundness of 68.5%. Besides, the Figure 4.47(a) hints that there is a void in 50% grout filling of aluminium sheath PC specimen. Figure 4.48(a) is a tomogram measuring by soundness of 0% grout filling of aluminium sheath PC specimen while Figure 4.48(b) is soundness of 50% grout filling of aluminium sheath PC specimen. Both are measuring by 4 sided Q-value tomography reconstructed by raw data that obtained from experiment of 25 kHz source. The centre of Figure 4.48(a) is able to show the presence of void at 0% grout filling of aluminium sheath PC specimen and the visualization is better and more accurate than in Figure 4.47(a). The tomogram in Figure 4.48(b) is able to indicate the presence of void at 50% grout filling with green colour and with soundness of 73%.

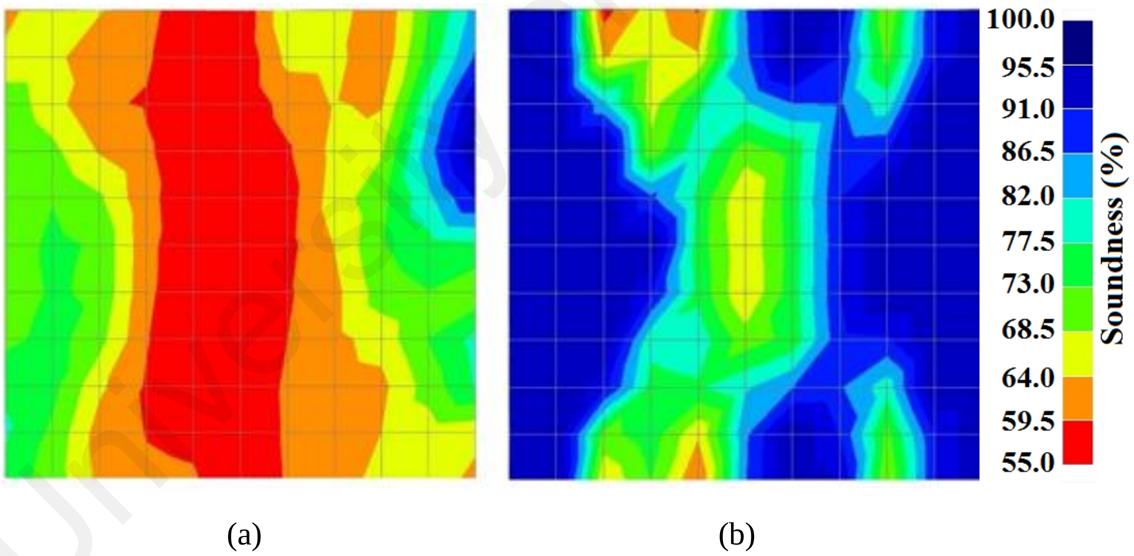

Figure 4.47: Soundness of tomogram case Figure 3.14, aluminum sheath PC specimen measuring by 25 kHz frequency laboratory 2 sided Q-value technique:(a) 0 % grout filling; (b) 50 % filling.

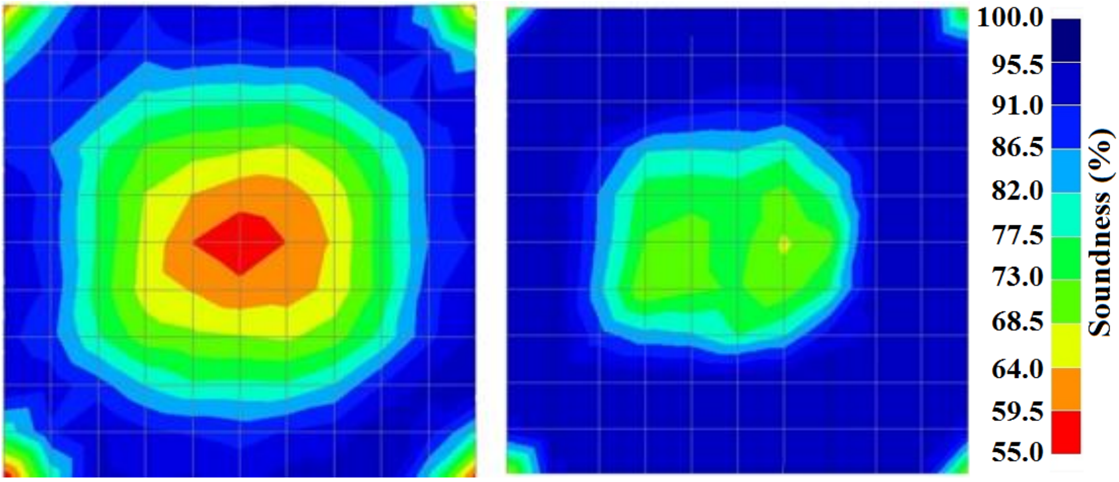

(a) (b)

Figure 4.48: Soundness of tomogram case Figure 3.14, aluminum sheath PC specimen plotted by 25 kHz frequency laboratory 4 sided Q-value technique:(a) 0 % grout filling; (b) 50 % filling.

Figure 4.49 shows average soundness for partially grouted of aluminium sheath PC model with steel tendon by two-sided and four-sided measurements of four types of tomography technique which are travel time, amplitude, frequency and Q-value. From the results, the travel time technique is the less sensitive among the four techniques. For 0% grout filling of aluminium sheath PC model with steel tendon, the 2 sided measurements of travel time have average soundness of 95.17%, 70.13% for amplitude, 60.52% for frequency and 81.9% for Q-value technique. For 0% grout filling of aluminium sheath PC model with steel tendons of the 4 sided measurements, the travel time has average soundness of 94.2%, 74.17% for amplitude, 63.88% for frequency and 79.81% for Q-value technique. For 50% grout filling of aluminium sheath PC model with steel tendon by the 2 sided measurements, the travel time has average soundness of 98.18%, 73.42% for amplitude, 65.45% for frequency and 85.13% for Q-value technique. The last but not least, for 50% grout filling of aluminium sheath PC model with steel tendon by the 4 sided measurements, the travel time has average soundness of 98.62%, 79.11% for amplitude, 77.62% for frequency and 83.94% for Q-value technique.

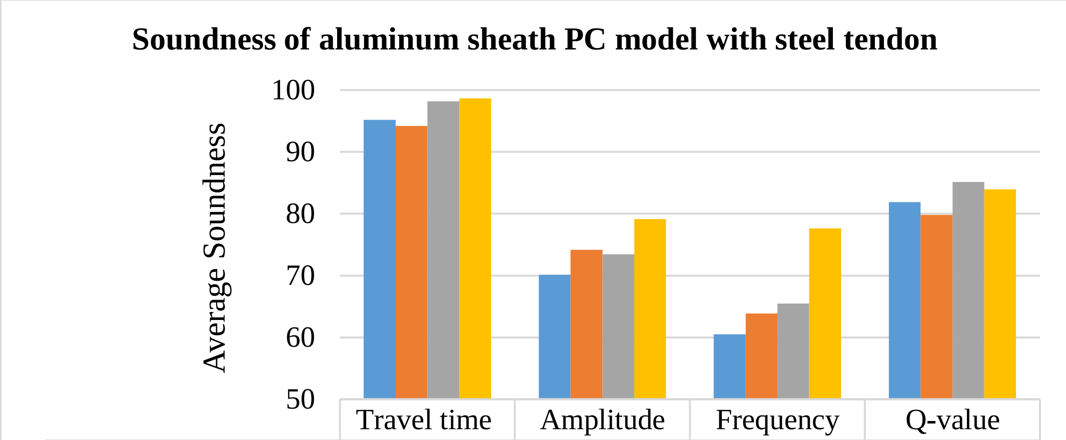

	Travel time	Amplitude	Frequency	Q-value
0% filling & 2-sided	95.171	70.137	60.52	81.904
0% filling & 4-sided	94.208	74.176	63.882	79.815
50% filling & 2-sided	98.185	73.421	65.453	85.135
50% filling & 4-sided	98.623	79.115	77.624	83.941

Figure 4.49: Histogram of average soundness for partially grouted aluminum sheath PC model with steel tendon.

Figure 4.50 shows average soundness for partially grouted of polyethylene sheath PC model with steel tendon by two-sided and four-sided measurements of four types of tomography technique which are travel time, amplitude, frequency and Q-value. From the results, the travel time technique is the less sensitive among the four techniques. For 0% grout filling of polyethylene sheath PC model with steel tendon, the 2 sided measurements of travel time have average soundness of 97.26%, 73.2% for amplitude, 62.4% for frequency and 85.86% for Q-value technique. For 0% grout filling of polyethylene sheath PC model with steel tendon by the 4 sided measurements, the travel time has average soundness of 95.21%, 78.61% for amplitude, 56.81% for frequency and 80.16% for Q-value technique. For 50% grout filling of polyethylene sheath PC model with steel tendon by the 2 sided measurements, the travel time has average soundness of 97.19%, 80.9% for amplitude, 66.93% for frequency and 87.53% for Q-value technique. The last but not the least, for 50% grout filling of polyethylene sheath PC model with steel tendon by the 4 sided measurements, the travel time has average soundness of 98.43%, 81.24% for amplitude, 68.49% for frequency and 85.6% for Q-value technique.

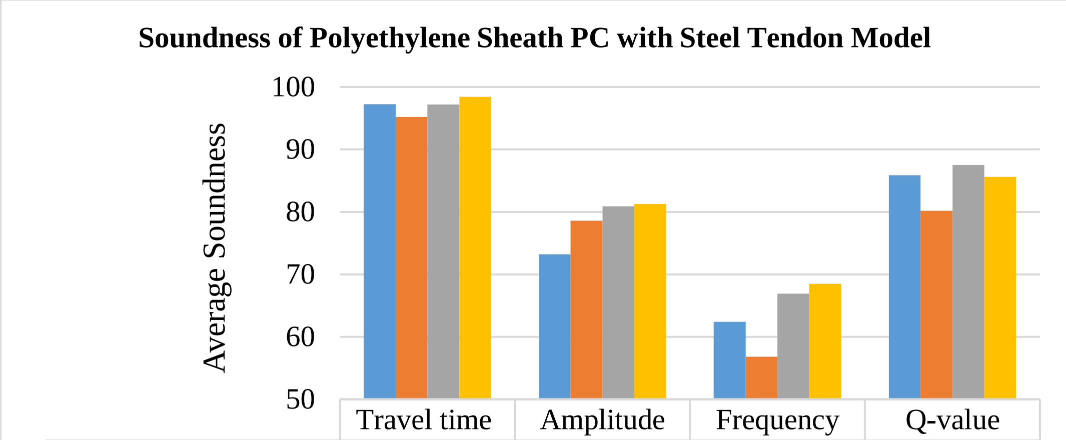

	Travel time	Amplitude	Frequency	Q-value
0% filling & 2-sided	97.265	73.204	62.403	85.869
0% filling & 4-sided	95.219	78.614	56.814	80.162
50% filling & 2-sided	97.192	80.908	66.936	87.531
50% filling & 4-sided	98.431	81.247	68.499	85.606

Figure 4.50: Histogram of average soundness for partially grouted polyethylene sheath PC with steel tendon model.

Figure 4.51 presents average soundness for partially grouted of aluminium sheath PC model by two-sided and four-sided measurements of four types of tomography technique which are travel time, amplitude, frequency and Q-value. The tomograms were reconstructed from raw data that obtained from laboratory at source frequency of 18 kHz.

From the results, the travel time technique is the less sensitive among the four techniques. For 0% grout filling of aluminium sheath PC model, the 2 sided measurements of travel time have average soundness of 97.1%, 81.41% for amplitude, 75.21% for frequency and 78.61% for Q-value technique. For 0% grout filling of aluminium sheath PC model of the 4 sided measurements, the travel time has average soundness of 93.26%, 86.82% for amplitude, 77.16% for frequency and 80.2% for Q-value technique. For 50% grout filling of aluminium sheath PC model of the 2 sided measurements, the travel time has average soundness of 96.63%, 88.13% for amplitude, 81.59% for frequency and 87.21% for Q-value technique. The last but not least, for 50% grout filling of aluminium sheath PC model by the 4 sided measurements, the travel time has average soundness of 98.42%, 89.2% for amplitude, 83.06% for frequency and 88.07% for Q-value technique.

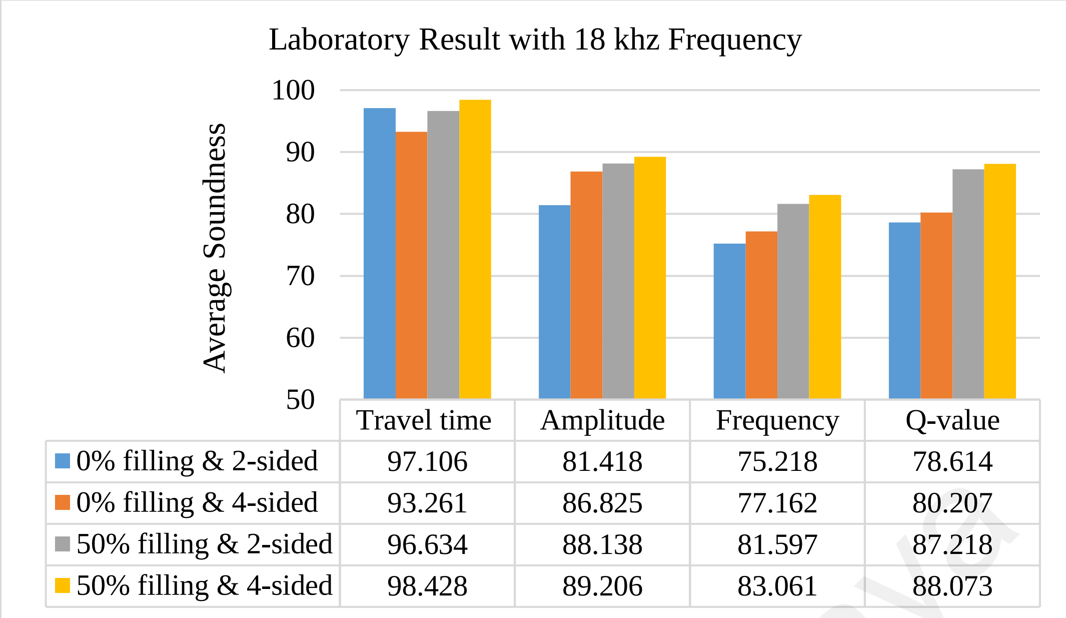

	Travel time	Amplitude	Frequency	Q-value
0% filling & 2-sided	97.106	81.418	75.218	78.614
0% filling & 4-sided	93.261	86.825	77.162	80.207
50% filling & 2-sided	96.634	88.138	81.597	87.218
50% filling & 4-sided	98.428	89.206	83.061	88.073

Figure 4.51: Histogram of average soundness for partially grouted aluminum sheath PC specimen by 18 kHz laboratory raw data.

Figure 4.52 presents average soundness for partially grouted of aluminium sheath PC model by two-sided and four-sided measurements of four types of tomography technique which are travel time, amplitude, frequency and Q-value. The tomograms were reconstructed from raw data that obtained from laboratory at source frequency of 25 kHz.

From the results, the travel time technique is the less sensitive among the four techniques. For 0% grout filling of aluminium sheath PC model, the 2 sided measurements of travel time have average soundness of 93.81%, 76.73% for amplitude, 68.48% for frequency and 72.61% for Q-value technique. For 0% grout filling of aluminium sheath PC model by the 4 sided measurements, the travel time has average soundness of 90.97%, 84.68% for amplitude, 71.85% for frequency and 76.43% for Q-value technique. For 50% grout filling of aluminium sheath PC model of the 2 sided measurements, the travel time has average soundness of 95.04%, 85.69% for amplitude, 69.02% for frequency and 82.57% for Q-value technique. The last but not least, for 50% grout filling of aluminium sheath PC model by the sided measurements, the travel time has average soundness of 96.18%, 92.75% for amplitude, 74.31% for frequency and 87.54% for Q-value technique.

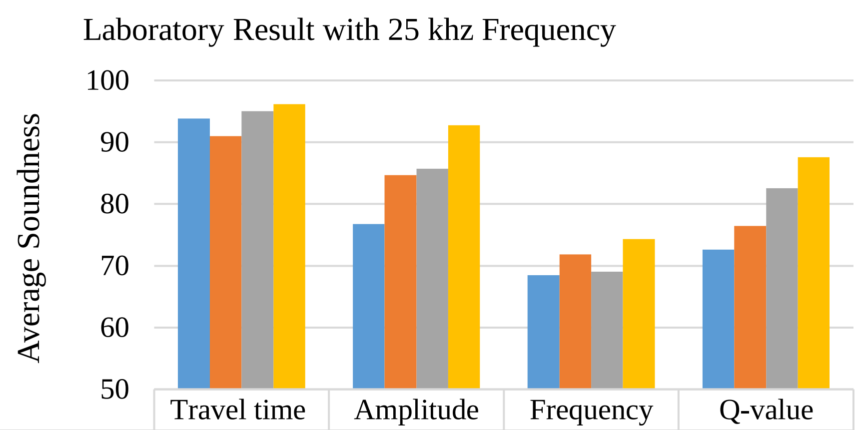

	Travel time	Amplitude	Frequency	Q-value
0% filling & 2-sided	93.815	76.732	68.489	72.613
0% filling & 4-sided	90.975	84.681	71.852	76.431
50% filling & 2-sided	95.043	85.698	69.021	82.574
50% filling & 4-sided	96.18	92.754	74.315	87.549

Figure 4.52: Histogram of average soundness for partially grouted aluminum sheath PC specimen by 25 kHz laboratory raw data.

Figure 4.49, 4.50, 4.51 and 4.52 show the sensitivity of the travel time technique in terms of soundness is less than the other three techniques because the delay caused in travel time was due to inhomogeneity of mediums, whereas the decrease of amplitude and frequency of wave are caused by the effect of scattering and absorption. The sensitivity for soundness of cross section that plotted from tomogram that reconstructed by the higher frequency produce have higher sensitivity than the tomogram that reconstructed from lower frequency. This is demonstrated by the average soundness for all cases at histogram Figure 4.52 is higher than average soundness in histogram Figure 4.50. This is because the attenuation coefficient of a material is found to increase with source frequency. Chaix JF et al. (2003) have found that waves from a high frequency source are bound to attenuate faster during their propagation from one point to another inside a medium.

4.5 Summary

Based on the research findings, it is possible to develop an algorithm to plot tomograms for some indicative elastic wave parameters in the case of inhomogeneous materials. At this point it seems to be necessary to discuss the significant aspects of the whole procedure. The general procedure seems to be considerably sensitive to the existence of a deteriorated material zone such as honeycomb rather than to a central void like PC duct. In addition, the level of sensitivity to the inhomogeneity size that can be determined is profoundly dependent on the sensor placement, as well as the tomography element size, particularly, for amplitude, frequency, and Q-value tomograms. In the present study, the distance between neighboring sensors was 88 mm, while the tomography cell sizes were 100 mm and 50 mm for tomograms with 25 and 100 elements, respectively. This can be the reason why there was no high resolution tomography for some tomograms with 25 elements; except in cases where the large dimension of the vertical deterioration zone (honeycomb) was much larger than the cell size.

It is noteworthy that in the experimental procedure the excitation frequency is one of the significant parameters. The excitation frequencies concern the wavelength/defect size ratio (λ/d). The applied frequency can result in a higher and lower ratio than unity which is in direct relation to the tomograms' resolutions and cell size.

The above aforementioned results imply that without changing the raw information (number of wave paths examined or number of sensors placed in the field) the results can be enhanced by selecting a smaller tomography mesh size. The results suggest that the cell could be set to a value smaller than the distance between adjacent sensors. However, it is not practical to always have smaller tomography mesh size and shorter adjacent sensor distance especially tomography task is conduct on a large structure. Although, a required time for computation on the tomography software is required to conduct the necessary iterations, it is minor compared to a better understanding of the internal situation of a structure, while it is negligible considering contemporary computational tools.

CHAPTER 5

CONCLUSIONS AND FUTURE RECOMMENDATIONS

5.1 Conclusions

Synthetic and real raw data have been used to explore the potential of developed optimised elastic wave tomography algorithm for NDT on concrete structures. Based on the study of four tomography techniques, namely travel time, amplitude, frequency and Q-value, the following conclusions can be drawn:

i. Ray tracing of TTT technique has to be introduced into the amplitude and FT technique in order to obtain the ray-path of the wave using the ray-tracing method. This is because the elastic wave experiences refraction and reflection and thus does not necessarily propagate only in a straight line. .

ii. The visualization by tomography reconstruction technique becomes better with increasing number of sensors. Also placement of sensors on all four sides of the concrete model improves the visualization significantly. But, it is almost impossible to conduct completely coverage tomography reconstruction technique on concrete structure, it is important to do the survey and properly design the location source and receiver depending on section geometry and environmental conditions to optimise the results.

iii. The type of material and defect would affect the visualization of tomograms based on the difference in acoustic impedance and elastic properties.

iv. The higher the source frequency produced higher quality tomograms due to the reduced wavelength which is more sensitive to inhomogeneity.

v. The amplitude of the elastic wave propagation in concrete undergoes a much greater change because of scattering and absorption compared to the delay in travel time due to the inhomogeneity of the medium. This phenomenon indicates the high sensitivity of elastic wave attenuation for potential adoption in the evaluation of soundness in concrete.

vi. Frequency technique is not able to provide a reliable flaw indication, but able to provide flaw indications if with the superimposed technique, which is by mere comparison with the results of measuring the sound concrete model.

vii. The ray coverage is poor at wider angles, this caused the section corners or surroundings of amplitude, frequency and Q-value tomograms present low soundness. Besides, in experiment the receiver sensors show that they tend to record reflected wave that arrived from adjacent.

viii. TTT is less sensitive among four types of tomography techniques. Thus, it is recommended to conduct other tomography techniques to compare, interpret and confirm the experimental results.

ix. The incorporation of steel tendon into PC model has no influence on the capability of proposed tomography techniques on void detection. Somehow, the sensitivity of the travel time technique is better than the PC model that without steel tendon.

x. It is important to conduct preliminary studies such as numerical simulations on target structure before conducting the actual NDT on concrete structure. This is because the numerical simulations are considered to be the early design stages of NDT to check whether the NDT technique is suitable to conduct to target structure.

5.2 Future recommendations

In order to improve the quality and reliability of the proposed tomography reconstruction techniques, the following recommendations are proposed:

i. In this research, the developed algorithm was limited for viewing 2 dimensional cross section. It is recommended to modify the programme algorithm so that it has a capability for analysis and reconstruct the 3 dimensional tomography.

ii. Non-uniform mesh can be introduced into programme algorithm so that the mesh around the defects to be refined in order to improve accuracy of tomography visualization.

iii. The implementation and relay points into cells can improve the ray tracing approach. The installation of relay points will reduce the mesh dependency in which it will cause inaccurate estimation of ray-path from ray tracing.

iv. The programme algorithm also can be modified for the mapping triangular cell so that the technique is not only limited to square shape structure.

v. The process for extracting the first travel time, first peak amplitude, and central frequency until analysing the result into mapping can be organised and compacted into one programme so that it is user friendly and save time. The software, namely Labview is found to be a good programming software and it is capable to do this.

REFERENCES

228, ACI Committee (1998). *Nondestructive Test Methods for evaluation of Concrete in Structures*, Report ACI 228.2R-98. American Concrete institute, Framington hills, MI.

ASTM C 476, Standard Specification for Grout Masonry, ASTM.

Aggelis, D. G. & Shiotani, T. (2007). Repair evaluation of concrete cracks using surface and through-transmission wave measurements. *Cement and Concrete Composites*, 29(9), 700-711.

Aggelis, D. G, Hadjiyiangou, S., Chai, H. K., Momoki, S. & Shiotani, T. (2011). Longitudinal waves for evaluation of large concrete blocks after repair. *NDT & E International*. 44(1): 61-66 (2011).

Aggelis, D. G., Tsimpris, N., Chai, H. K., Shiotani, T. & Kobayashi, Y. (2011). Numerical simulation of elastic wave propagation for visualization of defects. *Construction and Building Materials*, 25(4), 1503-1512.

Alexander, A. M., & Thornton, H. T., Jr. (1989).Ultrasonic Pitch-Catch and Pulse-Echo Measurements in Concrete. *Nondestructive Testing of Concrete*, H. S. Lew, ed., ACI SP-112, American Concrete Institute, Farmington Hills, Mich., Mar., pp. 21-40.

Alver, N., Tokai, M., Nakai, Y., & Ohtsu, M. (2007). Identification of imperfectly-grouted tendon-duct in Concrete by Sibie procedure, in Proceedings of the European NDT Days, pp. 9–14, *NDE for Safety*, Prague, Czech Republic, November 2007.

Alver, N. & Ohtsu, M. (2007).BEM analysis of dynamic behavior of concrete in impact-echo test.*Construction and Building Materia*ls, 21(3), 519–526.

Ansari, F. & Sture, S.(1992). Nondestructive Testing of Concrete Elements and Structures, *Proceedings of Sessions in ASCE Structures Congress*, San Antonio, Texas.

Arnevik, A. (n.d.). Introduction to Ground Penetrating Radar and its General Use Applied to Fault Investigation. Retrieved from http://people.uwec.edu/jolhm/desertsouthwest/Posters/ArikGPR.pdf

Berkovits, A. & Fang, D. (1995). Study of fatigue crack characteristics by acoustic emission. *Engineering Fracture Mechanics*, 51(3):401-409.

Best, A. I., Mccann, C., & Sothcott, J. (1994). The relationships between the velocities, attenuations, and petrophysical properties of reservoir sedimentary rocks. *Geophys.Prosp*, 42,151-178.

Bhatt, P., MacGinley, T. J. & Choo. B. S. (1990). R*einforced Concrete: design theory and examples*. *Yaylor & Francis*.

Bond, L. J., Kepler, W. F. & Frangopol, D. M. (2000). Improved assessment of mass concrete dams using acoustic travel time tomography. Part I – theory. *Construction and Building Materials*, 14(3), 133-146.

Bradfield, G. & Gatfield, E. (1964).Determining the Thickness ofConcrete Pavements by Mechanical Waves: Directed Beam Method. *Magazineof Concrete Research*, 16(46), 49-53.

Breysse, D., Klysz, G., Derobert, X., Sirieix, C. & Lataste, J. F. (2008). How to combine several non-destructive techniques for better assessment of concrete structures. *Cement and Concrete Research, 38*(2008), 783-792.

Buyukozturk, O. (1998). Imaging of concrete structures, *NDT & E International*, 31(4), 233–243.

Carino, N. J., Sansalone, M., & Hsu, N. N. (1986). Flaw Detection in Concrete by Frequency Spectrum Analysis of Impact-Echo Waveforms. *International Advances in Nondestructive Testing*, V. 12, W. J. McGonnagle, ed., Gordon & Breach Science Publishers, New York, pp. 117-146.

Chai, H. K., Aggelis, D. G., Momoki, S., Kobayashi, Y. & Shiotani, T. (2010). Single-side access tomography for evaluating interior defect of concrete. *Construction and Building Materials, Elsevier*, 24(12), 2411-2418.

Chai, H. K., Aggelis, D. G., Momoki, S., Kobayashi, Y. & Shiotani, T. (2011). Tomographic reconstruction for concrete using attenuation of ultrasound. *NDT & E International*, 44(2), 206–215.

Chaix, J.F., Garnier, V. & Corneloup, G. (2003). Concrete damage evolution analysis by backscattered ultrasonic waves. *NDT & E International*. 36(7):461–469(2003).

Chen, B., & Liu, J. (2004). Experiment study on AE characteristics of three-point-bending concrete beams. *Cement and Concrete Research*, 34(3), 391-397.

Cheng, Y.; Hagan, P.C.; Mitra, R.; Wang, S. Defects Visualization Using Acoustic Emission Tomography Technique. *ACI Mater. J.* 2015, *112*, 755–766.

Chung, H. W., & Law, K. S. (1985). Assessing Fire Damage of Concrete by the Ultrasonic Pulse Technique.*Cement, Concrete, and Aggregates*, 7(2), 84-88.

Clark, M. R., McCann, D. M. & Forde, M. C. (2003). Application of infrared thermography to the non-destructive testing of concrete and masonry bridges. *NDT & E International*, 36(4), 265–275.

Colombo, S., Forde, M.C., Main, I.G., & Shigeishi, M. (2005). Predicting the ultimate bending capacity of concrete beams from the “relaxation ratio” analysis of AE signals.*Construction and Building Materials*, 19(10), 746-754.

Davis, A. G. (1995). Nondestructive evaluation of existing deep foundations. *Journal of performance of constructed facilities*, 9(1), 57-74.

Davis, A. G. (2003). The nondestructive impulse response test in North America: 1985-2001. *NDT&E International*, 36(4), 185-193.

Davis, J. L. & Annan, A. P.(1989). Ground-penetrating radar for high resolution mapping of soil and rock stratigraphy.*Geophysical Prospecting*, 37, 531-551.

Davis, A. G. and Dunn, C. S. (1974). From theory to field experience with the non-destructive vibration testing of piles. *In Institution of Civil Engineers*, Proceedings, 57(4), 571-593.

Davis, A. G. & Hertlein, B.H. (1987). Nondestructive testing of concrete pavement slabs and floors with the transient dynamic response method. In *ProcIntConfStruct faults repair, London*, 2, 429-433.

Farhidzadeh, A.; Mpalaskas, A.C.; Matikas, T.E.; Farhidzadeh, H.; Aggelis, D.G. Fracture mode identification in cementitious materials using supervised pattern recognition of acoustic emission features. *Constr. Build. Mater.* 2014, *67*, 129–138.

Farid, U., Numata, K., Shimasaki, J., Shigeishi, M. & Ohtsu, M. (2004). Mechanisms of crack propagation due to corrosion of reinforcement in concrete by AE-SiGMA and BEM, *Construction and Building Materials*, 18(3), 181–188.

Futterman, W. T. (1962). Dispersive body waves, *J. Geophys. Res.*, 67, 5279-5291.

Goldsmith, W. (1965). *Impact: The Theory and Physical Behavior of Colliding Solids, Edward Arnold Press, Ltd.*: 24-50.

Grosse, C. U. , & Finck, F. (2006). Quantitaive evaluation of fracture processes in concrete using signal-based acoustic emission techniques. *Cement and Concrete Composites*, 28(4), 330-336.

Grosse, C. U. & Ohtsu, M. (2008). Acoustic Emission Techniques. *Springer:Verlag Berlin heidelberg.*

Hoegh, K., Khazanovich, L., & Yu, H. T. (2011).Ultrasonic tomography for evaluation of concrete pavements.*Transportation Research Record*, 2232,85–94.

Hola, J. & Schabowicz, K. (2010). State-of-the-art non-destructive methods for diagnostic testing of building structures-anticipated development trends.*Archives of Civil and Mechanical Engineering*, 10(3), 5-18.

Howkins, S. D. (1968). Measurement of Pavement Thickness by Rapid and Nondestructive Methods, *NCHRP Report* 52, Highway Research Board, National Research Council, Washington, D.C., 82 .

Khan, M. F. H. (2015). Multi-sensing NDT Approaches for Inspection of Structural Components. Dissertation of Degree of Doctor of Philosophy, Faculty of Civil, Architectural and Environmental Engineering, Drexel University.

Kobayashi, Y. (2013). Mesh-independent ray-trace algorithm for concrete structure. Construction and Building Materials. 48(2013):1309-1317.

Krautkrämer, J. & Krautkrämer, H. (1990). Ultasonic testing of materials, *Springer: Verlag Berlin.*

Kurz, J. H., Finck, F., Grosse, C. U., & Reinhardt, H. W. (2006). Stress drop and street redistribution in concrete quantified over time by the b-value analysis. *Structural Health Monitoring*, 5(1), 69-81.

Labuz, J. F., Cattaneo, S. & Chen, L. H. (2001). Acoustic emission at failure in quasi-brittle materials. *Construction and Building Materials*, 15(5–6): 225–233.

Langenberg, K. J., Mayer, K. and Marklein, R. (2006).Nondestructive testing of concrete with electromagnetic and elastic waves: modeling and imaging," *Cement & Concrete Composites*, 28(4), 370–383.

Li, W. T., Sun, W. & Jiang, J.Y. (2011). Damage of concrete experiencing flexural fatigue load and closed freeze/thaw cycles simultaneously, *Construction and Building Materials*, 2011,25(5), 2604–2610.

Mailer, H. (1972). Pavement Thickness Measurement Using Ultrasonic Techniques. *Highway Research Record*, 378, 20-28.

Malhotra, V. M. & Carino, N . J. (2003). *Handbook of Nondestructive Testing of Concrete*, CRC Press, New York.

Martin, J., Broughton, K., Giannopolous, A., Hardy, M.S.A., Forde, M.C. (2001). Ultrasonic tomography of grouted duct post-tensioned reinforced concrete bridge beams, *NDT & E International*, 34(2), 107-113.

McCann, D.M. & Forde, M.C. (2001). Review of NDT methods in the assessment of concrete and masonry structures. *NDT & E International*, 34(2), 71-84.

Meyers, R., Smith D.G., Jol H.M., and Peterson C.R. (1996). Evidence for eight great earthquake-subsidence events detected with ground-penetrating radar, *Willapa barrier, Washington: Geology*, 24, 99-102.

Momoki, S.,Shiotani, T., Chai, H.K.,Aggelis, D.G. & Kobayashi, Y. (2013).Large-scale evaluation of concrete repair by three-dimensional elastic-wave based visualization technique, *Structural Health and Monitoring* 12(3),241-252.

Morton, H. L., Harrington, R. M. & Bjeletich, J. G. (1973). Acoustic Emissions of Fatigue Crack Growth, *Engineering Fracture Mechanic*, 5(3):691-697.

Nowers, O., Duxbury, D. J.·, Zhang, J., & Drinkwater, B. W. (2014). Novel ray-tracing algorithms in NDE: Application of Dijkstra and A∗algorithms to the inspection of an anisotropic weld. *NDT & E International*. 2014: 58–66.

Ohno, K. & M. Ohtsu (2010). Crack classification in concrete based on acoustic emission. *Construction and Building Materials*, 24(12): 2339-2346.

Ohtsu, M., Uchida, M., Okamoto, T., & Yuyama, S. (2002). Damage assessment of reinforced concrete beams qualified by acoustic emission. *ACI Structural journal*, 99(4), 411-417.

Ohtsu, M. & Watanabe, T. (2002).Stack imaging of spectral amplitudes based on impact-echo for flaw detection,*NDT & E International*, 35(3), 189–196.

Olson, L. D., and Wright, C. C. (1990). Nondestructive Testing for Repair and Rehabilitation, *Concrete International*, 12(3),58-64.

Osawa, S., Shiotani, T., Kitora, H. & Momiyama, Y. (2014). Damage Visualization of Imperfectly-Grouted Sheath in PC Structures. In Proceedings of the 31st Conference of the European Working Group on Acoustic Emission, Dresden, Germany, 3–5 September 2014.

Perenchio, W.F. (1989). The condition survey.*Concrete International*, 11(1), 59-62.

Pollock, A. A. (1989). Acoustic Emission Inspection. *Metals Handboo*k,17:278-294.

Rieck, C. &Hillemeier, B. (2003). Detecting voids inside ducts of bonded steel tendons using impulse thermography, in Proceedings of the International Symposium

Non-Destructive Testing in Civil Engineering (NDT-CE '03), Berlin, Germany, September 2003. •

Sansalone, M. (1986). Flaw Detection in Concrete Using Transient Stress Waves, *Ph.D. Dissertation, Cornell University*: 220.

Sansalone, M., & Carino, N. J. (1986).Impact-Echo: A Method for Flaw Detection in Concrete Using Transient Stress Waves, NBSIR 86-3452, *National Bureau of Standards*, 222.

Sansalone, M., and Carino, N. J. (1991). Stress Wave Propagation Methods, in *Handbook on Nondestructive Testing of Concrete*, Chapter 12. V. M. Malhotra and N. J. Carino, CRC Press, Boca Raton, Fla., 275-304.

Sansalone, M. J., and Streett, W. B. (1997).*Impact-Echo: Nondestructive Evaluation of Concrete and Masonry*, Bullbrier Press, Ithaca, N.Y, 339.

Schabowicz K. (2014). Ultrasonic tomography – The latest nondestructive technique for testing concrete members – Description, test methodology, application example. *Archives of Civil and Mechanical Engineering* ,14(2), 295–303.

Schechinger, B., and Vogel, T. (2007).Acoustic emission for monitoring a reinforced concrete beam subject to four-point-bending. *Construction and Building materials*, 21(3), 483-490.

Sheriff R.E. (2002). Encyclopedic dictionary of exploration geophysics, *SEG*,4th ed,429.

Shiotani, T., & Aggelis, D.G. (2007).Evaluation of repair effect for deteriorated concrete piers of intake dam using AE activity.*Journal of Acoustic Emission*, 25,69-79.

Shiotani, T., Bisschop, J., & Van Mier, J. G. M. (2003).Temporal and spatial development of drying shrinkage cracking in cement-based materials.*Engineering Fracture mechanics*, 70(12), 1509-1525.

Shiotani, T., Fujii, K., Aoki, T., & Amou, K. (1994).Evaluation of progressive failure using AE sources and improved b-value on slope model tests.*Progress in acoustic emission*, 7(7), 529-534.

Shiotani, T.; Kobayashi, Y.; Chang, K.C. Hybrid elastic-wave CT with impact acoustics for single-side measurement in concrete structures. *Constr. Build. Mater.* 2016, *112*, 907–914.

Shiotani, T., Momoki, S., Chai, H. K. & Aggelis, D. G. (2009). Elastic wave validation of large concrete structures repaired by means of cement grouting. *Construction and Building Materials*, 23(7), 2647-2652.

Shiotani, T., Nakanishi, Y., Iwaki, K., Luo, X., & Haya, H. (2005). Evaluation of reinforcement in damaged railway concrete piers by means of acoustic emission. *Journal of Acoustic emission*, 23, 260-271.

Shiotani, T., Nakanishi, Y., Luo, X., Haya, H., & Inaba, T. (2004).Damage evaluation for railway structures by means of acoustic emission.*Key Engineering Materials*, 270, 1622-1630.

Shiotani, T., Ohtsu, M., & Ikeda, K. (2001). Detection and evaluation of AE waves due to rock deformation. *Construction and Building Materials*, 15(5), 235-246.

Steinbach, J. & Vey, E. (1975).Caisson evaluation by stress wave propagation method.*Journal of the Geotechnical Engineering Division*, 101(4), 361-378.

Su, B. L., Zhang, Y. H., Peng, L. H., Yao, D. N. & Zhang, B. F. (2000). The use of simultaneous iterative reconstruction technique for electrical capacitance tomography. *Chemical Engineering Journal* , 77(1–2): 37–41.

Teodoru, G. V. M., & Herf, J. (1996). Engineering Society Cologne Presents Itself (NDT Methods).*Proceedings* Fourteenth World Conference on NDT, Dec. 8-13, New Delhi, India, C. G. Krishnadas et al., eds., Oxford & IBH Publishing Co., V. 2, pp. 939-943.

Tian, G.Y.; Sophian, A.; Taylor, D.; Rudlin, J. Multiple Sensors on Pulsed Eddy Current Detection for 3-D Subsurface Crack Assessment. *IEEE Sens. J.* 2005, *5*, 90–96.

Tronicke J., Tweeton D. R., Dietrich, P. & Appel, E.(2001). Improved crosshole radar tomography by using direct and reflected arrival times. *Journal of Applied Geophysics*. 47(2):97–105 (2001).

Tonn, R. (1991). The determination of the seismic quality factor Q from VSP data: a comparison of different computational methods. *Geophysical Prospecting*,39,1-37.

Valle, S., Zanzi, L. & Rocca, F. (1999). Radar Tomography for NDT: comparison of techniques. *Journal of Applied Geophysics*, 41(1999):259-269.

Vladimir, S. (2013). QVOA techniques for fracture characterization. *Geofísica Internacional*, 54(2), 311-320.

Ward, R. W. & Toksoz, M. N. (1971). Causes of regional variation of magnitude. *SSA bull*, 61, 649-670.

Wu, K., Chen, B., & Yao, W. (2000). Study on the AE characteristics of fracture process of mortar, concrete and steel-fiber-reinforced concrete beams. *Cement and Concrete Research*, 30(9), 1495-1500.

Zhu, J. & Popovics, J. S. (2007). Imaging Concrete Structures using the Air-coupled Impact-Echo. *ASCE J. Eng. Mech*, 133(6) 628-640.

APPENDICES

APPENDIX A : Programme Algorithm

A.1 Setup of model

```
int q, iteration,n,m,total_cell,no_of_cell ;
  double *vel,*attenuation_coefficient,attenuation,x,y,interval_of_x,interval_of_y,velocity;
  scanf("%d",&iteration);
  scanf("%lf%lf%d%d", &x, &y, &n, &m);
  interval_of_x = x/n;
  interval_of_y = y/m;
  total_cell=n*m;
  vel= (double *)calloc (total_cell , sizeof(double));
  for ( no_of_cell=0 ; no_of_cell<total_cell ; no_of_cell++)
    {
      scanf("%lf",&velocity);
      vel[no_of_cell]=velocity;
    }
  attenuation_coefficient= (double *)calloc (total_cell, sizeof(double));
  for (no_of_cell=0; no_of_cell<total_cell; no_of_cell++)
    {
      scanf("%lf",&attenuation);
      attenuation_coefficient[no_of_cell]=attenuation;
    }

  int a,b;
  int n1,m1,n1m1,i,j,nodenum;
  double **node;
  int no_of_node,total_node,source,no_source,node_of_source,*source_node;

  n1=n+1;
  m1=m+1;
  n1m1=(n+1)*(m+1);
  total_node=n1m1;
  node    = (double **)calloc (total_node,sizeof(double*));
  node[0] = (double *)calloc (total_node * 2,sizeof(double));

  for ( a = 1; a < total_node; a++ )
    {
      node[ a ] = node[ a - 1 ] + 2;
    }

  double xinterval = x / n, yinterval = y / m;
  for ( i=0 ; i < n+1 ; i++)
    {
      for (j=0 ; j < m+1 ; j++)
        {
          nodenum = (n1*j)+i;
          node[ nodenum ][ 0 ] = xinterval * i;
          node[ nodenum ][ 1 ] = yinterval * j;
        }
    }

  scanf("%d",&no_source);
  source_node= (int *)calloc (no_source , sizeof(int));
  for (source=0 ; source<no_source ; source++)
    {
      scanf("%d",&node_of_source);
      source_node[source]=node_of_source;
    }

  int **receiver_node,no_receivers,receiver,node_of_receiver;
```

```
double **traveltime,travel_time,**obs_amp_factor,s_amplitude;
scanf("%d",&no_receivers);

receiver_node = (int **) calloc(no_source, sizeof (int*));
for (source=0 ; source<no_source ; source++)
  {
    receiver_node[source]=(int *) calloc(no_receivers,sizeof (int));
    for (receiver=0; receiver<no_receivers ; receiver++)
      {
        scanf("%d",&node_of_receiver) ;
        receiver_node[source][receiver]=node_of_receiver;
      }
  }

traveltime=(double **) calloc(no_source, sizeof (double*));
for (source=0 ; source<no_source ; source++)
  {
    traveltime[source]=(double *) calloc(no_receivers,sizeof (double));
    for (receiver=0; receiver<no_receivers ; receiver++)
      {
        scanf("%lf",&travel_time) ;
        traveltime[source][receiver]=travel_time;
      }
  }

obs_amp_factor=(double **) calloc(no_source, sizeof (double*));

for (source=0 ; source<no_source ; source++)
  {
    obs_amp_factor[source]=(double *)calloc(no_receivers,sizeof (double));
    for (receiver=0; receiver<no_receivers ; receiver++)
      {
        scanf("%lf", &s_amplitude);
        obs_amp_factor[source][receiver]=s_amplitude;
      }
  }
```

A.2 Ray trace

```
void straight(double interval_of_x, double interval_of_y, int n1, int m1, int source_node,int
receiver_node, double *vel, double *sum, double **Raypath)
{
  int i,j;
  int sratioy= source_node/n1 ;
  int sratiox= source_node - (sratioy*n1) ;
  int rratioy= receiver_node/n1;
  int rratiox= receiver_node - (rratioy*n1) ;
  int rratioy1 = rratioy-1;
  double x1= sratiox*interval_of_x ;
  double y1= sratioy*interval_of_y ;
  double x2= rratiox*interval_of_x;
  double y2= rratioy*interval_of_y;
  double a=y2-y1 ;
  double b=x2-x1 ;
  double c=(x2*y1)-(x1*y2) ;
  int n=n1-1;
  int m=m1-1;
  int total_cell = n*m;
```

```
 int max;
 if (fabs(a)<0.000001 && b>0) {
   max=rratiox+1-sratiox;
 }
 else if (fabs(a)<0.000001 && b<0){
   max=sratiox+1-rratiox;
 }
 else if (fabs(b)<0.000001 && a>0){
   max= rratioy+1-sratioy;
 }
 else if (fabs(b)<0.000001 && a<0) {
   max=sratioy+1-rratioy;
 }
 else if (a<0 && b>0){
   max = (rratiox+1-sratiox) + (sratioy-1-rratioy);
 }
 else if (a>0 && b<0){
   max = (sratiox+1-rratiox)+(rratioy-1-sratioy);
 }
 else if (a<0 && b<0) {
   max = (sratiox+1-rratiox)+(sratioy-1-rratioy);
 }
 else
   {
     max = (rratiox+1-sratiox)+(rratioy1-sratioy);
   }

 double distanced,cox,coy, *corx, *cory, *distance,*newcorx, *newcory, *centre_corx,
*centre_cory, *caltravel_time ;
 (corx) = (double *)calloc (max , sizeof(double));
 (cory) = (double *)calloc (max , sizeof(double));

 int countered, counter = 0;
 if (fabs(a)<0.000001 && b>0) {

   for      (i=sratiox ; i<=rratiox ; i++){
     (corx)[ counter ]=i * interval_of_x;
     (cory)[ counter ]=y1 ;
     counter++;
   }
 }
 else if (fabs(a)<0.000001 && b<0){
   for (i=sratiox ; i>=rratiox ; --i){
     (corx)[ counter ]=i * interval_of_x;
     (cory)[ counter ]=y1 ;
     counter++;
   }
 }

 else if (a<0 && b>0){
   for      (i=sratiox ; i<=rratiox ; i++){
     (corx)[ counter ]=i * interval_of_x;
     (cory)[ counter ]= (c/b) + (a/b) * (corx)[ counter ] ;
     counter++;
   }
```

```
}
else if (a>0 && b<0){
  for (i=rratiox ; i<=sratiox ; i++){
    (corx)[ counter ]=i * interval_of_x;
    (cory)[ counter ]= (c/b) + (a/b) * (corx)[ counter ] ;
    counter++;
  }
}

else if (a<0 && b<0) {
  for (i=rratiox ; i<=sratiox ; i++){
    (corx)[ counter ]=i * interval_of_x;
    (cory)[ counter ]= (c/b) + (a/b) * (corx)[ counter ] ;
    counter++;
  }
}

else if(a>0 && b>0)
  {
    for     (i=sratiox ; i<=rratiox ; i++){
      (corx)[ counter ]=i * interval_of_x;
      (cory)[ counter ]= (c/b) + (a/b) * (corx)[ counter ] ;
      counter++;
  }
  }


 if (fabs(b)<0.000001 && a>0){
  for (j=sratioy ; j<=rratioy ; j++){

    (cory)[ counter ]=j * interval_of_y;
    (corx)[ counter ]= x1 ;
    counter++;
  }
}
 else if (fabs(b)<0.000001 && a<0) {

  for (j=sratioy ; j>=rratioy ; --j){
    (cory)[ counter ]=j * interval_of_y;
    (corx)[ counter ]= x1 ;
    counter++;
  }
}

else if (a<0 && b>0){
  for (j=rratioy+1 ; j<sratioy ; j++){
    (cory)[ counter ]=j * interval_of_y;
    (corx)[ counter ]= -(c/a) + (b/a) * (cory)[ counter ] ;
    counter++;
  }
}
else if (a>0 && b<0){
  for (j=sratioy+1 ; j<rratioy ; j++){

    (cory)[ counter ]=j * interval_of_y;
    (corx)[ counter ]= -(c/a) + (b/a) * (cory)[ counter ] ;
```

```
    counter++;
   }
  }
  else if (a<0 && b<0) {
   for (j=rratioy+1 ; j<sratioy ; j++){

    (cory)[ counter ]=j * interval_of_y;
    (corx)[ counter ]= -(c/a) + (b/a) * (cory)[ counter ] ;
    counter++;
   }
  }

  else if(a>0 && b>0)
   {
    for (j=sratioy+1 ; j<rratioy ; j++){

     (cory)[ counter ]=j * interval_of_y;
     (corx)[ counter ]= -(c/a) + (b/a) * (cory)[ counter ] ;
     counter++;
    }
   }

  (distance) = (double *)calloc (max, sizeof(double));

  for (counter=0 ; counter<max ; counter++){
   (distance)[counter]=sqrt(pow(((corx)[counter]-x1),2)+pow(((cory)[counter]-y1),2)) ;
  }

  for (counter=0 ; counter<max ; counter++){
   for (countered=counter+1;countered<max;countered++){
    if ((distance)[counter]>(distance)[countered]){
     distanced= (distance)[counter];
     (distance)[counter]=(distance)[countered];
     (distance)[countered]=distanced;
     cox=(corx)[counter];
     (corx)[counter]=(corx)[countered];
     (corx)[countered]=cox;

     coy=(cory)[counter];
     (cory)[counter]=(cory)[countered];
     (cory)[countered]=coy;
    }
   }
  }

  double *gate;
 int con=1,zzz;
 (gate)= (double *)calloc (max, sizeof(double));
 for (counter=0 ; counter<max-1 ; counter++) {
  zzz=counter+1;
  (gate)[con]= (distance)[zzz]-(distance)[counter];
  con++;
 }

 int ct=0;
 for (con=1; con<max;con++)
```

```
  {
 if ((gate)[con]<0.00001)
  {
    ct++;
  }
  }

 (newcorx)=(double*)calloc (max-ct, sizeof(double));
 (newcory)=(double*)calloc (max-ct, sizeof(double));
 int coun=1;
 for (con=1;con<max;con++)
  {

    if((gate)[con]>0.00001)
      {
        (newcorx)[coun]=(corx)[con];
              (newcory)[coun]=(cory)[con];
              coun++;
      }
  }
 (newcorx)[0]=(corx)[0];
 (newcory)[0]=(cory)[0];

 (centre_corx)=(double*)calloc (max-ct-1, sizeof(double));
 (centre_cory)=(double*)calloc (max-ct-1, sizeof(double));

 int com=0;
 for (counter = 0; counter <max-ct; counter++)
  {
    countered=counter+1;
    (centre_corx)[com]=((newcorx)[countered]+(newcorx)[counter])/2;
    (centre_cory)[com]=((newcory)[countered]+(newcory)[counter])/2;
    com++;
  }

  int cot=0;
  double interval_x_per2=interval_of_x / 2;
  double interval_y_per2=interval_of_y / 2;
  double y=n*interval_of_x;
  int *cell;
(cell)=(int*)calloc (max-ct-1, sizeof(int));

 for (com     = 0; com     <max-ct-1 ; com ++)
  {
    if (a==0){
  int a=  ((centre_corx)[com]/interval_of_x);

double b1=  (centre_cory)[com] + interval_y_per2 ;
    double b2=  (centre_cory)[com] - interval_y_per2  ;
    if (b1<=0){
        b1=b2;
    }
    if(b2<=0){
        b2=b1;
    }
```

```
        int bb1=  b1/interval_of_y  ;
                        int bb2= b2/interval_of_y  ;
                        int c1=a+ (bb1*n);
                        int c2=a+ (bb2*n);

                        double cc1= vel[c1];
                        double cc2=vel[c2];
                        if (cc1 >= cc2){
                          (cell)[cot]= c1 ;
                          cot++;

                        }
                        else {
                          (cell)[cot]= c2 ;
                          cot++;
                        }
                        }

 else if (b==0) {
     double a1=  (centre_corx)[com] + interval_x_per2;
     double a2 = (centre_corx)[com] - interval_x_per2;
     if (a1>= y){
       a1=a2;
     }
     if(a2<=0){
       a2=a1;
     }

     int aa1= a1 / interval_of_x;
     int aa2= a2 / interval_of_x;
     int b=  ((centre_cory)[com]/interval_of_y)  ;
     int c= b*n;
     int c1= aa1+c;
     int c2= aa2+c;
     double cc1= vel[c1];
     double cc2=vel[c2];

                            if (cc1 >= cc2){
                              (cell)[cot]= c1 ;
                              cot++;
                            }
                            else {
                              (cell)[cot]= c2 ;
                              cot++;
                            }
}

 else {
    int aa=  ((centre_corx)[com]/interval_of_x);
     int bb=  ((centre_cory)[com]/interval_of_y)  ;
     int cc= bb*n;
     (cell)[cot]= aa + cc ;
     cot++;
 }
   }
```

```
 double *D;
(D)=(double*)calloc(max-ct-1, sizeof(double));
int cott=0;
for (counter     = 0; counter     <max-ct-1 ; counter ++)
{
  int countered=counter+1;
  double aaa= pow(((newcorx)[countered]-(newcorx)[counter]),2);
  double bbb= pow(((newcory)[countered]-(newcory)[counter]),2);
  (D)[cott]=sqrt(aaa+bbb) ;

  cott++;
}

 (*Raypath)=(double*)calloc(total_cell, sizeof(double));
for (counter     = 0; counter <max-ct-1; counter ++)
  {
    (*Raypath)[(cell)[counter]]=(D)[counter];
   }


(caltravel_time)=(double*)calloc(max-ct-1, sizeof(double));
int cottt=0;
  for (counter     = 0; counter     <max-ct-1 ; counter ++)
    {

      (caltravel_time)[cottt]= ((D)[counter]) / (vel[(cell)[counter]]);

             cottt++;
    }

  *sum=0;
  for (cottt=0 ; cottt<max-ct-1 ;cottt++)
  {
    *sum = *sum + (caltravel_time)[cottt];
  }
```

A.3 Travel time technique

```
int counter,countered;
 double temporary_sum,*temporary_D;

  temporary_D=(double *) calloc(total_cell, sizeof (double));

for (counter=0; counter<total_node;counter++){
 for (countered=counter+1;countered<total_node;countered++){
  if (finalsum[counter]>finalsum[countered]){
temporary_sum=finalsum[counter];
                                   finalsum[counter]=finalsum[countered];
                                   finalsum[countered]=temporary_sum;

for ( no_of_cell=0 ; no_of_cell<total_cell ; no_of_cell++) {
                                    temporary_D[no_of_cell]=D0[counter][no_of_cell];
                                    D0[counter][no_of_cell]=D0[countered][no_of_cell];
                                    D0[countered][no_of_cell]=temporary_D[no_of_cell];
   }}}}
```

```
factor[source][receiver]=finalsum[0];
  pathway[source][receiver]=(double *) calloc(total_cell, sizeof (double));

for ( no_of_cell=0 ; no_of_cell<total_cell ; no_of_cell++) {
                                        pathway[source][receiver][no_of_cell]=D0[0][no_of_cell];
   }
  free (finalsum);
   free (D0);
     }
   }

    int counter;
    double **summation_of_D;
    summation_of_D=(double **) calloc(no_source, sizeof (double*));

    for (source=0 ; source<no_source ; source++ )
      {
       summation_of_D[source]=(double *) calloc(no_receivers, sizeof (double));

       for (receiver=0 ; receiver<no_receivers ; receiver++)
         {

          double sum_D=0;
          for (counter=0; counter<total_cell;counter++)
            {
             sum_D=sum_D+pathway[source][receiver][counter];
            }
                summation_of_D[source][receiver]=sum_D;
         }
      }

    double ***factor3;
    factor3=(double ***) calloc(no_source, sizeof (double**));
    for (source=0 ; source<no_source ; source++ )
      {
       factor3[source]=(double **) calloc(no_receivers, sizeof (double*));
       for (receiver=0 ; receiver<no_receivers ; receiver++)
         {
          double sum=summation_of_D[source][receiver];
          double error_t= traveltime[source][receiver] - factor[source][receiver];
          double  individual_change_of_slowness= error_t / sum;
         factor3[source][receiver]=(double *) calloc(total_cell, sizeof (double));
          for (no_of_cell=0; no_of_cell< total_cell;no_of_cell++)
            {
             factor3[source][receiver][no_of_cell] = individual_change_of_slowness *
pathway[source][receiver][no_of_cell] ;
            }

         }
      }

    double *factor4=0;
    factor4 = (double *) calloc(total_cell, sizeof (double));

    for (source=0;source<no_source;source++){
      for (receiver=0 ; receiver<no_receivers ; receiver++)
        {

         for ( no_of_cell=0 ; no_of_cell<total_cell ; no_of_cell++)
           {

             factor4[no_of_cell]= factor4[no_of_cell] + factor3[source][receiver][no_of_cell] ;
           }
```

```
        }
    }
    double *factor5=0;
    factor5 = (double *) calloc(total_cell, sizeof (double));

    for (source=0 ; source<no_source ; source++ )
      {
        for (receiver=0 ; receiver<no_receivers ; receiver++)
          {
   for ( no_of_cell=0 ; no_of_cell<total_cell ; no_of_cell++)
            {
              factor5[no_of_cell]= factor5[no_of_cell] + pathway[source][receiver][no_of_cell];
            }
          }
      }
    double *final_slowness;
    final_slowness=(double *) calloc(total_cell, sizeof (double));
    for ( no_of_cell=0 ; no_of_cell<total_cell ; no_of_cell++)
      {

        if ( fabs(factor5[no_of_cell])<0.000001 )
        {
          final_slowness[no_of_cell]= 1 / vel[no_of_cell]; }
        else {
final_slowness[no_of_cell]= (1/vel[no_of_cell]) + (factor4[no_of_cell] / factor5[no_of_cell]) ;
        }
     }

    double *final_velocity;
    final_velocity=(double *) calloc(total_cell, sizeof (double));
    for ( no_of_cell=0 ; no_of_cell<total_cell ; no_of_cell++)
      {
        final_velocity[no_of_cell] = 1/ final_slowness[no_of_cell];
      }

    for ( no_of_cell=0 ; no_of_cell<total_cell ; no_of_cell++){

     vel[no_of_cell]=final_velocity[no_of_cell];
                    }
```

A.4 Amplitude technique

```
double **fac;
    fac=(double **) calloc(no_source, sizeof (double*));
    for (source=0 ; source<no_source ; source++ )
      {
        fac[source]=(double *) calloc(no_receivers, sizeof (double));
        for (receiver=0 ; receiver<no_receivers ; receiver++)
          {
            fac[source][receiver]= -log( obs_amp_factor[source][receiver]);
          }
      }

    double ***fac1;
    fac1=(double ***) calloc(no_source, sizeof (double**));
    for (source=0 ; source<no_source ; source++ )
      {
        fac1[source]=(double **) calloc(no_receivers, sizeof (double*));
        for (receiver=0 ; receiver<no_receivers ; receiver++)
          {
            fac1[source][receiver]=(double *) calloc(total_cell, sizeof (double));
            for (no_of_cell=0; no_of_cell< total_cell;no_of_cell++)
              {
```

```
               fac1[source][receiver][no_of_cell]=
attenuation_coefficient[no_of_cell]*pathway[source][receiver][no_of_cell];
          }
      }
      }

    double **fac2;
    fac2=(double **) calloc(no_source, sizeof (double*));
    for (source=0 ; source<no_source ; source++ )
      {
        fac2[source]=(double *) calloc(no_receivers, sizeof (double));
        for (receiver=0 ; receiver<no_receivers ; receiver++)
          {

  for (no_of_cell=0; no_of_cell< total_cell;no_of_cell++)
    {
      fac2[source][receiver]=fac2[source][receiver]+ fac1[source][receiver][no_of_cell];

    }
          }
      }

    double **fac3;
    fac3=(double **) calloc(no_source, sizeof (double*));
    for (source=0 ; source<no_source ; source++ )
      {
        fac3[source]=(double *) calloc(no_receivers, sizeof (double));
        for (receiver=0 ; receiver<no_receivers ; receiver++)
          {

            for (no_of_cell=0; no_of_cell< total_cell;no_of_cell++)
              {
                fac3[source][receiver]=fac[source][receiver]-fac2[source][receiver];

              }
          }
      }
    double **fac4;
    fac4=(double **) calloc(no_source, sizeof (double*));
    for (source=0 ; source<no_source ; source++ )
      {
        fac4[source]=(double *) calloc(no_receivers, sizeof (double));
        for (receiver=0 ; receiver<no_receivers ; receiver++)
          {

                    fac4[source][receiver]= fac3[source][receiver] / summation_of_D[source][receiver];
          }
      }

    double ***fac5;
    fac5=(double ***) calloc(no_source, sizeof (double**));
    for (source=0 ; source<no_source ; source++ )
      {
        fac5[source]=(double **) calloc(no_receivers, sizeof (double*));
        for (receiver=0 ; receiver<no_receivers ; receiver++)
          {
            fac5[source][receiver]=(double *) calloc(total_cell, sizeof (double));
            for (no_of_cell=0; no_of_cell< total_cell;no_of_cell++)
              {
                fac5[source][receiver][no_of_cell]=
fac4[source][receiver]*pathway[source][receiver][no_of_cell];

              }
```

```
        }
      }

    double *fac6=0;
    fac6 = (double *) calloc(total_cell, sizeof (double));

    for (source=0;source<no_source;source++){
      for (receiver=0 ; receiver<no_receivers ; receiver++)
        {
          for ( no_of_cell=0 ; no_of_cell<total_cell ; no_of_cell++)
            {

              fac6[no_of_cell]= fac6[no_of_cell] + fac5[source][receiver][no_of_cell] ;

            }
        }
    }

    double *final_attenuate;
    final_attenuate=(double *) calloc(total_cell, sizeof (double));
    for ( no_of_cell=0 ; no_of_cell<total_cell ; no_of_cell++)
      {

        if ( fabs(factor5[no_of_cell])<0.000001 )
          {
            final_attenuate[no_of_cell]=  attenuation_coefficient[no_of_cell]; }
        else {
          final_attenuate[no_of_cell]=  attenuation_coefficient[no_of_cell] + (fac6[no_of_cell] /
factor5[no_of_cell]) ;
        }
      }

    for ( no_of_cell=0 ; no_of_cell<total_cell ; no_of_cell++)
      {
        attenuation_coefficient[no_of_cell]=final_attenuate[no_of_cell] ;
      }
```

A.5 Frequency technique

```
double **fac;
    fac=(double **) calloc(no_source, sizeof (double*));
    for (source=0 ; source<no_source ; source++ )
      {
        fac[source]=(double *) calloc(no_receivers, sizeof (double));
        for (receiver=0 ; receiver<no_receivers ; receiver++)
          {
           fac[source][receiver]= d_frequency[source][receiver] / variance[source] ;
                }
      }

    double ***fac1;
    fac1=(double ***) calloc(no_source, sizeof (double**));
    for (source=0 ; source<no_source ; source++ )
      {
        fac1[source]=(double **) calloc(no_receivers, sizeof (double*));
        for (receiver=0 ; receiver<no_receivers ; receiver++)
          {
            fac1[source][receiver]=(double *) calloc(total_cell, sizeof (double));

            for (no_of_cell=0; no_of_cell< total_cell;no_of_cell++)
              {
```

```
              fac1[source][receiver][no_of_cell]=
attenuation_coefficient[no_of_cell]*pathway[source][receiver][no_of_cell];
         }
      }
      }

    double **fac2;
    fac2=(double **) calloc(no_source, sizeof (double*));
    for (source=0 ; source<no_source ; source++ )
      {
        fac2[source]=(double *) calloc(no_receivers, sizeof (double));
        for (receiver=0 ; receiver<no_receivers ; receiver++)
          {
            double jumlah=0;
  for (no_of_cell=0; no_of_cell< total_cell;no_of_cell++)
    {
      jumlah=jumlah + fac1[source][receiver][no_of_cell];

    }
  fac2[source][receiver]=jumlah;
          }
      }

    double **fac3;
    fac3=(double **) calloc(no_source, sizeof (double*));
    for (source=0 ; source<no_source ; source++ )
      {
        fac3[source]=(double *) calloc(no_receivers, sizeof (double));
        for (receiver=0 ; receiver<no_receivers ; receiver++)
          {

            for (no_of_cell=0; no_of_cell< total_cell;no_of_cell++)
              {
                fac3[source][receiver]=fac[source][receiver]-fac2[source][receiver];

              }
          }
      }
    double **fac4;
    fac4=(double **) calloc(no_source, sizeof (double*));
    for (source=0 ; source<no_source ; source++ )
      {
        fac4[source]=(double *) calloc(no_receivers, sizeof (double));
        for (receiver=0 ; receiver<no_receivers ; receiver++)
          {
                        fac4[source][receiver]= fac3[source][receiver] / summation_of_D[source][receiver];
          }
      }

    double ***fac5;
    fac5=(double ***) calloc(no_source, sizeof (double**));
    for (source=0 ; source<no_source ; source++ )
      {
        fac5[source]=(double **) calloc(no_receivers, sizeof (double*));
        for (receiver=0 ; receiver<no_receivers ; receiver++)
          {
            fac5[source][receiver]=(double *) calloc(total_cell, sizeof (double));
            for (no_of_cell=0; no_of_cell< total_cell;no_of_cell++)
              {
                fac5[source][receiver][no_of_cell]=
fac4[source][receiver]*pathway[source][receiver][no_of_cell];

              }
```

```
        }
      }

    double *fac6=0;
    fac6 = (double *) calloc(total_cell, sizeof (double));

    for (source=0;source<no_source;source++){
      for (receiver=0 ; receiver<no_receivers ; receiver++)
        {
          for ( no_of_cell=0 ; no_of_cell<total_cell ; no_of_cell++)
            {

              fac6[no_of_cell]= fac6[no_of_cell] + fac5[source][receiver][no_of_cell] ;

            }
        }
    }

    double *final_attenuate;
    final_attenuate=(double *) calloc(total_cell, sizeof (double));
    for ( no_of_cell=0 ; no_of_cell<total_cell ; no_of_cell++)
      {

        if ( fabs(factor5[no_of_cell])<0.000001 )
          {
            final_attenuate[no_of_cell]=  attenuation_coefficient[no_of_cell]; }
        else {
          final_attenuate[no_of_cell]=  attenuation_coefficient[no_of_cell] + (fac6[no_of_cell] /
factor5[no_of_cell]) ;
        }
      }

    for ( no_of_cell=0 ; no_of_cell<total_cell ; no_of_cell++)
      {
        attenuation_coefficient[no_of_cell]=final_attenuate[no_of_cell] ;

      }
```

A.6 Design platform of first travel time and first peak attraction

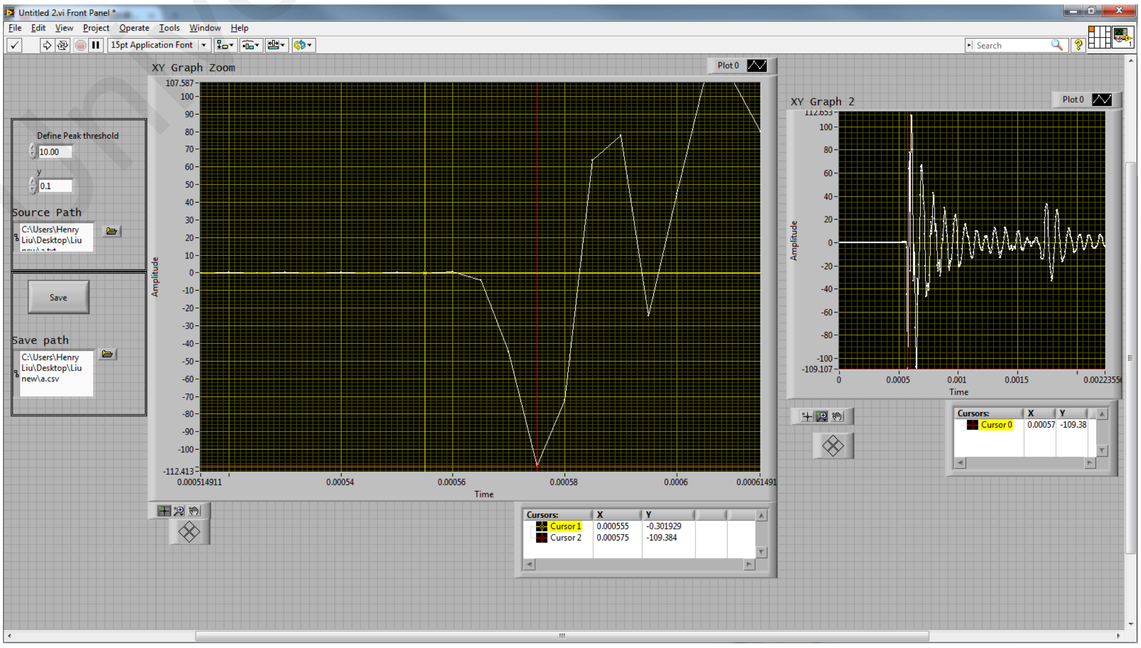

Figure A1: The screenshot of the design platform by showing the yellow cursor pointing the first arrival travel time and red colour cursor on the first peak amplitude of one waveform.

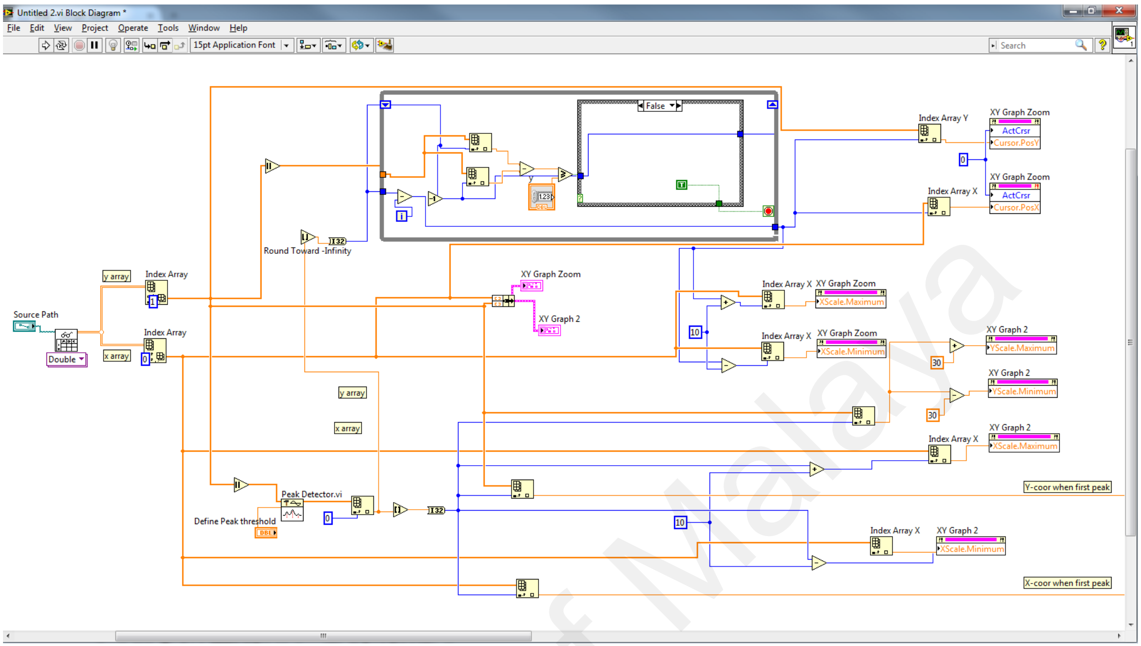

Figure A2, continued.

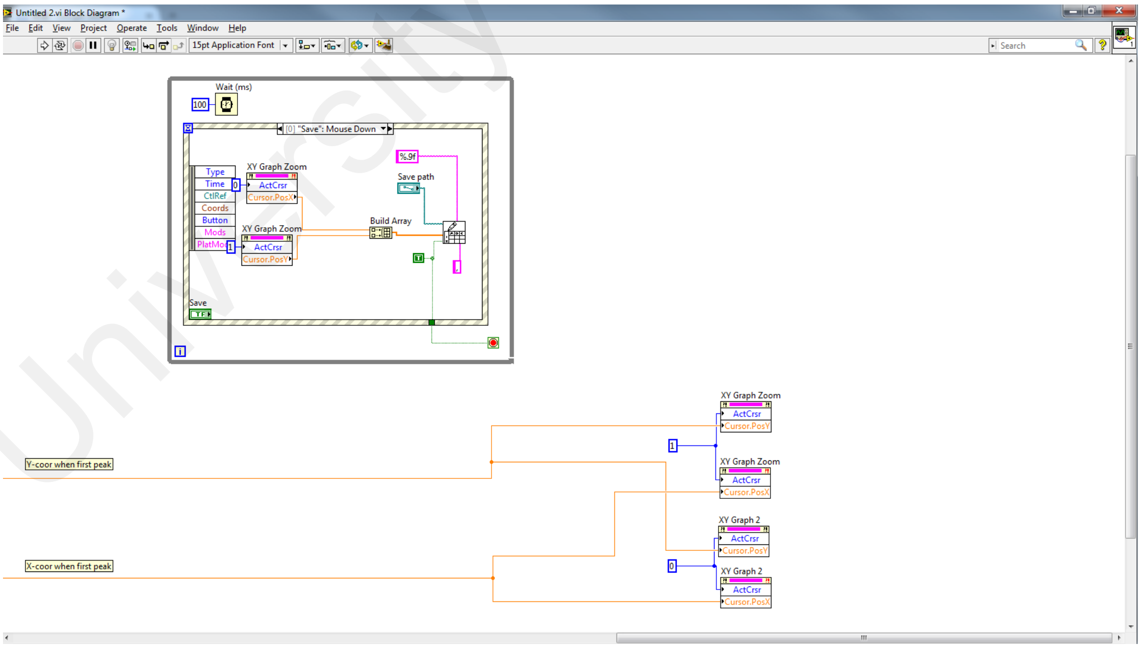

Figure A2: The screenshot of block diagram of the design platform of Figure A1.

APPENDIX B : TOMOGRAM

B.1 Concrete model with honeycomb

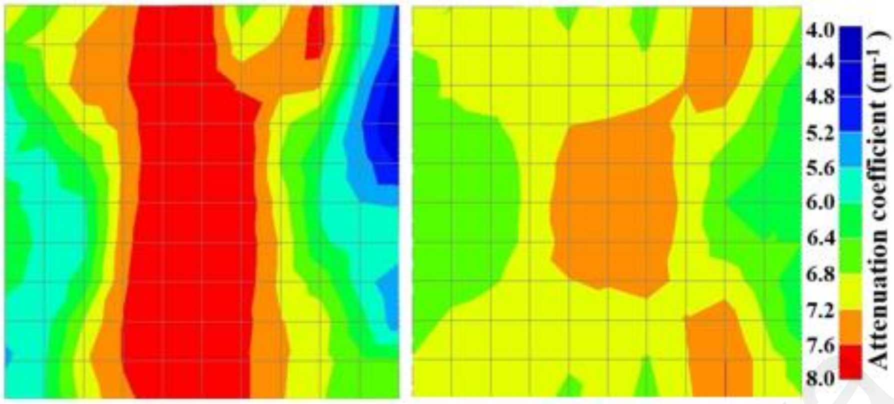

(a) (b)

Figure B1: Tomogram of case Figure 3.7, PC with polyethylene tendon sheath plotted by 25khz frequency laboratory 2 sided amplitude technique:(a) 0 % grout filling; (b) 100% filling.

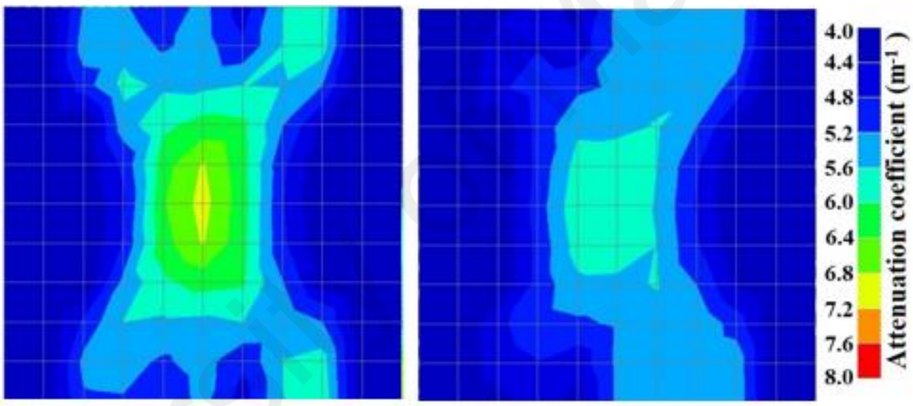

(a) (b)

Figure B2: Tomogram of case Figure 3.7, PC with polyethylene tendon sheath plotted by 18khz frequency laboratory 2 sided amplitude technique:(a) 0 % grout filling; (b) 100% filling.

B.2 Concrete specimen with honeycomb

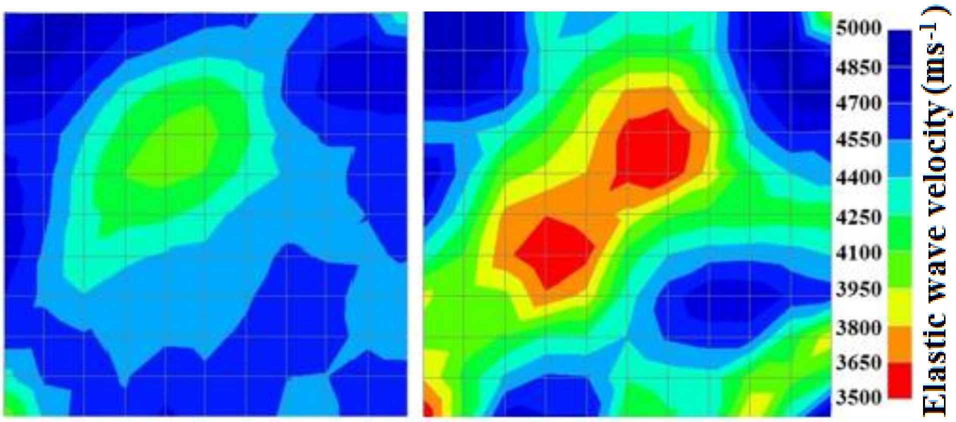

(a) (b)

Figure B3: Tomogram of case Figure 3.7 by laboratory 25 kh frequency, 4 sided travel time technique: (a) sound concrete;(b) honeycomb.

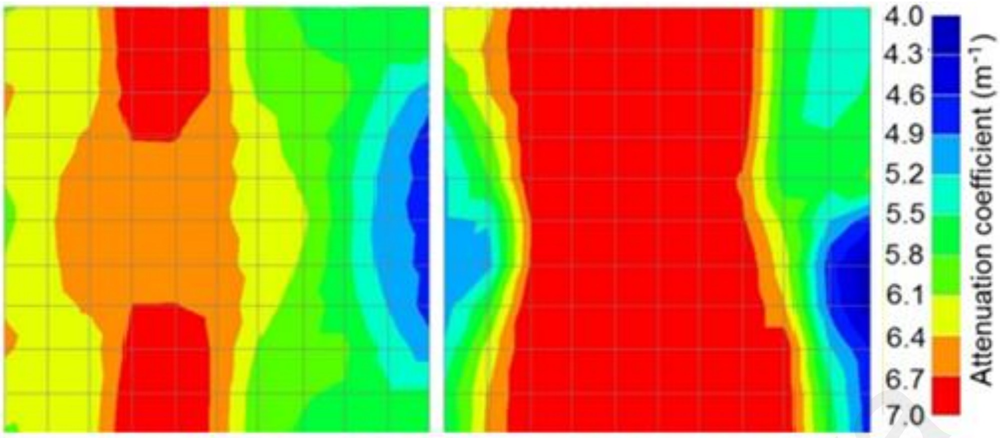

(a) (b)

Figure B4: Tomogram of Figure 3.7 by laboratory 2 sided amplitude technique:(a) sound concrete;(b) honeycomb.

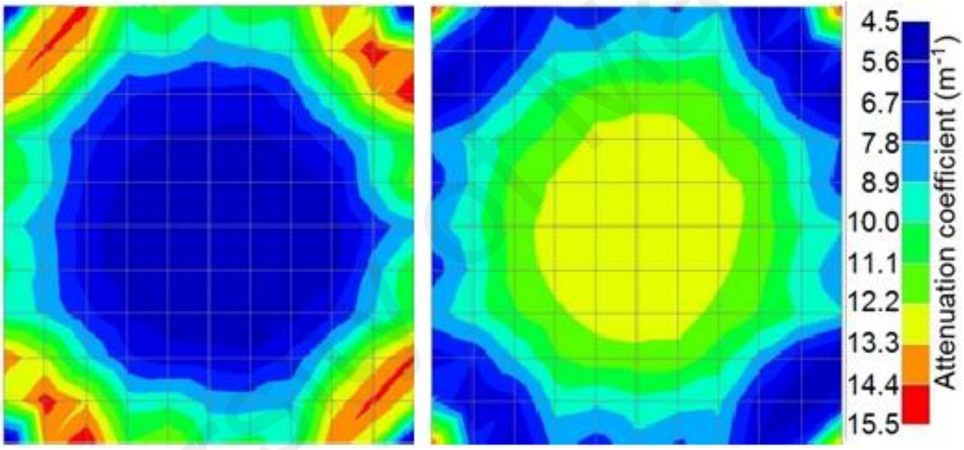

(a) (b)

Figure B5: Tomogram of Figure 3.7 by laboratory 4 sided frequency technique: (a) sound concrete;(b) honeycomb.

B.3 Concrete model with surface deterioration

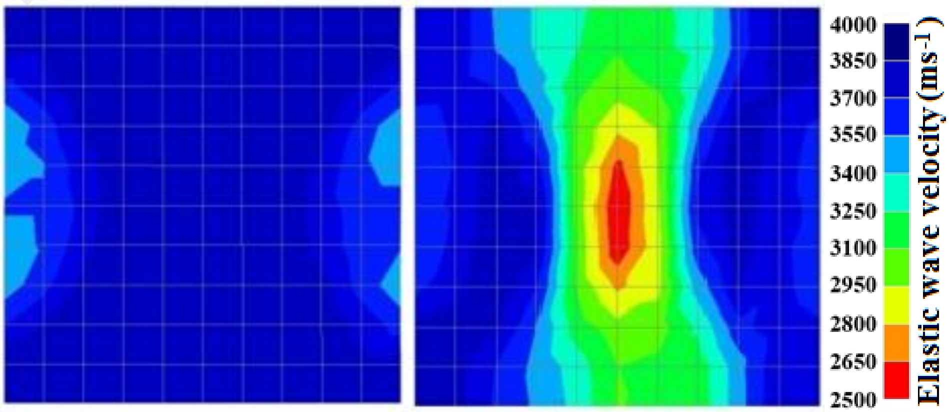

(a) (b)

Figure B6: Tomogram of case 3.7 by numerical simiulation 2 sided travel time technique:(a) surface deterioration ($V=2500ms^{-1}$) with sound concrete;(b) surface deterioration ($V=2500ms^{-1}$) with honeycomb ($V=1500ms^{-1}$).

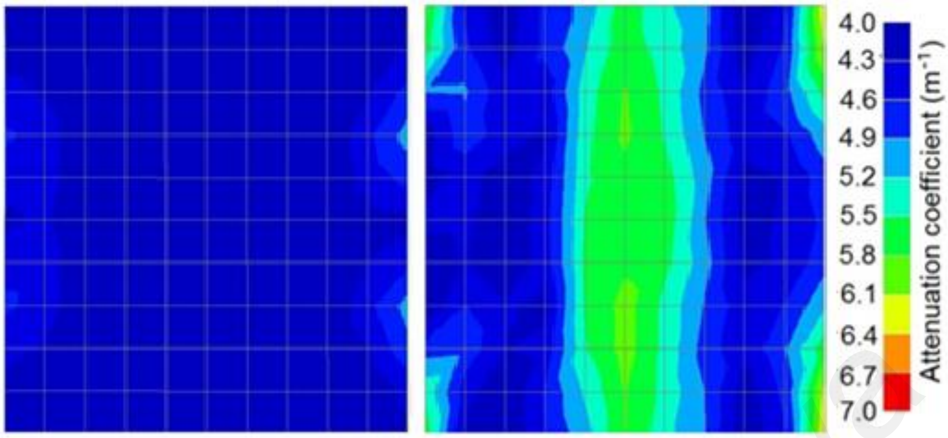

(a) (b)

Figure B7: Tomogram of case 3.7 by numerical simiulation 2 sided amplitude technique:(a) surface deterioration ($V=2500ms^{-1}$) with sound concrete;(b) surface deterioration ($V=2500ms^{-1}$) with honeycomb ($V=1500ms^{-1}$).

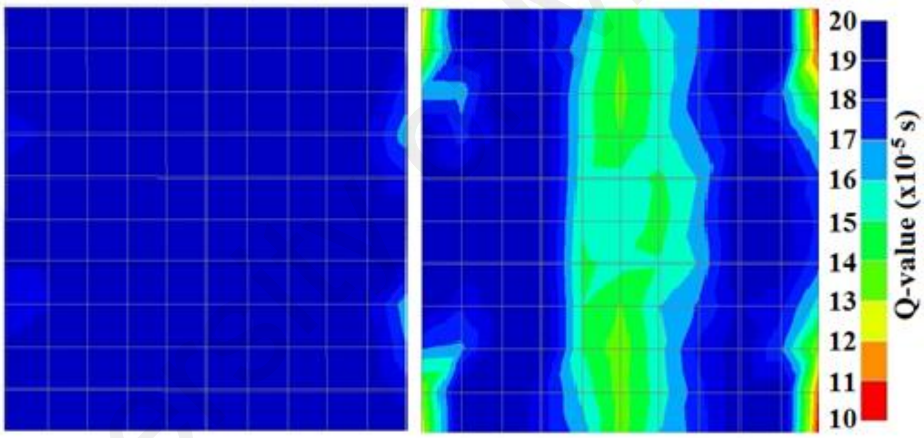

(a) (b)

Figure B8: Tomogram of case 3.7 by numerical simiulation 2 sided Q-value technique:(a) surface deterioration ($V=2500ms^{-1}$) with sound concrete;(b) surface deterioration($V=2500ms^{-1}$) with honeycomb($V=1500ms^{-1}$).

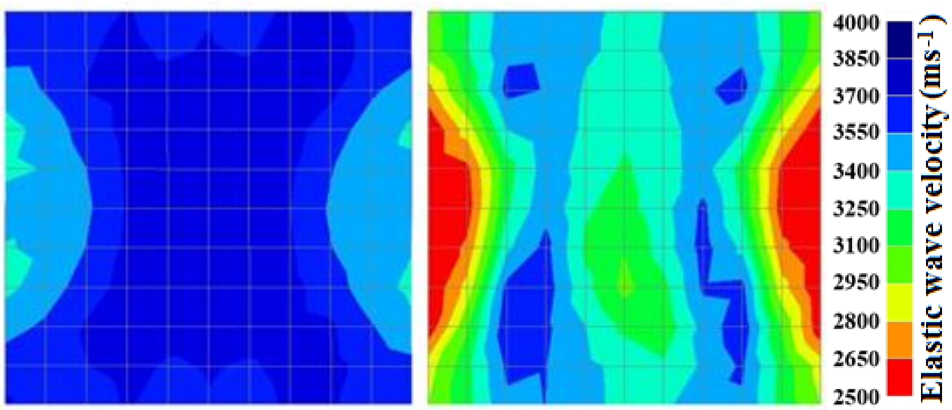

(a) (b)

Figure B9: Tomogram of case Figure 3.8 by 2 sided travel time technique:(a) surface deterioration with sound concrete($V=1500\ ms^{-1}$) ;(b) surface deterioration with honeycomb($V=2500\ ms^{-1}$).

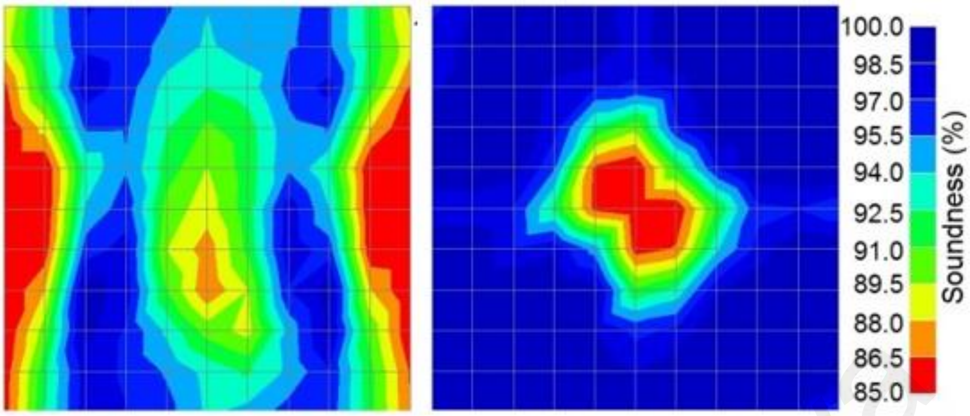

(a) (b)

Figure B10: Soundness of Tomogram case Figure 3.8 with honeycomb ($V=2500ms^{-1}$) and surface deteriorated ($V=1500ms^{-1}$) by: (a) 2 side travel time technique ;(b) 4-sided travel time technique.

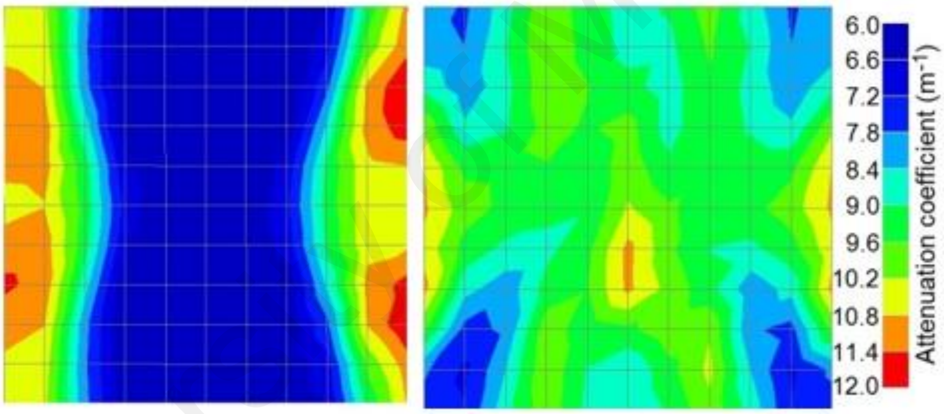

(a) (b)

Figure B11: Tomogram of case Figure 3.8 by 2 sided amplitude technique :(a) surface deterioration with sound concrete($V=1500\ ms^{-1}$) ;(b) surface deterioration with honeycomb($V=2500\ ms^{-1}$).

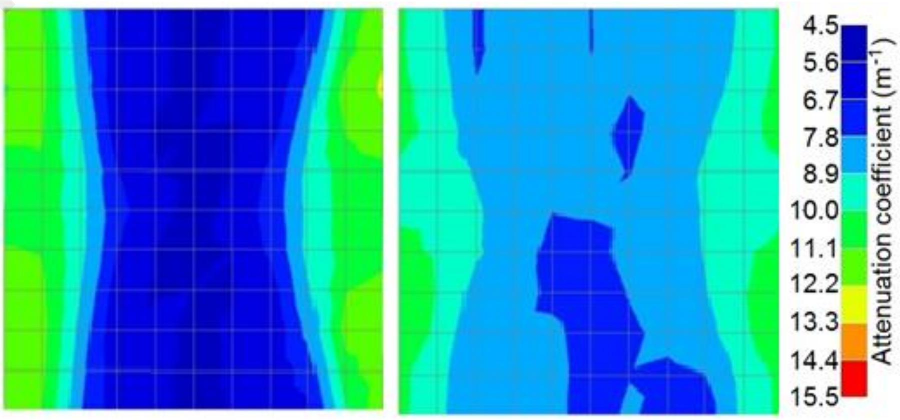

(a) (b)

Figure B12 : Tomogram of case Figure 3.8 by 2 sided frequency technique:(a) surface deterioration with sound concrete(V=1500 ms^{-1}) ;(b) surface deterioration with honeycomb(V=2500 ms^{-1}).

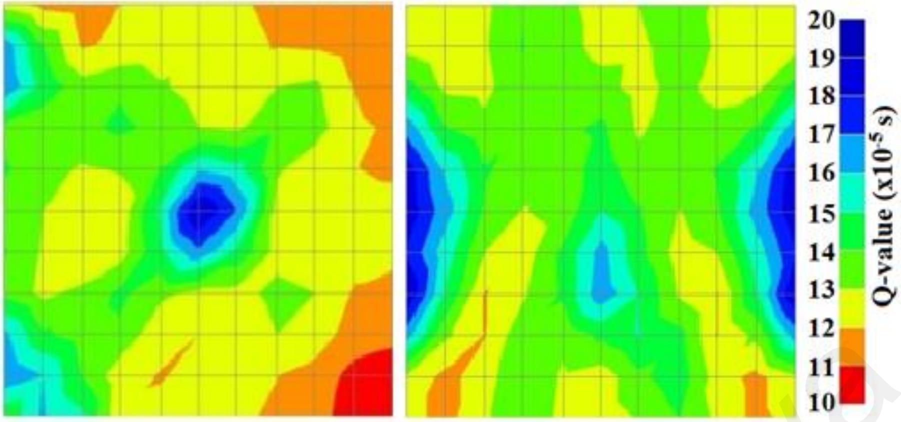

(a) (b)

Figure B13 : Tomogram of case Figure 3.8 by 2 sided Q-value technique:(a) surface deterioration with sound concrete(V=1500 ms^{-1}) ;(b) surface deterioration with honeycomb(V=2500 ms^{-1}).

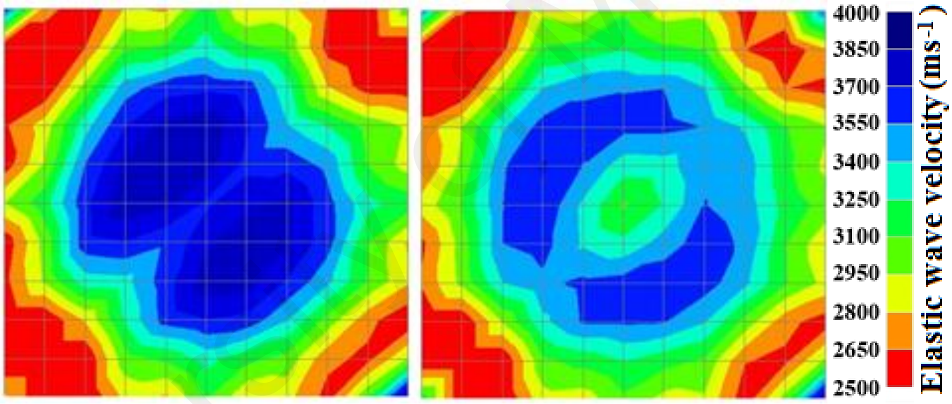

(a) (b)

Figure B14: Tomogram of case Figure 3.8 by 4 sided travel time technique:(a) surface deterioration with sound concrete(V=1500 ms^{-1}) ;(b) surface deterioration with honeycomb(V=2500 ms^{-1}).

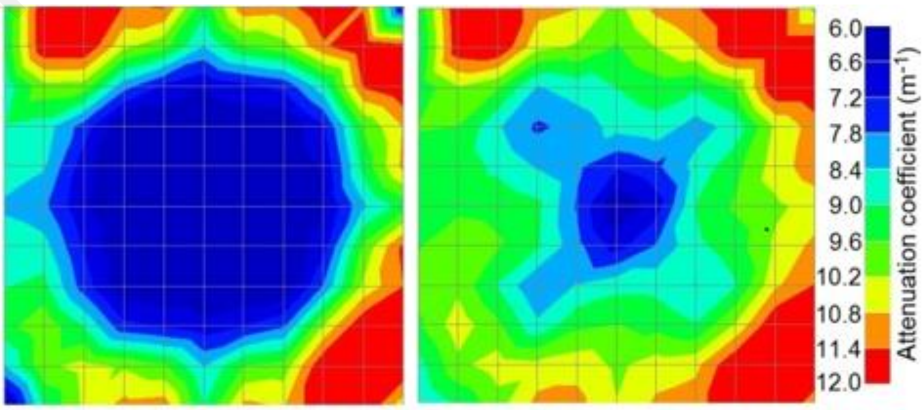

(a) (b)

Figure B15: Tomogram of case Figure 3.8 by 4 sided amplitude technique:(a) surface deterioration with sound concrete(V=1500 ms^{-1}) ;(b) surface deterioration with honeycomb(V=2500 ms^{-1}).

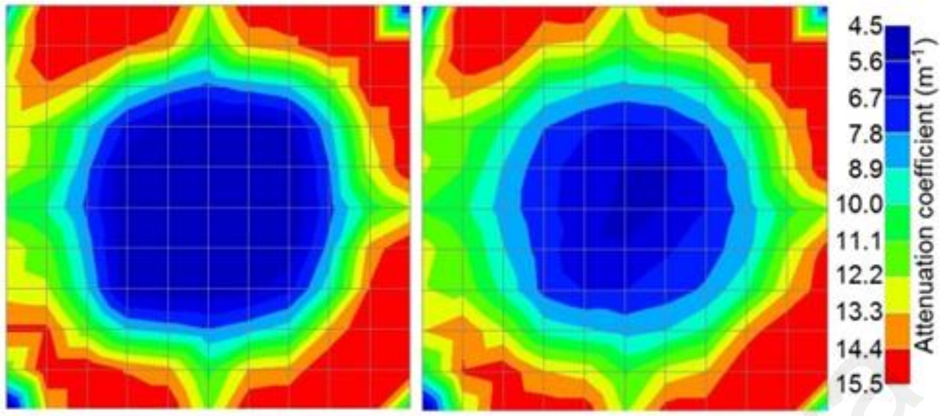

(a) (b)

Figure B16: Tomogram of case Figure 3.8 by 4 sided frequency technique :(a) surface deterioration with sound concrete(V=1500 ms^{-1}) ;(b) surface deterioration with honeycomb(V=2500 ms^{-1}).

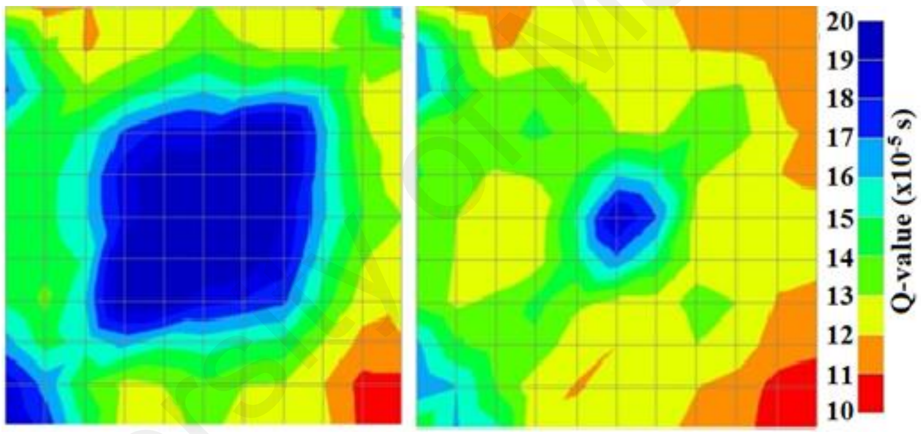

(a) (b)

Figure B17: Tomogram of case Figure 3.8 by 4 sided Q-value technique :(a) surface deterioration with sound concrete(V=1500 ms^{-1}) ;(b) surface deterioration with honeycomb(V=2500 ms^{-1}).

B.4 Aluminium sheath PC model

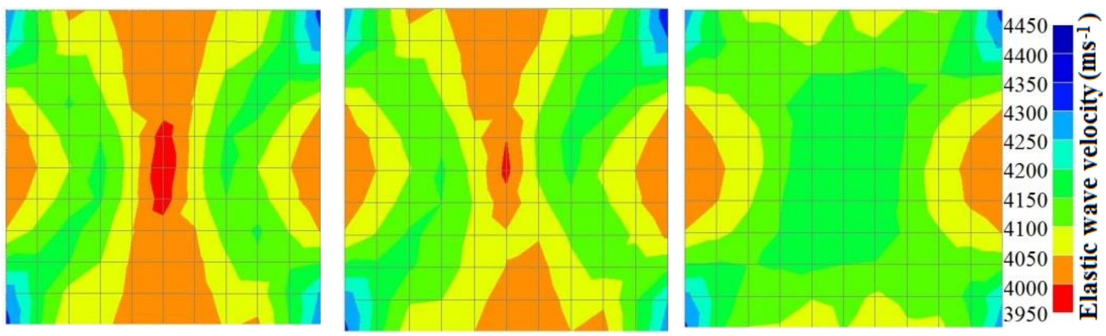

(a) (b) (c)

Figure B18: Tomogram of case Figure 3.9 ,PC with aluminium tendon sheath tested by 2 sided travel time technique:(a) 0 % grout filling; (b) 50 % filling; (c) 100% filling.

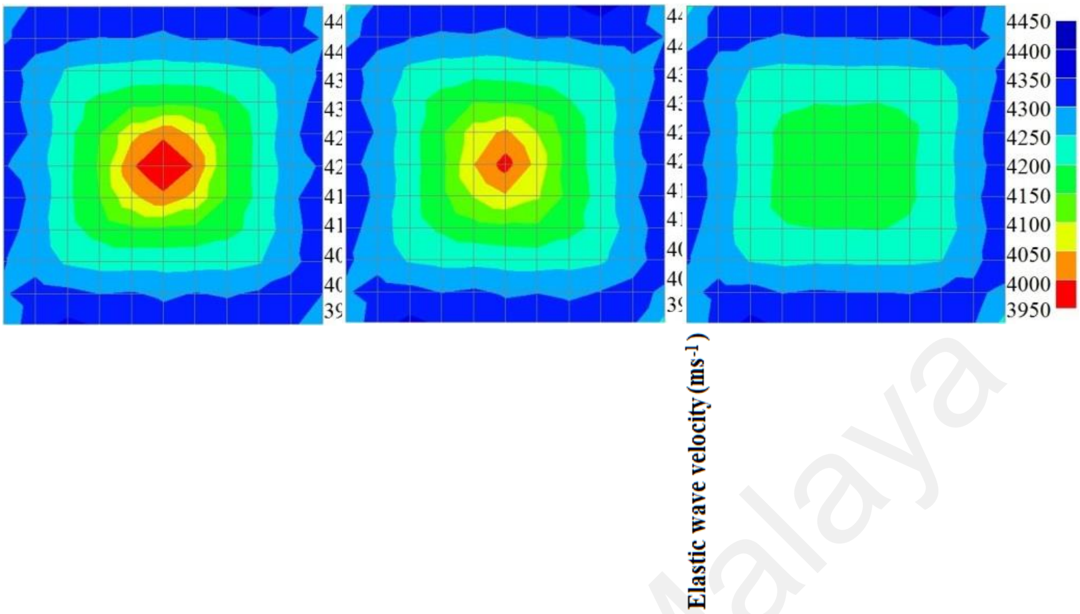

(a) (b) (c)

Figure B19: Tomogram of case Figure 3.9 ,PC with aluminium tendon sheath tested by 4 sided travel time technique:(a) 0 % grout filling; (b) 50 % filling; (c) 100% filling.

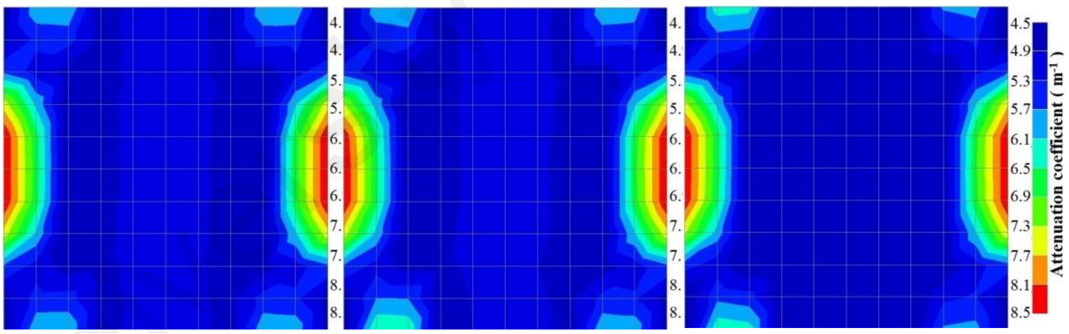

(a) (b) (c)

Figure B20: Tomogram of case Figure 3.9 ,PC with aluminium tendon sheath tested by 2 sided amplitude technique:(a) 0 % grout filling; (b) 50 % filling; (c) 100% filling.

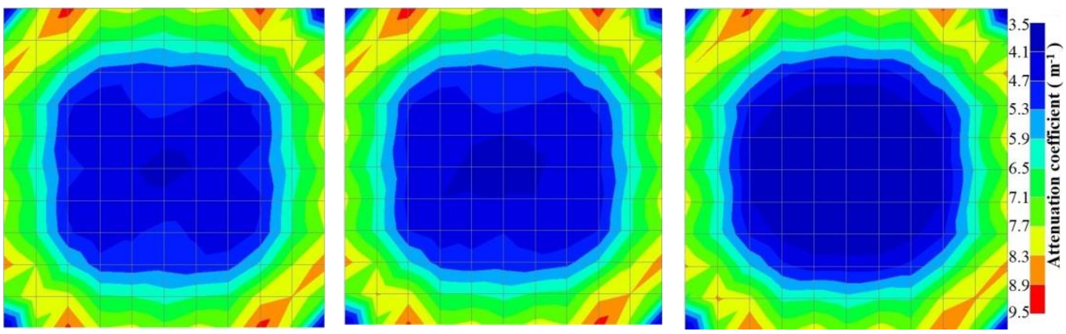

(a) (b) (c)

Figure B21: Tomogram of case Figure 3.9 , PC with aluminium tendon sheath tested by 4 sided amplitude technique:(a) 0 % grout filling; (b) 50 % filling; (c) 100% filling.

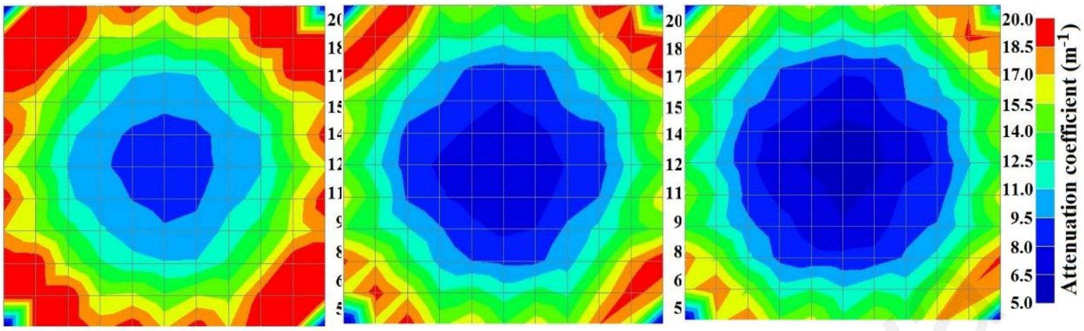

(a) (b) (c)

Figure B22: Tomogram of case Figure 3.9 , PC with aluminium tendon sheath tested by 4 sided frequency technique:(a) 0 % grout filling; (b) 50 % filling; (c) 100% filling.

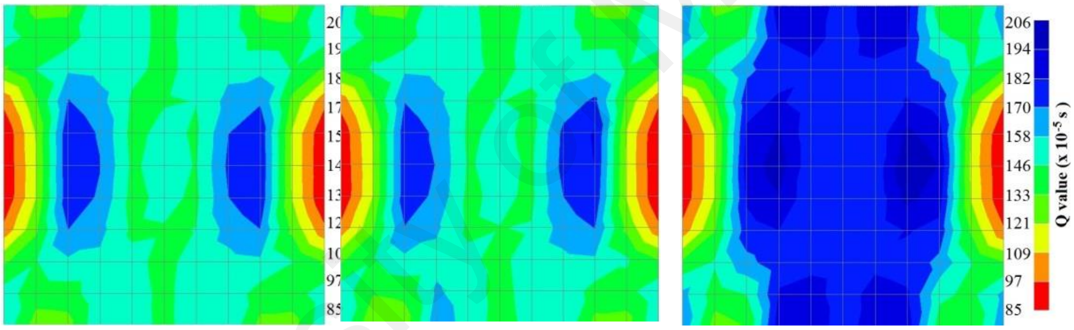

(a) (b) (c)

Figure B23: Tomogram of case Figure 3.9 , PC with aluminium tendon sheath tested by 2 sided Q-value technique:(a) 0 % grout filling; (b) 50 % filling; (c) 100% filling.

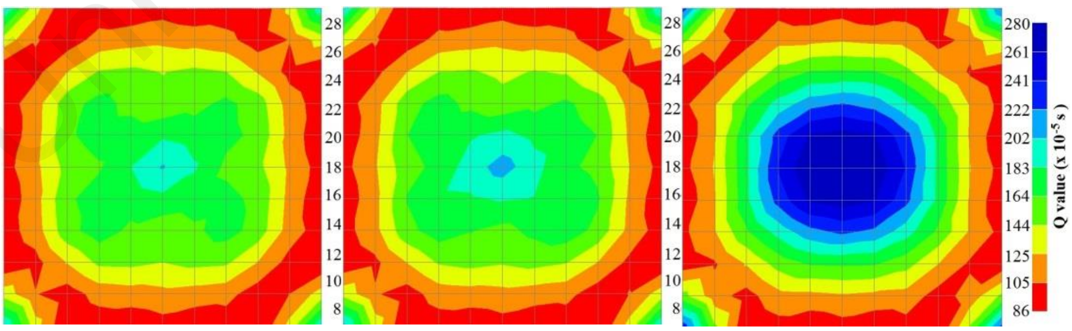

(a) (b) (c)

Figure B24: Tomogram of case Figure 3.9 , PC with aluminium tendon sheath tested by 4 sided Q-value technique:(a) 0 % grout filling; (b) 50 % filling; (c) 100% filling.

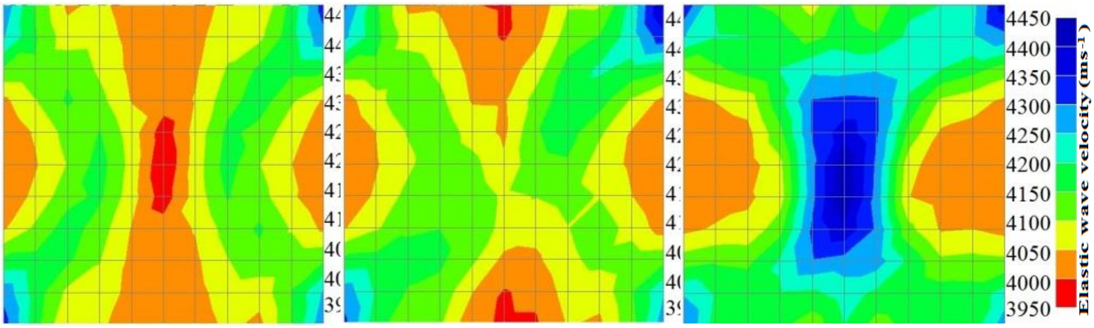

(a) (b) (c)

Figure B25: Tomogram of case Figure 3.10, PC with aluminium tendon sheath with steel tendon measuring by 2 sided travel time technique:(a) 0 % grout filling; (b) 50 % filling; (c) 100% filling.

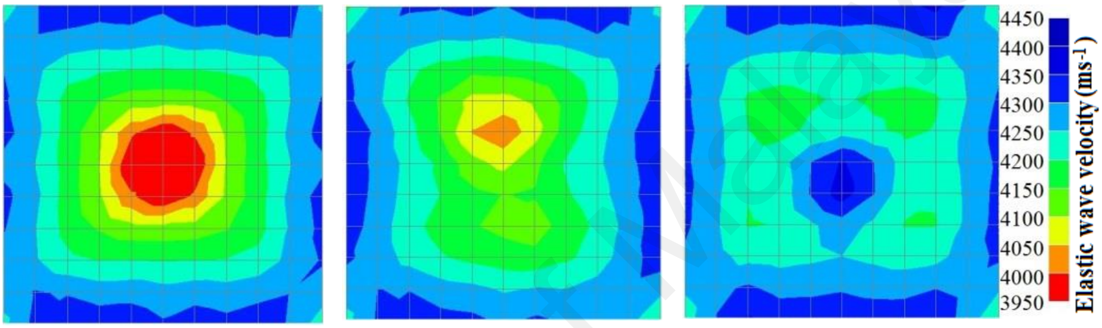

(a) (b) (c)

Figure B26: Tomogram of case Figure 3.10, PC with aluminium tendon sheath with steel tendon measuring by 4 sided travel time technique:(a) 0 % grout filling; (b) 50 % filling; (c) 100% filling.

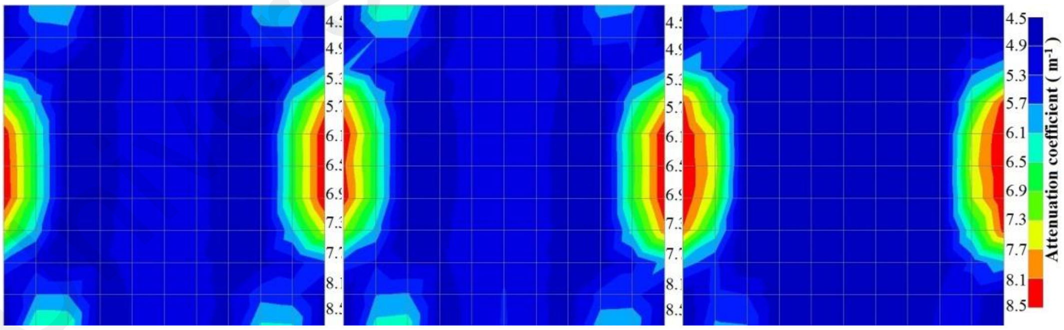

(a) (b) (c)

Figure B27: Tomogram of case Figure 3.10, PC with aluminium tendon sheath with steel tendon plotted by 2 sided amplitude technique:(a) 0 % grout filling; (b) 50 % filling; (c) 100% filling.

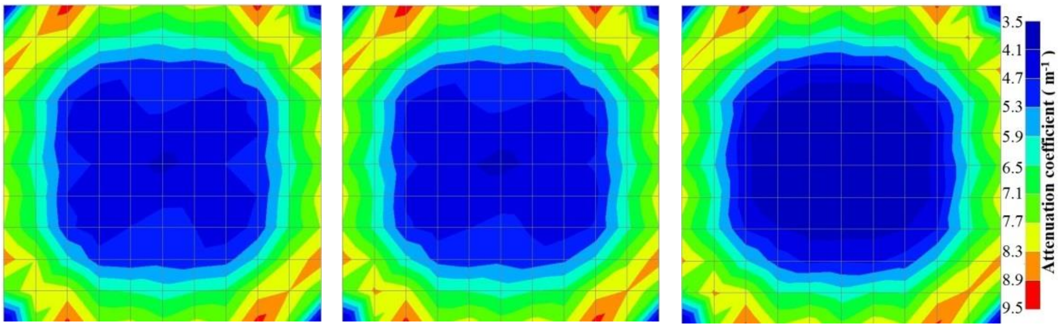

(a) (b) (c)

Figure B28: Tomogram of case Figure 3.10, PC with aluminium tendon sheath with steel tendon plotted by 4 sided amplitude technique:(a) 0 % grout filling; (b) 50 % filling; (c) 100% filling.

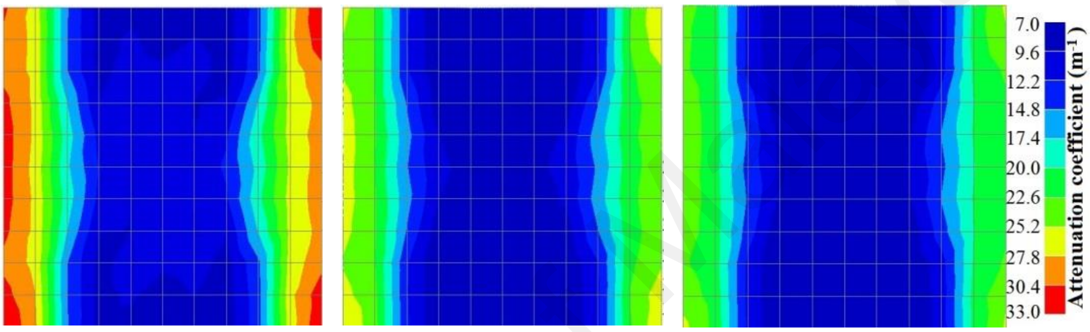

(a) (b) (c)

Figure B29: Tomogram of case Figure 3.10, PC with aluminium tendon sheath with steel tendon tested by 2 sided frequency technique:(a) 0 % grout filling; (b) 50 % filling; (c) 100% filling.

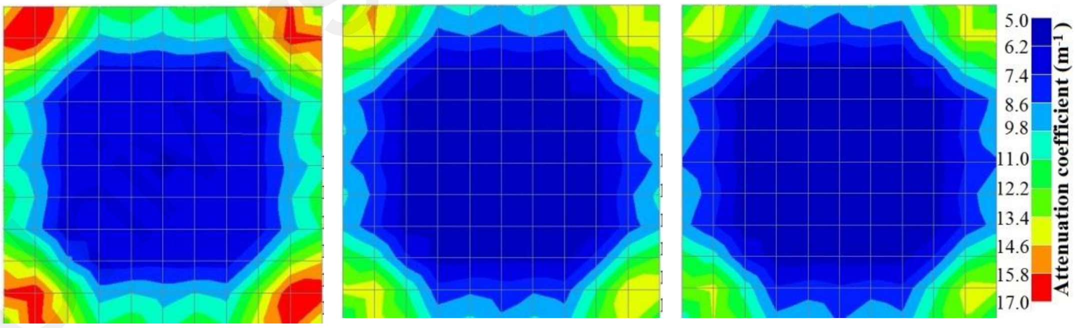

(a) (b) (c)

Figure B30: Tomogram of case Figure 3.10, PC with aluminium tendon sheath with steel tendon measuring by 4 sided frequency technique:(a) 0 % grout filling; (b) 50 % filling; (c) 100% filling.

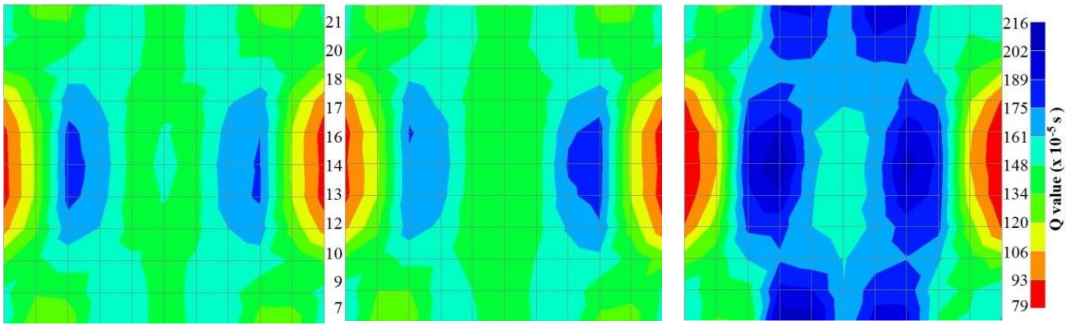

(a) (b) (c)

Figure B31: Tomogram of case Figure 3.10, PC with aluminium tendon sheath with steel tendon measuring by 2 sided Q-value technique:(a) 0 % grout filling; (b) 50 % filling; (c) 100% filling.

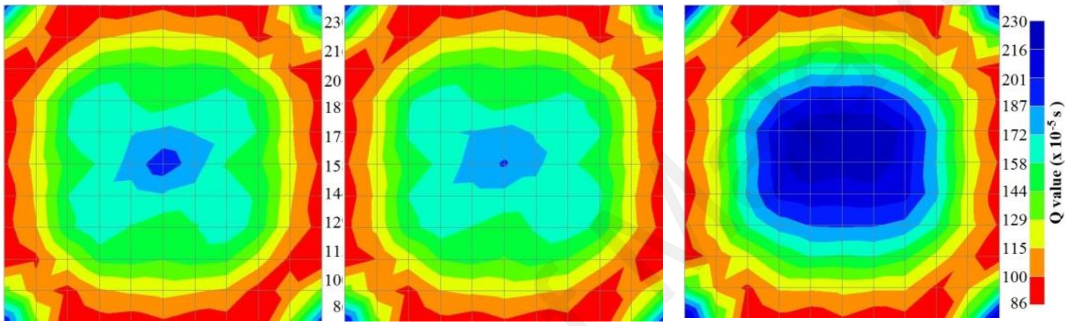

(a) (b) (c)

Figure B32: Tomogram of case Figure 3.10, PC with aluminium tendon sheath with steel tendon measuring by 4 sided Q-value technique:(a) 0 % grout filling; (b) 50 % filling; (c) 100% filling.

B.5 Polyethylene sheath PC model

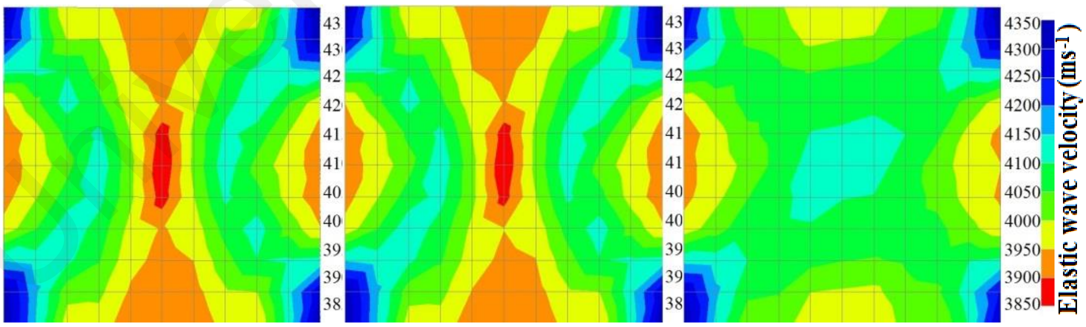

(a) (b) (c)

Figure B33: Tomogram of case Figure 3.9, PC with polyethylene tendon sheath measuring by 2 sided travel time technique:(a) 0 % grout filling; (b) 50 % filling; (c) 100% filling.

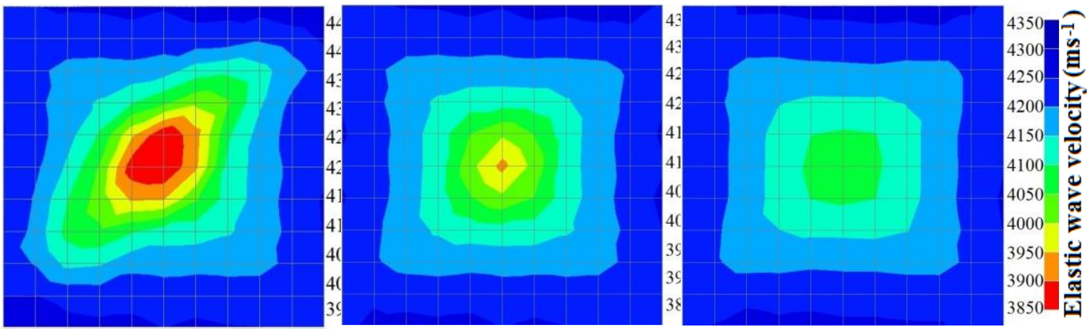

(a) (b) (c)

Figure B34: Tomogram of case Figure 3.9, PC with polyethylene tendon sheath plotted by 4 sided travel time technique:(a) 0 % grout filling; (b) 50 % filling; (c) 100% filling.

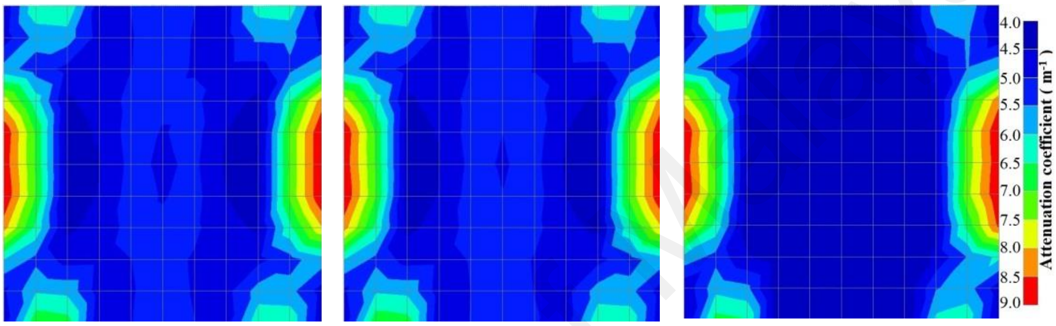

(a) (b) (c)

Figure B35: Tomogram of case Figure 3.9, PC with polyethylene tendon sheath plotted by 2 sided amplitude technique:(a) 0 % grout filling; (b) 50 % filling; (c) 100% filling.

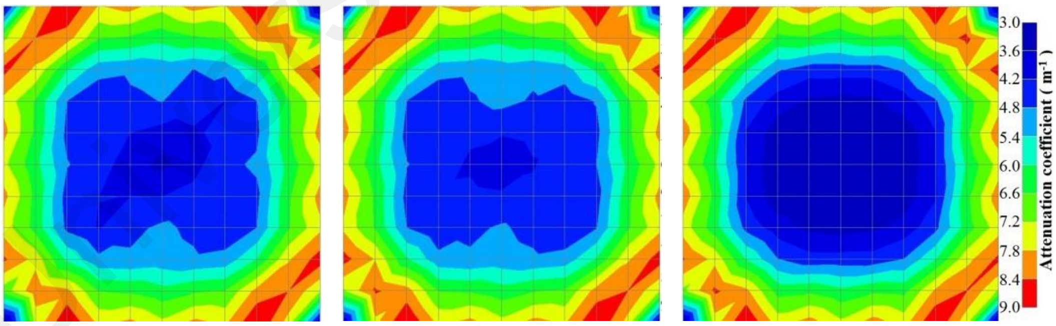

(a) (b) (c)

Figure B36: Tomogram of case Figure 3.9, PC with polyethylene tendon sheath plotted by 4 sided amplitude technique:(a) 0 % grout filling; (b) 50 % filling; (c) 100% filling.

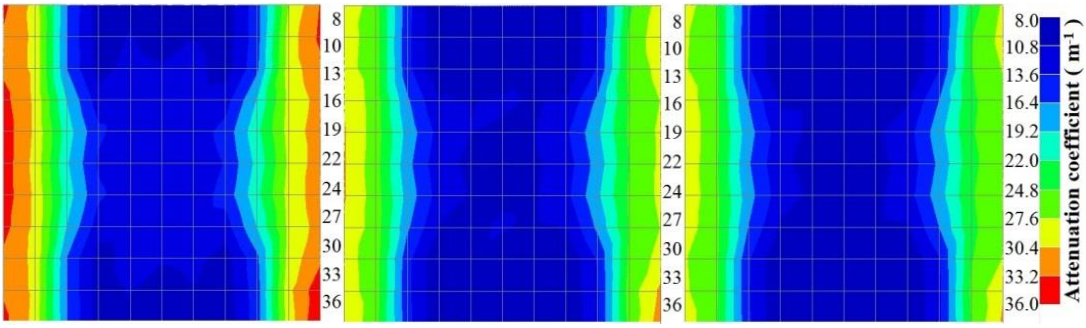

(a) (b) (c)

Figure B37: Tomogram of case Figure 3.9, PC with polyethylene tendon sheath plotted by 2 sided frequency technique:(a) 0 % grout filling; (b) 50 % filling; (c) 100% filling.

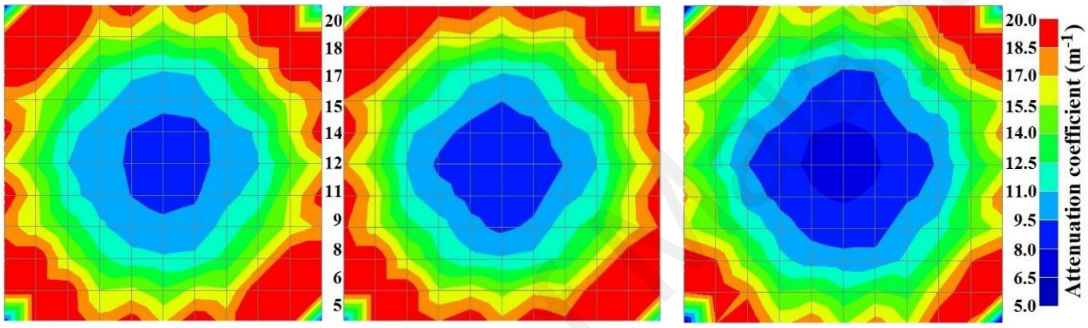

(a) (b) (c)

Figure B38: Tomogram of case Figure 3.9, PC with polyethylene tendon sheath plotted by 4 sided frequency technique:(a) 0 % grout filling; (b) 50 % filling; (c) 100% filling.

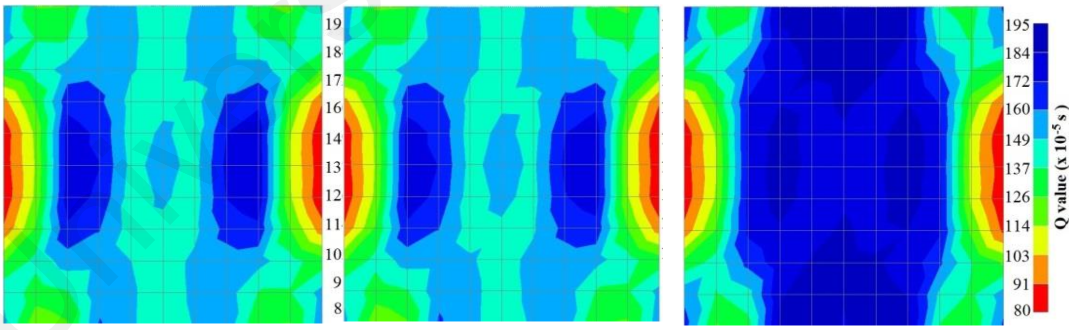

(a) (b) (c)

Figure B39: Tomogram of case Figure 3.9, PC with polyethylene tendon sheath plotted by 2 sided Q-value technique:(a) 0 % grout filling; (b) 50 % filling; (c) 100% filling.

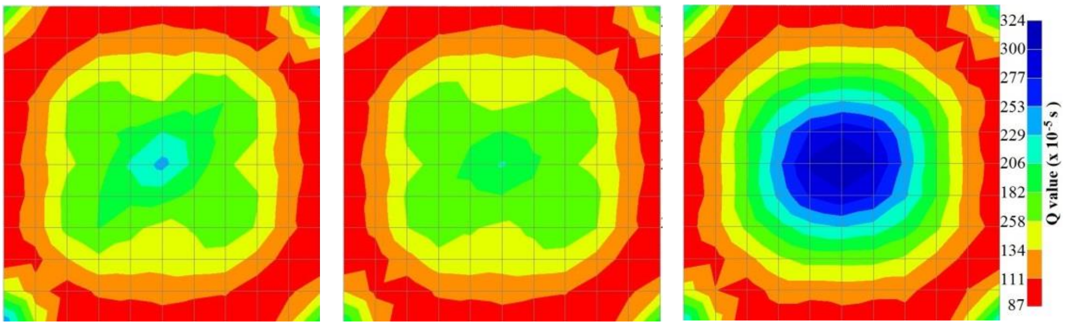

(a) (b) (c)

Figure B40: Tomogram of case Figure 3.9, PC with polyethylene tendon sheath plotted by 4 sided Q-value technique:(a) 0 % grout filling; (b) 50 % filling; (c) 100% filling.

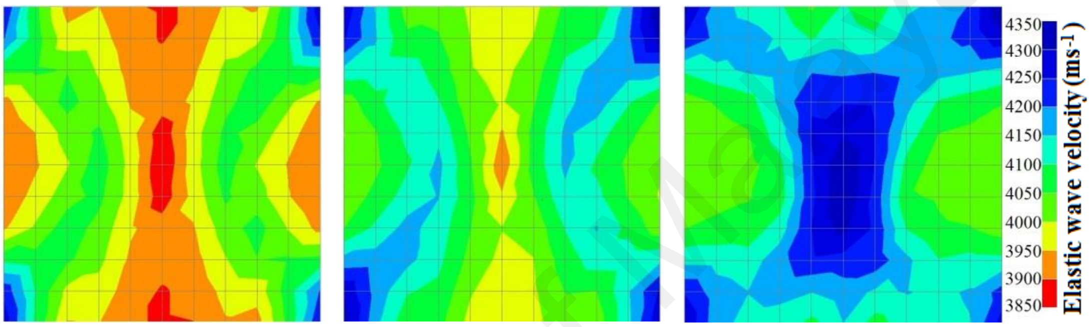

(a) (b) (c)

Figure B41: Tomogram of case Figure 3.10, PC with polyethylene tendon sheath with steel tendon plotted by 2 sided travel time technique:(a) 0 % grout filling; (b) 50 % filling; (c) 100% filling.

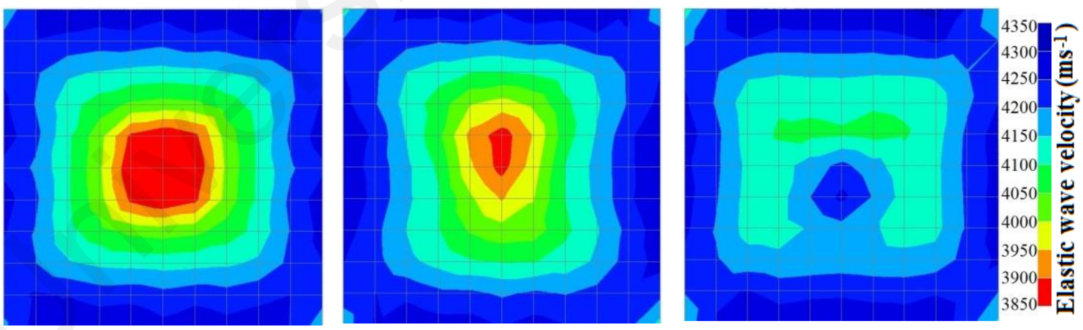

(a) (b) (c)

Figure B42: Tomogram of case Figure 3.10, PC with polyethylene tendon sheath with steel tendon plotted by 4 sided travel time technique:(a) 0 % grout filling; (b) 50 % filling; (c) 100% filling.

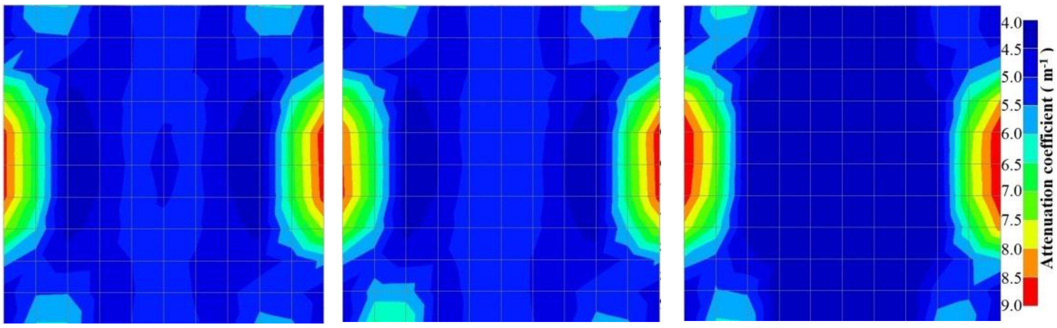

(a) (b) (c)

Figure B43: Tomogram of case Figure 3.10, PC with polyethylene tendon sheath with steel tendon plotted by 2 sided amplitude technique:(a) 0 % grout filling; (b) 50 % filling; (c) 100% filling.

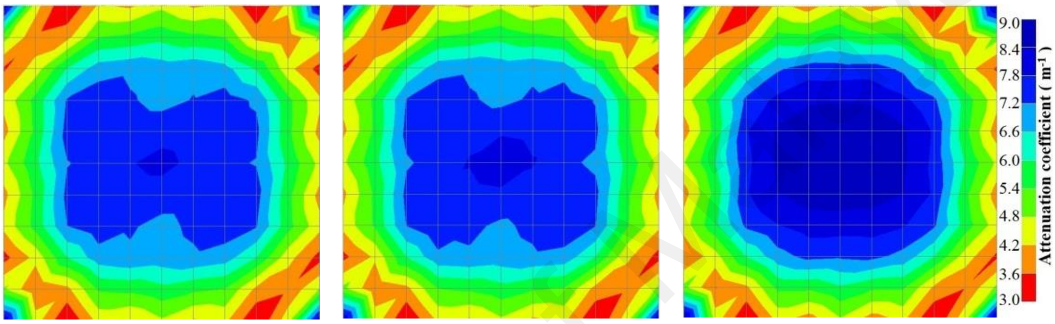

(a) (b) (c)

Figure B44: Tomogram of case Figure 3.10, PC with polyethylene tendon sheath with steel tendon plotted by 4 sided amplitude technique:(a) 0 % grout filling; (b) 50 % filling; (c) 100% filling.

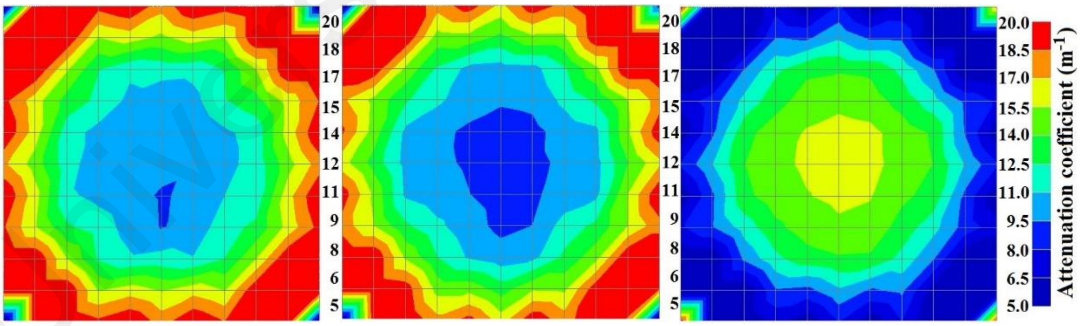

(a) (b) (c)

Figure B45: Tomogram of case Figure 3.10, PC with polyethylene tendon sheath with steel tendon plotted by 4 sided Q-value technique:(a) 0 % grout filling; (b) 50 % filling; (c) 100% filling.

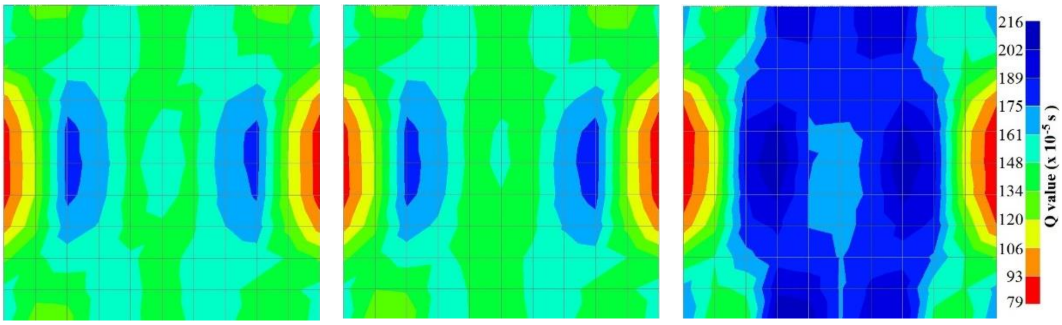

(a) (b) (c)

Figure B46: Tomogram of case Figure 3.9, PC with polyethylene tendon sheath plotted by 2 sided Q-value technique:(a) 0 % grout filling; (b) 50 % filling; (c) 100% filling.

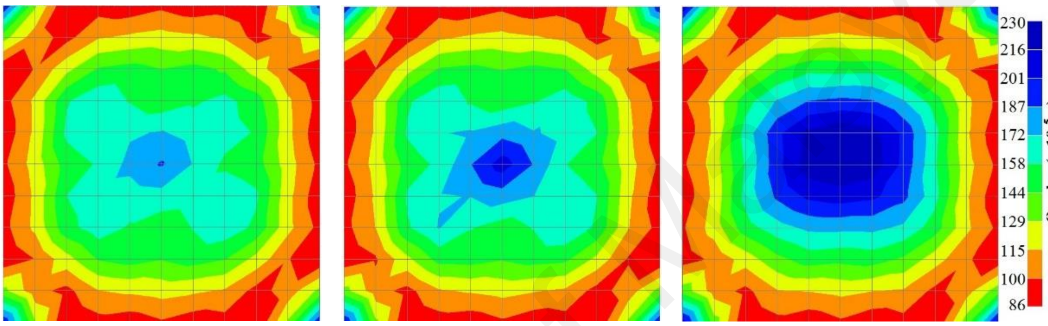

(a) (b) (c)

Figure B47: Tomogram of case Figure 3.9, PC with polyethylene tendon sheath plotted by 4 sided Q-value technique:(a) 0 % grout filling; (b) 50 % filling; (c) 100% filling.

B.6 Aluminium sheath PC Specimen

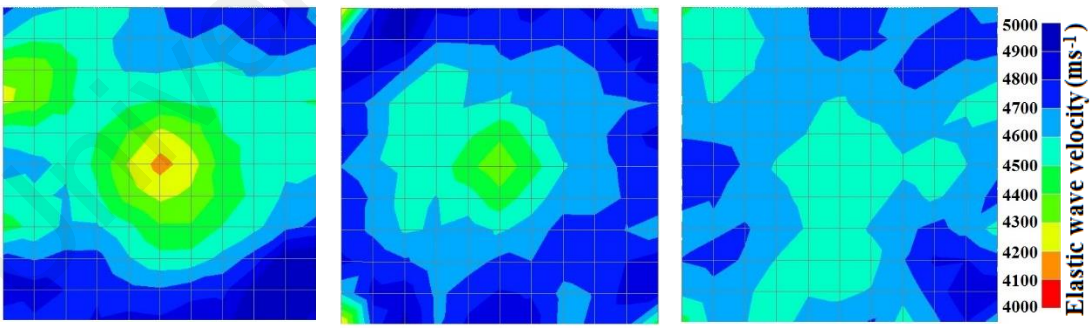

(a) (b) (c)

Figure B48: Tomogram of case Figure 3.14, PC with polyethylene tendon sheath plotted by 25 khz frequency laboratory 4 sided travel time technique:(a) 0 % grout filling; (b) 50 % filling; (c) 100% filling.

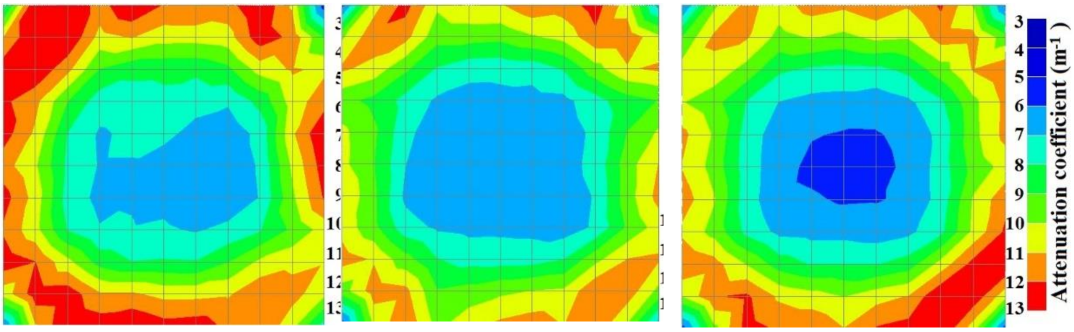

(a) (b) (c)

Figure B49: Tomogram of case Figure 3.14, PC with polyethylene tendon sheath plotted by 25 khz frequency laboratory 4 sided amplitude technique:(a) 0 % grout filling; (b) 50 % filling; (c) 100% filling.

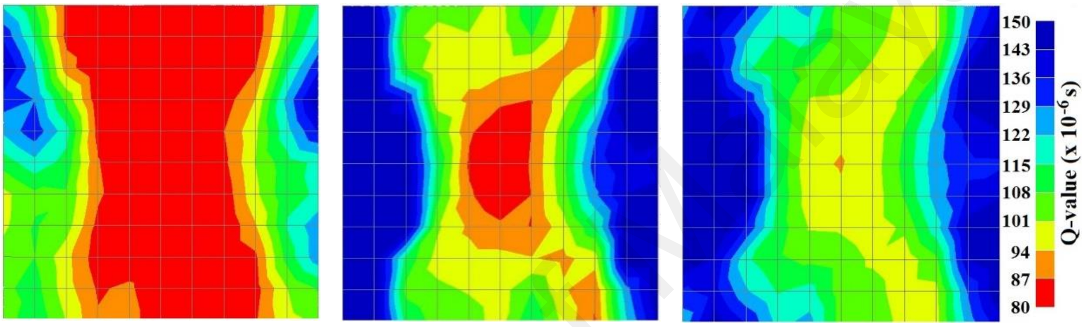

(a) (b) (c)

Figure B50: Tomogram of case Figure 3,14, PC with polyethylene tendon sheath plotted by 25 khz frequency laboratory 2 sided Q-value technique:(a) 0 % grout filling; (b) 50 % filling; (c) 100% filling.

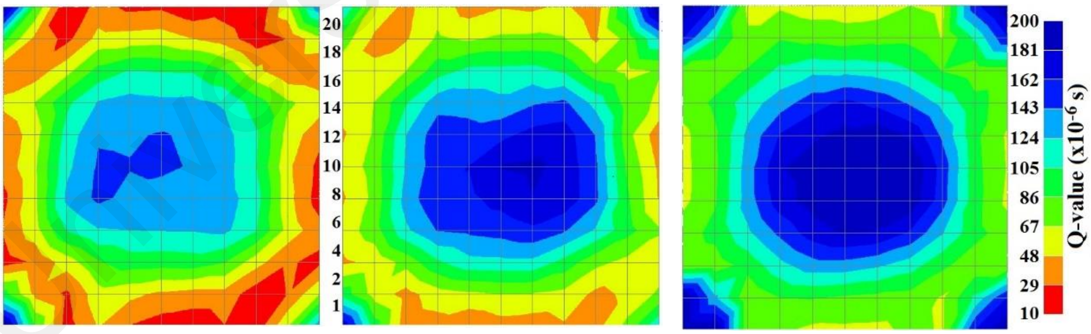

(a) (b) (c)

Figure B51: Tomogram of case Figure 3.14, PC with polyethylene tendon sheath plotted by 25 khz frequency laboratory 4 sided Q-value technique:(a) 0 % grout filling; (b) 50 % filling; (c) 100% filling.

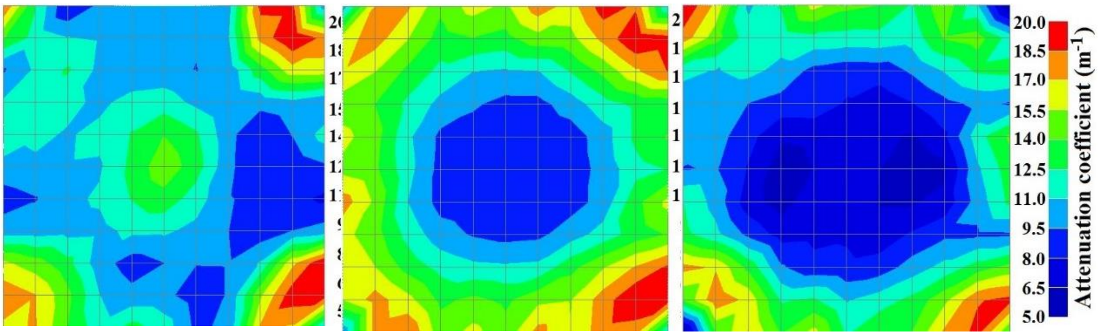

(a) (b) (c)

Figure B52: Tomogram of case Figure 3.14, PC with polyethylene tendon sheath plotted by 18 khz frequency laboratory 4 sided frequency technique:(a) 0 % grout filling; (b) 50 % filling; (c) 100% filling.

LIST OF PUBLICATION

Chai, H. K., Liu, K. F., Behnia, A., Yoshikazu, K. & Shiotani, T. (2016). Development of a Tomography Technique for Assessment of the Material Condition of Concrete Using Optimized Elastic Wave Parameters. *Materials,* 2016, *9*, 291. (*ISI/SCOPUS Cited Publication*)

Liu, K. F., Chai, H. K., Mehrabi, N., Kobayashi, Y. & Shiotani, T. (2014). Condition Assessment of PC Tendon Duct Filling by Elastic Wave Velocity Mapping. *The Scientific World Journal*. Article ID 194295. (*ISI/SCOPUS Cited Publication*)

Liu, K. F., Chai, H. K., Kobayashi, Y. & Shiotani, T. (2014). Development of Tomography Reconstruction Technique for Concrete Using Elastic Wave Time and Frequency Domain Parameters. Proceedings from *6th Asia and Pacific Young Researchers and Graduates Symposium*. SIIT, Thailand.